Waveguide-based single molecule detection in flow

Dissertation zur Erlangung des
naturwissenschaftlichen Doktorgrades
der Julius-Maximilians-Universität Würzburg

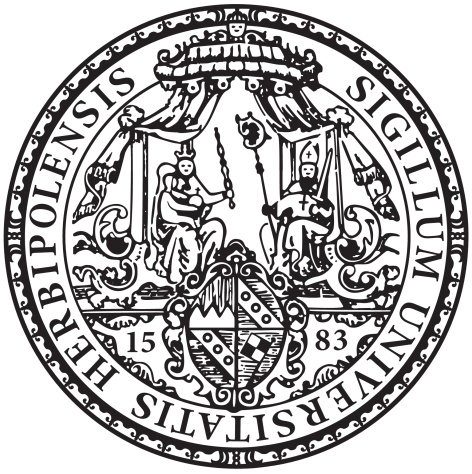

vorgelegt von
Patrick Then

aus
Schweinfurt

Würzburg 2015

Eingereicht am: 16.09.2015
bei der Fakultät für Physik und Astronomie

1. Gutachter: Bert Hecht
2. Gutachter: Markus Sauer
3. Gutachter: .....
der Dissertation.

Vorsitzende(r): Karl Brunner

1. Prüfer: Bert Hecht
2. Prüfer: Markus Sauer
3. Prüfer: Björn Trauzettel
im Promotionskolloquium

Tag des Promotionskolloquiums: 05.08.2016

Doktorurkunde ausgehändigt am: .....

Gewidmet meinem Großvater

List of Publications

Fast quantitative single-molecule detection at ultralow concentrations
Haas, P.*; Then, P.*; Wild, A.*; Grange, W.; Zorman, S.; Hegner, M.; Calame, M.; Aebi, U.; Flammer, J.; Hecht, B.
Analytical Chemistry, **82**(14):6299-6302, July 2010.
* *authors contributed equally*

Remote detection of single emitters via optical waveguides
Then, P.; Razinskas, G.; Feichtner, T.; Haas, P.; Wild, A.; Bellini, N.; Osellame, R.; Cerullo, G.; Hecht, B.
Physical Review A, **89**(5), May 2014.

Publication	**Details**	**Thesis**
"Fast quantitative..."[1]		
Supporting Information	text reproduced, modified, extended	section 2.3.2
pp. 6299-6301, SI	text & figures reproduced, modified, ext.	section 5.4
"Remote detection..."[2]		
appendix C	text reproduced, modified, extended	section 2.2.4
pp. 1-2, appendix A	text reproduced, modified	section 2.2.5
p. 1	text reproduced, modified, extended	section 5.1
pp. 2-3	text & figures reproduced, modified, ext.	section 5.2
pp. 3-5, appendix B	text & figures reproduced, modified, ext.	section 5.3
p. 5	text & figures reproduced, modified, ext.	section 5.5

Abstract

In this work fluorescence-based single molecule detection at low concetration is investigated, with an emphasis on the usage of active transport and waveguides. Active transport allows to overcome the limits of diffusion-based systems in terms of the lowest detectable threshold of concentration. The effect of flow in single molecule experiments is investigated and a theoretical model is derived for laminar flow. Waveguides on the other hand promise compact detection schemes and show great potential for their possible integration into lab-on-a-chip applications. Their properties in single molecule experiments are analyzed with help of a method based on the reciprocity theorem of electromagnetic theory.

Contents

1. Introduction

Over the past 25 years, the development of novel fluorescent probes and sensitive, yet affordable instruments have prompted a rapid development of optical single molecule techniques [3, 4, 5]. Offering both the possibility to probe behaviour otherwise hidden in time-averaged ensemble measurements and an unprecedented sensitivity, single molecule fluorescence quickly grew to one of the most influential single molecule methods in the field of biophysics.

While the first realizations of single molecule detection (SMD) had to be performed at cryogenic temperatures and with molecules embedded in crystal matrices [6, 7], experiments soon progressed to the detection of single fluorescent molecules in solution [8]. Today, single molecule fluorescence techniques are used in many diverse applications, notably boosted by the development of various fluorescent markers for biomolecules. Through Förster Resonance Energy Transfer (FRET) [9] it has become possible to probe relative dipole orientation and distance between two fluorescent molecules, a property that is widely employed to determine binding properties and conformation of complex molecules such as proteins or nucleic acid sequences [10]. In DNA sequencing, single molecule fluorescence is contributing to reduction of cost and time in a field of growing importance to genetic research and modern medicine [11]. Another important field is super-resolution imaging, the recording of microscopic images with resolution well beyond the diffraction limit. Initially conceived through Near-Field Scanning Optical Microscopy (NSOM) [12, 13], recent years have brought the development of far-field techniques such as Stimulated Emission Depletion (STED) [14], which locally depletes excited-state fluorophores or methods such as Photoactivated-Localization Microscopy (PALM) [15] and Stochastic Optical Reconstruction Microscopy (STORM) [16], which are based on the stochastic readout of molecules combined with precision-localization. Lastly, single molecule fluorescence forms the basis for highly sensitive detection schemes aimed at the detection of biomolecules such as DNA or proteins. Using fluorescent markers such as "molecular beacons" [17], SMD can be used to monitor gene expression, specific antigenes or early-onset disease markers. In recent years the integration of single-emitter detection within lab-on-a-chip (LOC) architectures has attracted significant interest, due to the obvious allure from a combination of the ultimate sensitivity of single-emitter detection with the handling of ultra-small analyte volumes through microfluidics and parallel processing in a compact package [18, 19, 20].

The applicability of the typically diffraction-limited optical single molecule methods, which are relying on transport of analyte molecules by diffusion is limited within a relatively narrow range of analyte molecule concentration. Typically that range is between a few hundred fM (femtomolar or femtomoles per liter) and a few nM [21].

The upper limit is a consequence of the necessity to measure an individual single molecule, which requires both a small observation volume and a low enough concentration of analyte molecules. Higher concentrations are encountered in many biological interactions (e.g. protein-DNA interactions), which often occur in the micromolar or even millimolar range. Experiments in high-concentration environments thus require a reduction of the effective observation volume below the diffraction limit. This has been realized e.g. through methods such as STED, or by use of novel near-field optical probes such as "optical nanoantennas" which at the same time facilitate a strong local excitation of emitters and a boosted emission of photons via the enhancement of the local optical density of states [22, 23]. On the other end of the concentration range, ultra-low concentrations pose different problems. As many disease-biomarkers, e.g. for cancer, or viral loads exist in bodily fluids at very low concentration, measurement time becomes increasingly an issue. Considering free diffusion only, the time between two successive single molecule detection events increases inversely proportional to the concentration. For a concentration of a few femtomolar and lower, typical confocal detection schemes with a detection volume of ~ 1 fL quickly encounter average downtimes between single molecule detection events of several tens of minutes to hours when relying purely on diffusive transport of analyte molecules. To extend single molecule fluorescence techniques into regions of lower concentration one can either artificially increase concentration through preconcentration steps [24, 25] or provide some form of active transport, e.g. through mixing of the sample or by providing controlled flow as in microfluidic devices. Microfluidics is of interest also due to its importance in LOC devices, where it forms the basis for transport and manipulation of the sample fluid.

In this work the detection of single emitters at low concentration with the purpose of implementation into compact and easy-to-use sensors is investigated. The problem is therefore approached from two sides: by overcoming the diffusion-limit through active transport of molecules provided by flow and by studying both the suitability and optimization of alternate, waveguide-based detection schemes specifically with the purpose of integrating them into compact and efficient setups.

After a short overview of some theoretical concepts in chapter 2, a basic single molecule experiment is presented in chapter 3 and the evaluation of experimental results is briefly discussed. The use of stirring as a provider of active transport in single molecule experiments is examined in chapter 4. Here, a model is derived to assess the influence of laminar flow on single molecule detection experiments. It is shown theoretically and experimentally that active transport by means of flow can greatly enhance the performance of such experiments and is therefore paramount to ensure efficient detection in the low-concentration regime. First experiments are presented that investigate the possibility to manipulate local flow by small, micrometer-sized artificial structures. Such structures can be used to reduce the flow-rate in confined areas or e.g. as a basic building block for mixing devices in microfluidic designs. In chapter 5 of this work, the suitability of using low-NA waveguides to detect single molecules is examined. Based on the theory of reciprocity and numerical simulations, a method to predict the performance of arbitrary dielectric waveguides is developed and verified experimentally. As an experimental realization of SMD by waveguides, a

setup based on a simple commercially available single-mode fiber is presented that is able to reliably detect fluorescent single molecules even at very low, sub-femtomolar concentration. To overcome the limiting factor of diffusion-based transport of analyte molecules in the low concentration regime, rapid and highly turbulent stirring is used. The setup offers high sensitivity at fast measurement times and a considerably lower technical complexity in comparison to other methods of similar sensitivity. Lastly, in chapter 6 the concepts of active transport through flow and dielectric waveguides are brought together. Here, microfluidic chips with integrated dielectric waveguides are used in SMD experiments. The applicability of the integrated waveguides for excitation and detection of analyte molecules in SMD experiments is investigated and different additional detection schemes are tested. Additionally the chip's property of sealing-off the sample volume from external atmosphere is used in special low-oxygen experiments aimed at chemically improving the performance of the dye used in this work. The insights gained in this chapter are then used in an outlook for an improved chip design that can be used for more efficient and integrated optical SMD experiments in lab-on-a-chip setups.

2. Theory

2.1. Principles of Fluorescence

2.1.1. Fluorescence Emission

Fluorescence denotes the spontaneous emission of a photon, e.g. by a molecule, after the prior absorption of another photon of generally shorter wavelength. This chapter intends to give only a brief overview of some aspects of fluorescence that are relevant to this thesis. For a more detailed treatise numerous volumes of literature exist to which the interested reader is referred, e.g. [26, 27, 3].

Photon emission by molecules can be illustrated by a simple three-level system as depicted in figure 2.1. It includes the basic encountered electronic states and the respective transitions between them:

1. A molecule in the singlet ground state S_0 can absorb a photon of energy $h\nu$ into the first excited singlet state S_1 with the rate k_e.

2. Transition back from S_1 to S_0 with the rate k_f, which contains radiative (k_r) and non-radiative (k_{nr}) transitions.

3. Transition from S_1 to the excited triplet state T_1, so-called *intersystem-crossing*, with the rate k_{isc}.

4. Depletion of T_1 to S_0 with the rate k_{ph}

5. Photobleaching of the molecule with the rate k_{bl}.

For fluorescence emission from an organic molecule, the ground state S_0 is equivalent to the highest occupied molecular orbital (HOMO) and S_1 corresponds to the lowest unoccupied molecular orbital (LUMO). The electronic states are superimposed with vibrational and rotational energy levels (not shown). Since thermal energy at ambient temperatures is much smaller than the separation between vibrational states, excitation of molecules typically takes place from the electronic ground state. If the energy of an absorbed photon exceeds the energy difference between electronic states, the molecule will end up in a higher vibrational energy level of S_1. Through vibrational relaxation the molecule can quickly ($10^{-12} - 10^{-10}$ s) fall back to the respective vibrational ground level (*internal conversion*). Upon the transition $S_1 \rightarrow S_0$ a photon can be emitted, resulting in *fluorescence*. This process is relatively fast, with the transition rate k_f typically being in the range of $10^7 - 10^9$ s^{-1}. Upon transition, the molecule can relax into an excited vibrational state of the electronic ground state, contributing

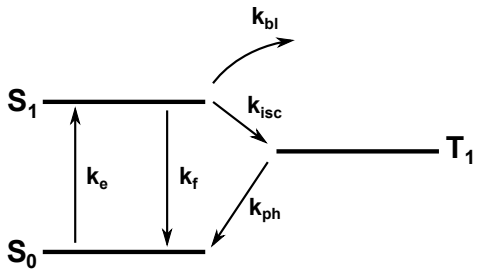

Figure 2.1.: Basic three-level system showing the different transitions between singlet ground state S_0, excited singlet state S_1 and excited triplet state T_1.

to a red-shift of the emitted fluorescence photons. The relaxation between S_1 and S_0 can also occur non-radiatively through vibration and collisions. In comparison to fluorescence, intersystem-crossing between singlet and triplet states is a much slower process in good fluorophores, with timescales of several milliseconds and in some cases up to hours. Upon intersystem crossing, the system has to undergo a spin-flip between singlet and triplet state. According to selection rules, transitions have to take place between states of the same spin multiplicity, making a singlet-triplet transition "forbidden". However, such a transition becomes possible with low probability due to small, but non-zero spin-orbit coupling encountered in molecules. Singlet-triplet transitions can lead to extended "dark" periods in the molecular emission, a behavior known as *blinking*. *Photobleaching* is made up of different processes summed up in the rate k_{bl} upon which a molecule in the excited state is deactivated or destroyed through chemical reactions.

With increasing excitation intensity I, a single emitter will cycle more rapidly through excited and ground state, until reaching a limit based upon their respective transition rates. Typically the intensity-dependent saturation behavior can be described by

$$R(I) = R_\infty \frac{I/I_S}{1 + I/I_S} \,. \tag{2.1}$$

Here R_∞ is the maximum emission rate in saturation and I_S the intensity for which $R(I) = R_\infty/2$. Equation 2.1 is plotted in figure 2.2. For saturated emission a molecule typically has to be excited with $I \geq 10 \cdot I_S$.

2.1.2. Fluorescence Resonance Energy Transfer

Fluorescence resonance energy transfer or Förster resonance energy transfer (FRET), described by T. Förster in 1948 [9] is a non-radiative energy transfer between a donor and an acceptor molecule . The donor D is excited by absorbing a photon and transferring the energy through dipole-dipole coupling to the acceptor A, which is then able to emit the energy in form of a fluorescence photon. It is necessary that the emission spectrum of the donor and absorption spectrum of the acceptor overlap (see figure 2.3a and the two fluorophores are in close proximity (typically a few nanometers). Due to

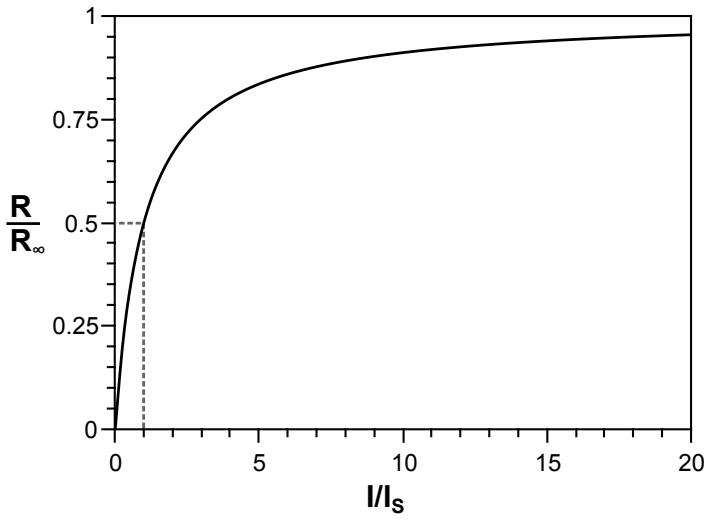

Figure 2.2.: Saturation of a fluorescent molecule depending on excitation intensity I. At an intensity value of I_S the emission by the photon is exactly half the saturation emission R_∞

coupling between the dipole moments of donor and acceptor, the efficiency of the energy transfer furthermore depends on the angle between dipole moments, with a maximum (minimum) for parallel (perpendicular) orientation [28].

The energy transfer efficiency E_τ decays with the power of 6 of the distance r between donor and acceptor and can be calculated as

$$E_\tau = \frac{R_0^6}{r^6 + R_0^6}\,, \tag{2.2}$$

where R_0 is the so-called Förster-radius, denominating the distance where the probabilities for an energy transfer D→A and a direct photon emission by the donor are equal. Figure 2.2b shows the FRET efficiency as a function of the relative distance R/R_0 between A and D.

The strong distance dependence has led to the adoption of FRET as a spectroscopic ruler used to measure inter- and intra-molecular distances [29]. Of higher importance to this work, are two other characteristics of FRET, however. The energy transfer from donor to acceptor leads to a spectral shift between excitation and emission wavelength that exceeds what is typically encountered in organic fluorophores, enabling more effective filtering of excitation light in fluorescence studies. Furthermore, the acceptor in a FRET pair can be a quenching molecule that "swallows" the excitation energy, preventing the subsequent emission of a fluorescence photon, an effect elegantly used in molecular beacons [30].

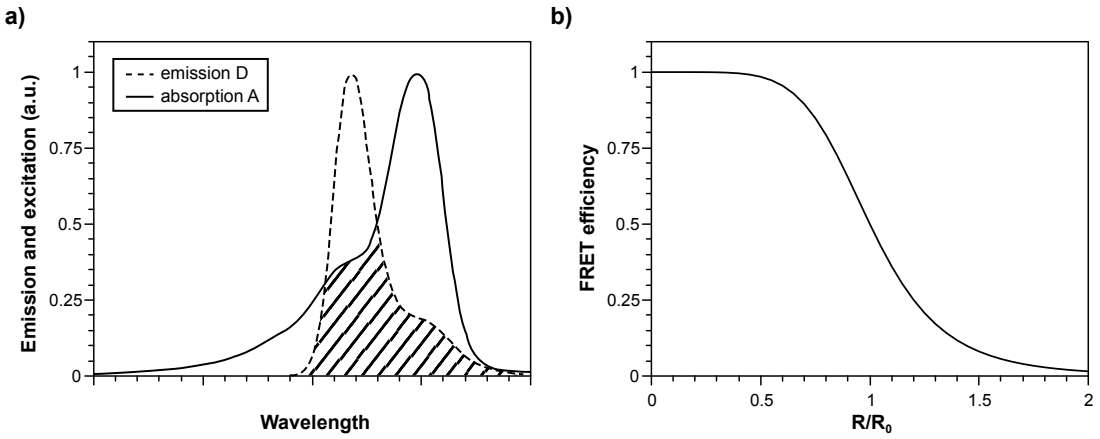

Figure 2.3.: **a)** FRET efficiency is depending on the overlap (shaded area) between the emission spectrum of the donor D and the absorption spectrum of the acceptor A. **b)** FRET efficiency depending on the relative distance R/R_0 between A and D as given by equation (2.2).

2.2. Waveguides and Optical Fibers

Waveguides in form of optical fibers today find widespread application in industry, technology and science. The ability to transmit large amounts of information encoded in light over long distances, while maintaining low losses makes them ideally suited for data transmission in the information age. Also in science, fibers are put to use in numerous different tasks, ranging from near field probes in SNOM-setups to lab-on-fiber experiments. This chapter will give an introduction to optical fibers and the phenomena behind light transmission in optical waveguides, starting with simple ray optics and then providing a brief overview of the more accurate principle of guided modes. For a more formal and in-depth treatise, the interested reader is referred to relevant literature, e.g. [31].

2.2.1. Basic Principles

The most basic optical fiber can be made from a simple thin glass cylinder. At the interface between the cylinder and the surrounding medium (e.g. air), light transmitted inside the glass can be reflected, if the angle between the incoming light wave and the surface is large enough. Such a simple fiber has several disadvantages, though, most prominently high potential losses when touching other media of similar refractive index (like another fiber), bending losses and low stability due to the fragility of the material. A typical optical fiber therefore usually resembles the schematic depiction in figure 2.4. A central, cylindrical core is surrounded by the cladding of slightly lower refractive index, which again is surrounded by a polymer coating for protection and increased stability. For single-mode fibers as used in this thesis, the core diameter is in the range of 3-5 µm, surrounded by a cladding 125 µm in diameter. The refractive

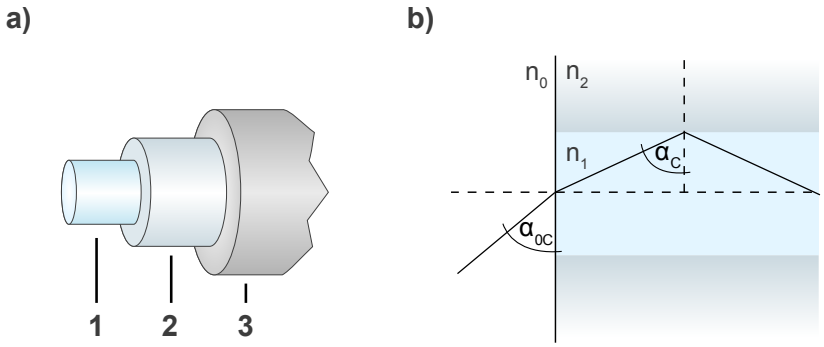

Figure 2.4.: **a)** Schematic picture of a typical optical fiber. **1**: Core, **2**: Cladding, **3**: Protective polymer coating. **b)** Light transmission by total internal reflection at the core-cladding interface and maximum incoupling angle α_{0C}.

index distribution in such a fiber is given by

$$n(r) = \begin{cases} n_1 & 0 < r < a \quad \text{(core)} \\ n_2 & r > a \quad \text{(cladding)} \end{cases} \tag{2.3}$$

where n_1 and n_2 are the refractive indices of core and cladding respectively. In actual single-mode fibers the refractive indices are similar so that

$$n_1 - n_2 \ll 1, \text{ or } n_1 \approx n_2, \tag{2.4}$$

which is called the weakly-guiding approximation and will be of importance later on.

A light beam propagating in a homogeneous dielectric medium of refractive index n_1, arriving at the boundary with a second medium of refractive index n_2, will be refracted according to well-known Snell's law as

$$n_1 \ \sin\alpha_1 = n_2 \ \sin\alpha_2, \tag{2.5}$$

where n_1 and n_2 denote the index of refraction and α_1 and α_2 the angle between light beam and the normal on the boundary layer in media 1 and 2, respectively. In the case of higher optical density of medium 2 ($n_1 < n_2$), angle α_2 will increase relative to α_1, up to $\alpha_2 = 90°$, corresponding to the critical angle

$$\alpha_C = \arcsin\frac{n_2}{n_1}.$$

At this point, the light beam cannot enter medium 2 and is reflected by 100% at the boundary, an effect known as "total internal reflection"[1]. Analogous to a light beam propagating through the fiber, a ray arriving at the fiber end from an outside medium

[1] In fact, this is not entirely correct. The beam may not be able to propagate in medium 2, but is still able to enter the medium in the form of an evanescent field with the components perpendicular to the boundary decaying exponentially (cf. [26])

n_0, will be refracted as well. It can be easily shown that the maximum angle α_{0C} (compare fig. 2.4) permitting such an incoming light ray to be reflected totally at the core/cladding boundary is depending on the refractive index difference between core and cladding as

$$\mathrm{NA} = n_0 \sin \alpha_{0C} = (n_1^2 - n_2^2)^{1/2}. \tag{2.6}$$

The dimensionless value NA is known as the numerical aperture, which provides a measure for the efficiency of the fiber to collect and transmit light rays arriving at the fiber end. Typical single-mode fibers have an numerical aperture in the range of 0.1. For the next chapter it is useful to remember that in order to ensure transport through the fiber, the maximal allowed angle between the refracted ray and the optical axis of the fiber is given by

$$\alpha_{max} = 90° - \alpha_c = 90° - \arcsin \frac{n_2}{n_1}. \tag{2.7}$$

2.2.2. Collection Efficiency in the Ray Picture

With the numerical aperture, one has a first quantity at hand to determine the ability of an optical fiber to collect light rays emitted by a source and transmit them through the fiber. However, the collection efficiency depends on the emission characteristic of the source as well. The radiation pattern from a single dye molecule in free space can be approximated by the well-known dipole pattern. In close proximity to a plane interface, e.g. the water-glass interface encountered with an immersed optical fiber, the free dipole pattern changes into an emission pattern directing the majority of emitted photons into the optically denser medium. Due to the relevance to this work, the incoupling efficiency for a single electric dipole into a single mode fiber, based on the simple ray picture discussed in the previous chapter will be briefly investigated.

Following the angular spectrum representation outlined in [26], the normalized radiation patterns of a dipole above a boundary layer between two mediums of refractive index n_0 and n_1 can be calculated. The calculations use a spherical coordinate system with the azimuthal angle ϕ and polar angle θ. The origin of the coordinate system is on the boundary layer and the dipole is located on the z-axis. The radiation pattern is then given by

$$\begin{aligned}\frac{p(\theta,\phi)}{P_0} = \frac{3\epsilon_j n_1 1}{8\pi\epsilon_1 n_j |\mu|^2} \cdot \Bigg[& \mu_z^2 \sin^2\theta \left|\Phi_j^{(1)}\right|^2 + [\mu_x \cos\phi + \mu_y \sin\phi]^2 \cos^2\theta \left|\Phi_j^{(2)}\right|^2 \\ & + [\mu_x \sin\theta - \mu_y \cos\theta]^2 \left|\Phi_j^{(3)}\right|^2 \\ & - \mu_z [\mu_x \cos\phi + \mu_y \sin\phi] \cos\theta \sin\theta \left[\Phi_j^{*(1)}\Phi_j^{(2)} + \Phi_j^{(1)}\Phi_j^{*(2)}\right]\Bigg],\end{aligned} \tag{2.8}$$

with the Phi-functions $\Phi_j^{(i)}$ defined as

$$\Phi_1^{(1)} = \left[e^{-ik_1 z_0 \cos\theta} + r^p(\theta) e^{ik_1 z_0 cos\theta}\right], \tag{2.9}$$

$$\Phi_1^{(2)} = \left[e^{-ik_1 z_0 \cos\theta} - r^p(\theta) e^{ik_1 z_0 cos\theta}\right], \tag{2.10}$$

$$\Phi_1^{(3)} = \left[e^{-ik_1 z_0 \cos\theta} + r^s(\theta) e^{ik_1 z_0 cos\theta}\right], \tag{2.11}$$

and

$$\Phi_2^{(1)} = \frac{n_1 \cos\theta}{n_0 \tilde{s}_z(\theta)} \cdot t^p(\theta) e^{ik_2[z_0 \tilde{s}_z(\theta)]}, \tag{2.12}$$

$$\Phi_2^{(2)} = -\frac{n_1}{n_0} \cdot t^p(\theta) e^{ik_2[z_0 \tilde{s}_z(\theta)]}, \tag{2.13}$$

$$\Phi_2^{(3)} = \frac{\cos\theta}{\tilde{s}_z(\theta)} \cdot t^s(\theta) e^{ik_2[z_0 \tilde{s}_z(\theta)]}. \tag{2.14}$$

The terms $r^{p,s}$ and $t^{p,s}$ are the (angle-dependent) Fresnel reflection and transmission coefficients for parallel and perpendicular polarization, respectively, and $\tilde{s}_z(\theta)$ is defined as

$$\tilde{s}_z(\theta) = \frac{k_{1z}}{k_2} = \sqrt{(n_0/n_1)^2 - \sin^2\theta}, \tag{2.15}$$

with k_{1z} the z-component of the $\mathbf{k}$ vector in the upper half space, the $\mathbf{k}$ vector in the lower halfspace k_2 and the refractive indices in the upper and lower halfspace, respectively.

In equation 2.8, P_0 corresponds to the total energy dissipation in a homogeneous medium characterized by ϵ_1 and μ_1. The first term can be identified as the p-polarized components for a vertically oriented dipole, whereas the second and third term correspond to p- and s-polarized components for a horizontally oriented dipole. The fourth term originates from interference between the p-polarized components of the horizontal and vertical orientations.

The above equations have been simplified and adapted to the case of a simple boundary layer between two dielectric media. For a more general study of stratified media, the interested reader is referred to the book by L. Novotny and B. Hecht ([26]).

Using Eq. 2.8, the total power emitted per unit solid angle $d\Omega$ is given by

$$P = \frac{p(\Omega)}{P_0} d\Omega = \frac{p(\theta,\phi)}{P_0} \sin\theta d\theta d\phi. \tag{2.16}$$

It is of some interest to have a look into which regions the dipole is emitting. Neglecting any form of power dissipation in the observed case, the total power P is

$$P = P^{\uparrow} + P_a^{\downarrow} + P_f^{\downarrow}. \tag{2.17}$$

$P^{\uparrow}$, $P_a^{\downarrow}$ and $P_f^{\downarrow}$ denotes the power emitted into the upper half-space and the allowed and forbidden zone in the lower half-space. The allowed zone is the angular region normally accessible by propagating planes waves from the upper half-space that are refracted

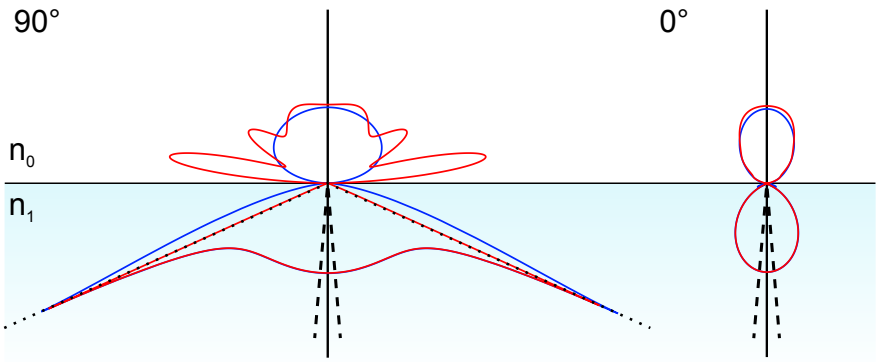

Figure 2.5.: Radiation patterns of a dipole with orientation parallel to a boundary between two dielectric media $n_0 = 1,33$ and $n_1 = 1,458$, with a distance z_0 of $0,1 \times \lambda$ (blue) and $1 \times \lambda$ (red). Patterns have been calculated by Eq. 2.8 for $\phi = 90°$ and $0°$. The dashed lines frame the power emitted in angles suitable for total internal reflection in an optical fiber of NA=0.12. Note the difference in emission into the forbidden zone (above dotted black line).

at the boundary layer. The forbidden zone is the region beyond the angle α_c for total internal reflection at the boundary layer and therefore not accessible for refracted propagating plane waves from the upper half-space. Evanescent components emitted by the dipole can not propagate in the upper half-space and will decay exponentially. In case of a lower half-space made up of a optically denser medium it is possible however, for remaining evanescent waves to be converted into propagating plane waves again. Those can be transformed into propagating plane waves in the forbidden zone. Interestingly, only the components emitted into the forbidden zone are depending on the distance z_0 between dipole and surface. The evanescent components of the dipole emission decline exponentially and can be already considered zero for distances larger than only one wavelength (cf. figure 2.5). On the other hand, the emission into the allowed zone does not depend on the distance between dipole and surface.

The fraction P_t of the total power emitted by the dipole that can be coupled into and transmitted through an optical fiber can be calculated by (numerically) integrating Eq. 2.16 over the range of angles suitable for total internal reflection at the core/cladding interface of the fiber:

$$P_t = \frac{1}{P_0} \int_0^{\alpha_{max}} \int_0^{2\pi} p(\theta, \phi) \sin\theta d\theta d\phi \,, \tag{2.18}$$

with the value α_{max} from Eq. 2.7 used as upper boundary for θ in the integral. Using typical values for an optical single-mode fiber, the resulting total incoupled power for a dipole oriented parallel to the boundary is $\approx 0,3\%$.

This value can be used as a reasonable approximation for the incoupling efficiency of a waveguide, but leaves some open questions. The calculation in this section does not

factor in the distance between emitter and waveguide outside of the contribution of evanescent fields - it is apparent, however, that the fraction of incoupled light should eventually decrease with distance. Likewise, no provision is made for a displacement of the emitter parallel to the waveguide surface. Can the collection efficiency be really considered uniform across the entire waveguide surface? Describing the transmission of light through an optical fiber in the simple picture of propagating rays reflected by total internal reflection is strictly speaking only valid for multi-mode fibers, while single-mode waveguides such as those used in this work are characterized by guiding modes. This will be briefly discussed in the next chapter.

2.2.3. Fiber Modes

An analysis of single-mode fibers requires a description by propagating modes of light. A complete treatise can be easily found in the literature ([31, 32, 33]), while only some results important for the scope of this work will be presented here. The complete transverse field for a mode propagating in z-direction in an optical fiber can be written as

$$\Psi_l(r,\phi,z,t) = \Psi(r)\cdot e^{i(\omega t-\beta z)}\cdot \begin{Bmatrix}\cos(l\phi)\\ \sin(l\phi)\end{Bmatrix}, \tag{2.19}$$

where r and ϕ are the cylindrical coordinates, ω the angular frequency, β the propagation constant and l is a constant.

Using the weakly guiding approximation (equation 2.4), the radial part of the field is defined by

$$\frac{d^2\Psi_l(r)}{dr^2}+\frac{1}{r}\frac{d\Psi_l(r)}{dr}+\left(k^2n^2-\beta^2-\frac{l^2}{r^2}\right)\Psi_l(r)=0, \tag{2.20}$$

which is a Bessel differential equation. For this work the analysis will be restricted to the case where $l=0$, i.e. the fundamental mode in a single-mode fiber. Equation 2.20 can be re-written as

$$\frac{d^2\Psi_l(r)}{dr^2}+\frac{1}{r}\frac{d\Psi_l(r)}{dr}+\left(\frac{U^2}{a^2}-\frac{l^2}{r^2}\right)\Psi_l(r)=0 \tag{2.21}$$

and

$$\frac{d^2\Psi_l(r)}{dr^2}+\frac{1}{r}\frac{d\Psi_l(r)}{dr}-\left(\frac{W^2}{a^2}+\frac{l^2}{r^2}\right)\Psi_l(r)=0 \tag{2.22}$$

Here U and W are defined as

$$W = V\sqrt{b} \quad \text{and} \tag{2.23}$$

$$U = V\sqrt{1-b}, \tag{2.24}$$

with the normalized propagation constant b

$$b = \frac{\beta^2/k_0^2 - n_{cl}^2}{n_{co}^2 - n_{cl}^2} = \frac{W^2}{V^2}, \tag{2.25}$$

and the normalized waveguide parameter V.

$$V = (U^2 + W^2)^{1/2} = k_0 a \sqrt{n_{co}^2 - n_{cl}^2} = k_0 a \cdot \mathrm{NA} \tag{2.26}$$

The solutions to equations 2.21 are Bessel functions of the form $J_l(x)$ and $Y_l(x)$, but since $Y_l(x)$ diverges for $x \to 0$, it has to be rejected. Likewise the modified Bessel functions $K_l(x)$ and $I_l(x)$ are the solutions of 2.22, where again $I_l(x)$ has to be rejected as it diverges for $x \to \infty$. Demanding continuity of Ψ at the core-cladding interface and neglecting higher-order modes, the complete solution of the fiber mode field for l=0 is therefore given by

$$\Psi(r) = \begin{cases} \frac{A}{J_0(U)} J_0(\frac{Ur}{a}); & r < a \\ \frac{A}{K_0(W)} K_0(\frac{Wr}{a}); & r > a \end{cases} \tag{2.27}$$

Assuming continuity of $\partial\Psi/\partial r$ at the core-cladding interface, it can be shown that for the case where l=0

$$U \frac{J_1(U)}{J_0(U)} = W \frac{K_1(W)}{K_0(W)}\,. \tag{2.28}$$

Substituting with equation 2.23, this equation can be solved numerically for b, yielding the solutions for U and W. With that, the mode-field profile in a single mode fiber can be calculated. Assuming a fiber of the type used in this work (FS-SN-3224, Thorlabs), with a mode-field diameter (MFD) of 4 µm ± 0.5 µm and NA=0.12 at a wavelength of 630 nm, the resulting mode-field is plotted in figure 2.6 for a wavelength of 630 nm (the design case) and 800 nm. Additionally the commonly-used approximation of the mode-field by a Gaussian distribution is shown. While the gaussian approximation yields good results for many purposes, it is necessary to use the more accurate description by Bessel functions under certain circumstances, such as giving an accurate account of the outcoupled intensity distribution of a fiber mode.

2.2.4. Propagation of Outcoupled Waveguide Modes

Central parameters for the detection of single molecules are the size and shape of the detection volume, i.e. the volume within efficient detection of single molecules can be achieved. If a single emitter (e.g. a fluorescent molecule or quantum dot) is excited by light outcoupled from a waveguide, the local intensity distribution will influence the emission rate of that emitter and consequently the number of detectable photons. While microscope objectives offer a comparatively sharp confinement of the detection volume inside the focal region, the distribution of the fields outcoupled from waveguides such as optical fibers is more difficult to characterize.

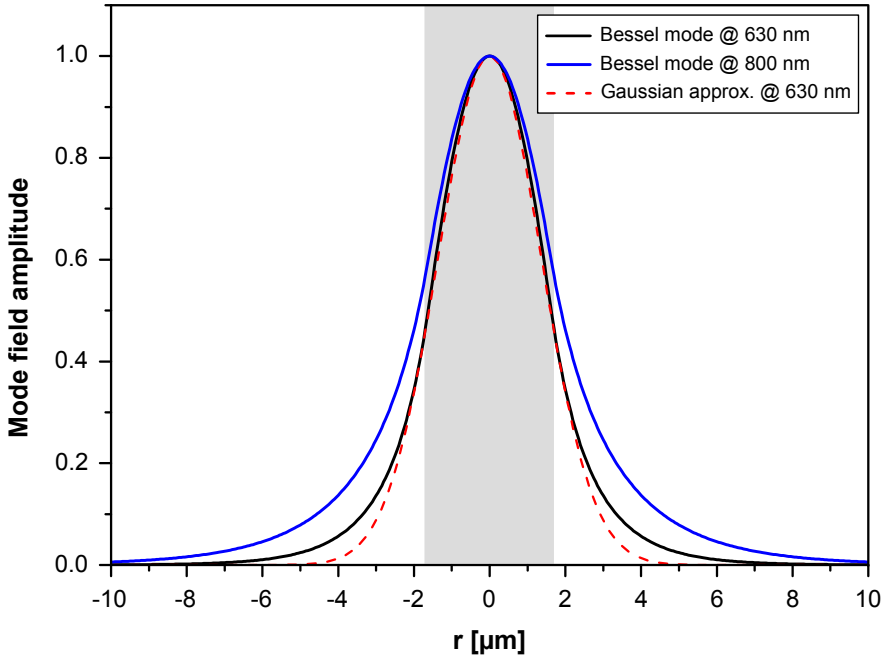

Figure 2.6.: Resulting radial amplitude of the mode-field for a fiber with a MFD of ≈4 µm at 630 nm and NA=0.12. The black curve is the resulting mode for 630 nm, the blue curve is the result obtained for 800 nm. The red dashed line indicates the commonly used approximation of the mode by a gaussian mode profile. The gray area indicates the fiber core. Note that a significant portion of the modes extend into the cladding and the broadening of the mode for longer wavelengths.

Analytical calculation of outcoupled fields To determine the field distribution of an outcoupled fiber mode described by equation 2.27, the propagation of Bessel beams is investigated. Bessel beams have been postulated by Durnin [34], as solutions to the scalar wave equation resulting in non-diffracting beams, with radial intensity distributions characterized by a Bessel function. Since each side-lobe in the 2D-Bessel function that determines the intensity distribution of the beam carries the same power as the central maximum, an ideal Bessel beam would carry infinite power and is therefore unphysical. It is however possible to approximate such beams experimentally by limiting the number of contributing side-lobes [35]. In the case of a single mode waveguide such as the optical fiber described earlier, the Bessel beam will be very short-lived, since it is constructed purely by the central maximum as described by J_0 within the core and the continuously decaying function K_0 within the cladding.

To calculate the field distribution after the fiber as resulting from the fiber mode, the free space Huygens-Fresnel diffraction integral [36] is utilized by using a slightly modified method as outlined in [37] and [38]. An expression for the intensity in the

half space after the fiber is obtained as

$$I(r,z) = |E(r,z)|^2 = \left(\frac{k}{z}\right)^2 \left| \int \rho \Psi(\rho) J_0\left(\frac{k\rho r}{z}\right) \exp\left(\frac{ik\rho^2}{2z}\right) \mathrm{d}\rho \right|^2 , \tag{2.29}$$

where $k = \omega/c$ is the wavenumber, ρ the distance from the optical axis over which the integral is evaluated and Ψ the fiber mode according to equation 2.27.

For r=0, the central beam-intensity along the optical axis of the fiber is obtained, resulting in

$$I(0,z) = |E(0,z)|^2 = \left(\frac{k}{z}\right)^2 \left| \int_0^a \rho \Psi(\rho) \exp\left(\frac{ik\rho^2}{2z}\right) \mathrm{d}\rho \right|^2 . \tag{2.30}$$

The normalized intensity distribution with increasing distance is shown in figure 2.7. Alongside are the similar results from simulations of a guiding mode outcoupled from an optical fiber obtained through FDTD (Finite Difference Time Domain) simulations, which will be presented and discussed in detail in chapter 5. Most notably, the intensity distribution has a small maximum ≈ 3 µm behind the fiber surface. This behavior reminds of a focusing effect and can be explained by the short-ranged Bessel beam directly after the fiber facet exhibiting typical intensity oscillations. Eventually the Bessel beam breaks down, starts to diverge and gradually approaches the behavior of a Gaussian beam with a divergence compatible with the fiber's numerical aperture (NA = 0.12).

2.2.5. Mode-matching and Reciprocity

In this section it will be shown that by using the reciprocity theorem of electromagnetic theory, the spatial distribution of the photon collection efficiency or incoupling efficiency of single-mode waveguides can be determined directly from the intensity distribution of the outcoupled light. In short, knowing the field distribution outside of an arbitrary single-mode waveguide created by the outcoupled field of the fundamental waveguide mode, the detection efficiency of this waveguide can be calculated for arbitrary positions of an emitting dipole.

A radiating single emitter (SE) - a dye molecule, quantum dot, or any other quantum emitter - is considered which is located close to the end facet of a single-mode waveguide (W) - an on-chip waveguide or an optical fiber - supporting a single guided mode $\boldsymbol{\Psi}_1$ with fields $\boldsymbol{E}_1$ and $\boldsymbol{H}_1$ (see figure 2.8a). The SE is described as a radiating point dipole situated at $\boldsymbol{r}_0$ with dipole moment $\boldsymbol{p}$ that radiates corresponding fields $\boldsymbol{E}_{SE}$ and $\boldsymbol{H}_{SE}$ [39]. To determine the overall detection efficiency of the system an important figure of merit is the fraction of power coupled from the radiating SE to the waveguide, described by the in-coupling efficiency $\eta(\boldsymbol{r}_0, \boldsymbol{p})$ - a quantity that is usually determined by mode matching, which is derived according to [40]. In general, any arbitrary field distribution within a waveguide can be decomposed into the complete basis of waveguide modes, which include a finite number of guided (bound) modes and

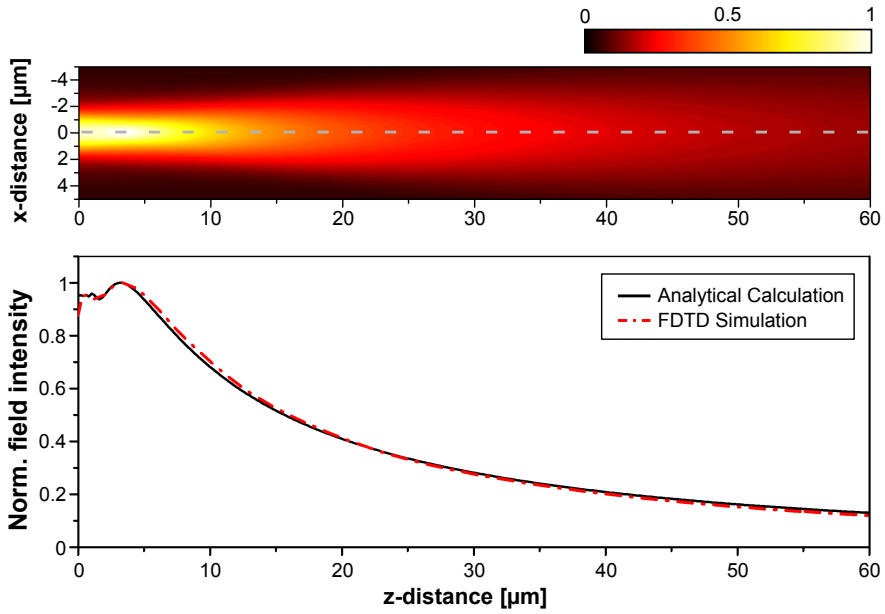

Figure 2.7.: Simulated field-intensity resulting from an outcoupled fiber mode in the half-space behind a single-mode fiber (upper picture) and linecut through the central part of the intensity distribution (dashed line, resulting intensity in lower diagram). The fiber end-facet is at z=0. The solid black line is the analytical result from equation 2.30, the red dashed line is the respective result from FDTD simulations.

a continuum of radiating modes. Applied to the present case, the input fields $\boldsymbol{E}_{SE}$ and $\boldsymbol{H}_{SE}$, generated by radiating SE inside the optical fiber, can thus be written as

$$\boldsymbol{E}_{SE}(\boldsymbol{r}) = \sum_i a_i \boldsymbol{E}_i(\boldsymbol{r}) + \boldsymbol{E}_{rad}(\boldsymbol{r})$$
$$\boldsymbol{H}_{SE}(\boldsymbol{r}) = \sum_i b_i \boldsymbol{H}_i(\boldsymbol{r}) + \boldsymbol{H}_{rad}(\boldsymbol{r})$$

where $\boldsymbol{E}_i$ and $\boldsymbol{H}_i$ are the fields of the i-th guided mode, and $\boldsymbol{E}_{rad}$ and $\boldsymbol{H}_{rad}$ represent the radiating modes. Using the fiber modes' orthogonality

$$\frac{\int_A \boldsymbol{E}_i \times \boldsymbol{H}_j^* \cdot \hat{\boldsymbol{z}}\, \mathrm{d}A}{\int_A \boldsymbol{E}_i \times \boldsymbol{H}_i^* \cdot \hat{\boldsymbol{z}}\, \mathrm{d}A} = \delta_{ij}$$

the modal amplitudes a_i and b_i are defined as

$$a_i = \frac{\int_A \boldsymbol{E}_{SE} \times \boldsymbol{H}_i^* \cdot \hat{\boldsymbol{z}}\, \mathrm{d}A}{\int_A \boldsymbol{E}_i \times \boldsymbol{H}_i^* \cdot \hat{\boldsymbol{z}}\, \mathrm{d}A}$$
$$b_i^* = \frac{\int_A \boldsymbol{E}_i \times \boldsymbol{H}_{SE}^* \cdot \hat{\boldsymbol{z}}\, \mathrm{d}A}{\int_A \boldsymbol{E}_i \times \boldsymbol{H}_i^* \cdot \hat{\boldsymbol{z}}\, \mathrm{d}A}$$

Using the definition of the time-averaged Poynting vector the total power propagating inside the fiber is then given by

$$\begin{aligned} P &= \frac{1}{2} Re\left(\int_A \boldsymbol{E}_{SE} \times \boldsymbol{H}_{SE}^* \cdot \hat{\boldsymbol{z}}\, \mathrm{d}A\right) \\ &= \frac{1}{2} \sum_i Re\left(a_i b_i^* \int_A \boldsymbol{E}_i \times \boldsymbol{H}_i^* \cdot \hat{\boldsymbol{z}}\, \mathrm{d}A\right) \end{aligned}$$

and therefore the fraction of power propagating in the i-th mode is

$$\begin{aligned} \frac{P_i}{P_0} &= \frac{1}{2P_0} Re\left(a_i b_i^* \int_A \boldsymbol{E}_i \times \boldsymbol{H}_i^* \cdot \hat{\boldsymbol{z}}\, \mathrm{d}A\right) \\ &= \frac{1}{2P_0} Re\left(\frac{\int_A \boldsymbol{E}_i \times \boldsymbol{H}_{SE}^* \cdot \hat{\boldsymbol{z}}\, \mathrm{d}A \cdot \int_A \boldsymbol{E}_{SE} \times \boldsymbol{H}_i^* \cdot \hat{\boldsymbol{z}}\, \mathrm{d}A}{\int_A \boldsymbol{E}_i \times \boldsymbol{H}_i^* \cdot \hat{\boldsymbol{z}}\, \mathrm{d}A}\right) \end{aligned}$$

Since the waveguides and fibers considered in this work support only a single guided fiber mode, $i = 1$, thus leading to:

$$\eta = \frac{1}{2P_0} Re\left(\frac{\int_A \boldsymbol{E}_1 \times \boldsymbol{H}_{SE}^* \cdot \hat{\boldsymbol{z}}\mathrm{d}A \cdot \int_A \boldsymbol{E}_{SE} \times \boldsymbol{H}_1^* \cdot \hat{\boldsymbol{z}}\mathrm{d}A}{\int_A \boldsymbol{E}_1 \times \boldsymbol{H}_1^* \cdot \hat{\boldsymbol{z}}\mathrm{d}A}\right) \tag{2.31}$$

Here A denotes the area of the waveguide end face, $\hat{\boldsymbol{z}}$ the unit vector parallel to the waveguide, and P_0 the SE's overall radiated power. In a general single-molecule detection experiment in complex environments and with diffusing SEs, the determination of η for multiple SE positions and orientations requires a new dipolar field calculation/simulation for every configuration to determine the fields $\boldsymbol{E}_{SE}$ and $\boldsymbol{H}_{SE}$ at A. It will now be shown that η can be determined for arbitrary locations and orientations of a SE relative to the waveguide with a single field simulation even for a complex environment. The key to this simplification is the application of the reciprocity theorem that can be used once the electric field $\boldsymbol{E}_W$, emitted by the waveguide end face when fed with the mode fields, is known. The Lorentz-formulation of electromagnetic reciprocity [41],

$$\int \boldsymbol{E}_m \cdot \boldsymbol{J}_n\, \mathrm{d}V_n = \int \boldsymbol{E}_n \cdot \boldsymbol{J}_m\, \mathrm{d}V_m \tag{2.32}$$

connects two electrical currents $\boldsymbol{J}_{m/n}$ and their respective radiated electric fields $\boldsymbol{E}_{m/n}$ in two finite volumes $V_{m/n}$ separated by an arbitrary environment consisting of particles and/or half-spaces described by linear dielectric constants ϵ (see Fig. 2.8b). Considering the definition of the electrical power, it is possible to write

$$P_{el} = \int \boldsymbol{E} \cdot \boldsymbol{J}\, \mathrm{d}V \tag{2.33}$$

Equation 2.32 shows that, when the tasks of the particles as sender and receiver are

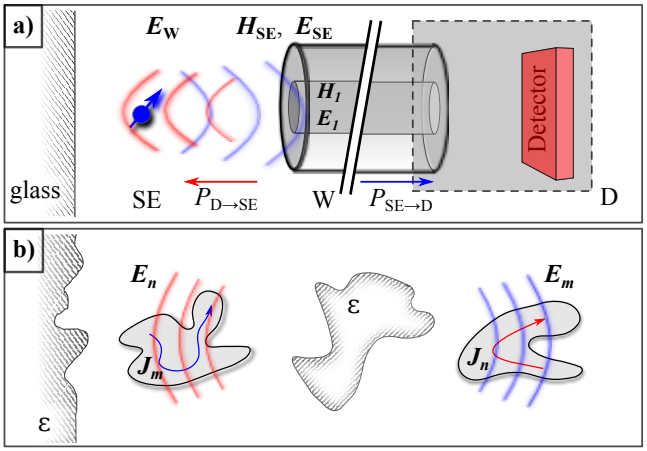

Figure 2.8.: General experimental setting: **(a)** A single emitter (SE) is placed next to the facet of a lossless single-mode waveguide (W), whose mode is described by fields $\boldsymbol{H}_1$ and $\boldsymbol{E}_1$. The far end of the fiber combined with the connected detection assembly is treated as detector (D) receiving all power $P_{SE\to D}$ transmitted through W via the fields $\boldsymbol{H}_{SE}$ and $\boldsymbol{E}_{SE}$. In order to make use of reciprocity the detector is assumed to emit light as ideal sender exciting the SE with the field $\boldsymbol{E}_W$ transporting the power $P_{D\to SE}$. The lower panel **(b)** sketches a general setting for which reciprocity can be formulated: two source currents $\boldsymbol{J}_{m/n}$ originating in volumes $V_{m/n}$ result in respective far fields $\boldsymbol{E}_{m/n}$, containing also fields reflected and diffracted by the environment described by ϵ. Figure from [2], © 2014 American Physical Society.

exchanged (time reversal symmetry), the transmitted power remains the same:

$$P_{el,m\to n} = P_{el,n\to m} \tag{2.34}$$

Now particle M is identified with the SE. It is situated near the end of a lossless single-mode fiber W whose far end is directly connected to a photon detector (Fig. 2.8a). For simplicity particle N subsumes the combination D of the detection device assembly and the connected fiber, assuming all power in the fiber mode will be detected. In the reciprocal case, D therefore is a perfect sending device coupling all power into the fiber mode $\boldsymbol{E}_1$ leading to the field $\boldsymbol{E}_W$ emitted from the fiber facet and exciting the SE. To calculate the deposited electrical power one has to insert the source current of a point dipole $\boldsymbol{J}_{SE} = \mathrm{i}\omega\boldsymbol{p}\,\delta(\boldsymbol{r}-\boldsymbol{r}_0)$ into eq. 2.33. One finds:

$$\begin{aligned} P_{SE\to D} &= \int \boldsymbol{E}_W\cdot\boldsymbol{J}_{SE}\,\mathrm{d}V = \int -\mathrm{i}\omega\boldsymbol{p}\cdot\boldsymbol{E}_W\delta(\boldsymbol{r}-\boldsymbol{r}_0)\,\mathrm{d}V \\ &= -\mathrm{i}\omega\boldsymbol{p}\cdot\boldsymbol{E}_W(\boldsymbol{r}_0) \end{aligned} \tag{2.35}$$

Inserting eq. 2.35 in eq. 2.32 and writing the dipole moment for an excited single

emitter as $\boldsymbol{p} = \bar{\bar{\boldsymbol{\alpha}}} \cdot \boldsymbol{E}(\boldsymbol{r}_0)$ [26] using the SE's polarizability tensor $\bar{\bar{\boldsymbol{\alpha}}}$ yields the final result:

$$P_{SE \to D} = -\mathrm{i}\omega \bar{\bar{\boldsymbol{\alpha}}} \cdot \boldsymbol{E}_W^2(\boldsymbol{r}_0) = P_{D \to SE} \tag{2.36}$$

This implies that once the vector field $\boldsymbol{E}_W$ emitted from the fiber facet is known for a given environment, which can be determined by a single calculation or simulation, also the power of a point dipole coupled into the fiber mode is known for all its possible positions and orientations. Using equation 2.36, η can now be written as

$$\eta = P_{SE \to D} / P_0 \tag{2.37}$$

Thus it is possible to calculate the incoupling efficiency for arbitrary positions when the field distribution originating from an outcoupled waveguide mode is known. To obtain the field distribution, the approach from section 2.2.4 can be used in case of simple geometries. Alternatively the field distribution can be determined through simulations, which additionally opens up the possibility to analyze complicated geometries. Contrary to the ray-optics approximation used in section 2.2.2, this method considers waveguide modes and yields the complete spatial distribution of the incoupling efficiency. In chapter 5 it will be confirmed through experiments and applied to determine the efficiency of a fiber-based single-molecule sensor.

2.3. Diffusion and Flow

Every method for single-molecule detection relies on the transport of molecules into a specific volume or to an active area where the molecule can be detected by the respective detection scheme. Molecules can be transported passively through diffusion, i.e. by random Brownian motion, or through some active process, typically flow of the sample containing the analyte molecules. Other more elaborate concepts are regularly employed as well, notably in the form of preconcentration of analyte molecules [24]. This chapter will provide a short overview over those aspects of diffusion and active flow that are relevant to this thesis.

2.3.1. Diffusion

In his 1905 publication on the movement of small particles in liquids [42], Einstein derived an expression for the mean squared displacement of a diffusing particle. Adjusted for diffusive motion in more than one dimension (Einstein derives the expression for movement along the x-axis), the mean displacement during the time t is given by

$$\langle r^2(t) \rangle = 2nDt \,, \tag{2.38}$$

where n is the numbers of dimensions open to diffusion and D is the particle's diffusion coefficient. For particles in solution D can be calculated through the Stokes-Einstein

equation, which can be found in the same publication, as

$$D = \frac{k_B T}{6\pi\eta R_0} \,. \tag{2.39}$$

Here the hydrodynamic radius R_0 has been used, which is the radius of a hypothetical sphere with the same diffusive properties as the diffusing molecule or particle. η is the dynamic viscosity of the solvent.

2.3.2. Molecule Arrival Time in Diffusion-limited Measurements

In absence of a form of active transport (e.g. a steady flow of the liquid sample through the detection volume of a SMD experiment), one has to rely on diffusion for molecules to reach the detection volume. For a high concentration of analyte molecules and a comparatively large detection volume, the average time until a molecule reaches the volume will be comparatively small. However, typical SMD experiments are characterized by a small detection volume, which is necessary to ensure single-molecule conditions and to reduce unwanted background signal. In combination with very low analyte concentrations encountered in many problems of interest, it is expected that the average arrival times reach large values. This is illustrated in figure 2.9, where three different concentrations of analyte molecules in solution are shown. Within time t, the freely diffusing molecules can reach positions within an area of the radius defined by equation 2.38. The probability to encounter the molecule at a given position is indicated by color density. With decreasing concentration less molecules can potentially reach the detection volume, as outlined by the red elliptical area, in time t. Consequently the observation time has to be increased to compensate.

Here an approximation is presented to estimate the arrival times encountered in diffusion-based experiments. The method was developed by W. Grange and S. Zorman and first published in [1].

For a diffusion coefficient D, which is independent of the concentration c, Fick's (second) law states

$$\frac{\partial c}{\partial t} = D\nabla^2 c \,. \tag{2.40}$$

Assuming the detection volume to be a sphere of radius a and rewriting 2.40 using spherical coordinates yields

$$\frac{\partial c}{\partial t} = D\frac{1}{r^2}\frac{\partial}{\partial r}\left(r^2\frac{\partial c}{\partial r}\right) \,. \tag{2.41}$$

For the stationary case this equation reads as

$$\frac{\partial c}{\partial t} = 0 \,. \tag{2.42}$$

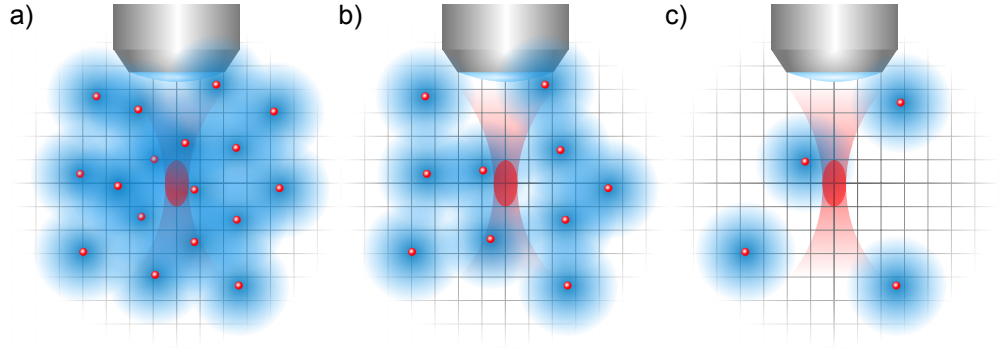

Figure 2.9.: Illustrating the basic problem of diffusion-limited single-molecule detection: The area accessible within time t to freely diffusing molecules in a liquid sample volume is depicted by blue shaded areas. Color density indicates probability density to encounter a molecule at this position after time t. With decreasing concentration (from a to c) less molecules will be able to potentially reach the detection volume (red elliptic area) within time t.

It is now assumed that the concentration within the detection volume is zero at any given time (i.e. once a molecule enters the detection volume, it is instantly bleached) and that the concentration is c_0 for $r >> a$. The concentration can then be written as

$$c(r) = c_0 \left(1 - \frac{a}{r}\right) . \tag{2.43}$$

Fick's first law can be used to calculate the diffusive flux J driven by a concentration gradient

$$J(a) = -D\frac{\partial c}{\partial r} \tag{2.44}$$

Calculating the total flux leads to

$$J = 4\pi a D c_0 \tag{2.45}$$

which can be used to estimate the total number of molecules reaching the sphere during the time t by $J \times t$. The probability $P(k, \lambda)$ for k occurrences at an expected number of λ occurrences during the time interval t is given by the Poisson distribution

$$P(k, Jt) = \frac{e^{-Jt}(Jt)^k}{k!} . \tag{2.46}$$

The average time it takes to observe a molecule corresponds to the average time for which no molecule is in the detection volume. The probability for zero molecules in a time interval t is

$$P(0, Jt) = e^{-Jt} . \tag{2.47}$$

The average time therefore reads as

$$\langle t \rangle = \frac{1}{\int_0^\infty P(0, Jt)dt} \cdot \int_0^\infty tP(0, Jt)dt = \frac{1}{4\pi a D c_0} \,. \tag{2.48}$$

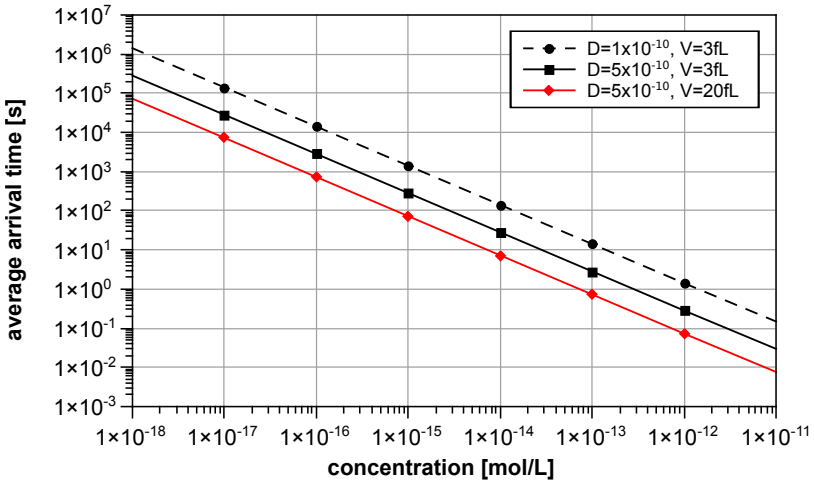

Figure 2.10.: Average time until a molecule enters the detection volume using equation 2.48. The black line (squares, circles) is calculated for a volume of 3 fL and diffusion coefficients $D = 1 \cdot 10^{-10}$ m^2/s (dashes) and $D = 5 \cdot 10^{-10}$ m^2/s (solid). The red line (diamonds) for a volume of 20 fL and $D = 5 \cdot 10^{-10}$ m^2/s.

In figure 2.10, equation 2.48 is used to calculate the average time it takes until a molecule reaches a 3 fL (corresponding to an objective-based setup) and 20 fL volume (corresponding to a waveguide-based detection scheme) for different values of the diffusion coefficient D. For bigger molecules reasonable values for D range between $1 \cdot 10^{-10}$ m^2/s and $5 \cdot 10^{-10}$ m^2/s. For this case, single molecule detection by diffusion will be limited to concentrations above roughly 10 fM, as for lower concentrations the average time until a molecule will be detected quickly reaches several tens of minutes to hours.

2.3.3. Laminar Flow over Surfaces

In this thesis, a special emphasis is put on single molecule detection under conditions of flow. It is therefore of interest to take a look at the analytic descriptions of some of the cases encountered in the respective experiments. Since a thorough analysis of the flow in realistic non-trivial systems, especially in presence of turbulence, is outside the scope of this work, the presented theory will be limited to laminar flow in model systems. This chapter will focus on applications of laminar flow which can be encountered in similar fashion in the experimental part of the thesis.

The Reynolds Number *Re* A useful parameter for the characterization of flows is the dimension-less Reynolds-number Re, describing the ratio of inertial to viscous forces.

$$Re = \frac{\rho v l}{\eta} = \frac{v l}{\nu} \,. \tag{2.49}$$

Here ρ is the density of the fluid, v the velocity, η and ν the dynamic and kinematic viscosity[2], respectively. The parameter l describes the characteristic length of the observed system, e.g. the diameter of a pipe where a fluid is passing through, or the length of a plate in a flow. If inertial forces can be neglected and viscous forces dominate (small Re), generally laminar flow is encountered. If inertial forces are dominating (large Re) the flow will become turbulent. The absolute value of Re, marking the transition between laminar and turbulent flow, depends on the system in question. For example turbulence may occur inside a pipe for $Re \approx 2000$, but only for $Re \approx 10^5$ in the case of fluid flowing over a plate. Another property of the Reynolds-number is its use in hydrodynamic similarity - two geometrically similar systems of different dimension will behave similar if their Reynolds numbers are the same [43]. This concept is widely exploited in wind tunnel experiments with small-scale models.

Flow through a cylindrical channel The flow profile encountered in the channels of microfluidic chips can be approximated by using the well-known parabolic profile of a laminar flow through a cylindrical channel [44]. The flow velocity is assumed to be zero at the channel walls due to friction between the fluid molecules and the channel surface (the so-called "no slip condition" [45]) and then gradually increases towards the center of the channel, resulting in a parabolic velocity profile. The flow velocity $u(r)$ in dependence of the radius r (in cylindrical coordinates) is then given as

$$u(r) = u_{max} \left[1 - (r/R)^2\right] \,. \tag{2.50}$$

Here, R is the diameter of the channel and u_{max} the maximum of the velocity encountered at $r = 0$.

Boundary layer theory Another approach of interest to this thesis is the boundary layer theory, describing the flow of a fluid over the surface of an object. Similar situations are encountered e.g. in measurements where a microscope objective is focusing into a sample volume with a constant flow. The origin of the boundary layer is the friction of the fluid molecules at the object surface. Assuming that the velocity of the utmost layer of molecules is the same as that of the surface due to friction at the surface, the lower friction between fluid molecules will lead to a gradual increase in flow velocity with increasing distance from the surface, asymptotically approaching the undisturbed velocity u_∞. For mathematical treatment of the boundary layer it is useful to define a threshold distance δ where the local velocity of the flow over the surface has reached a certain fraction of u_∞. The conventionally used ratio is 99%

[2]Dynamic and kinematic viscosity are related to each other as $\eta = \nu \cdot \rho$

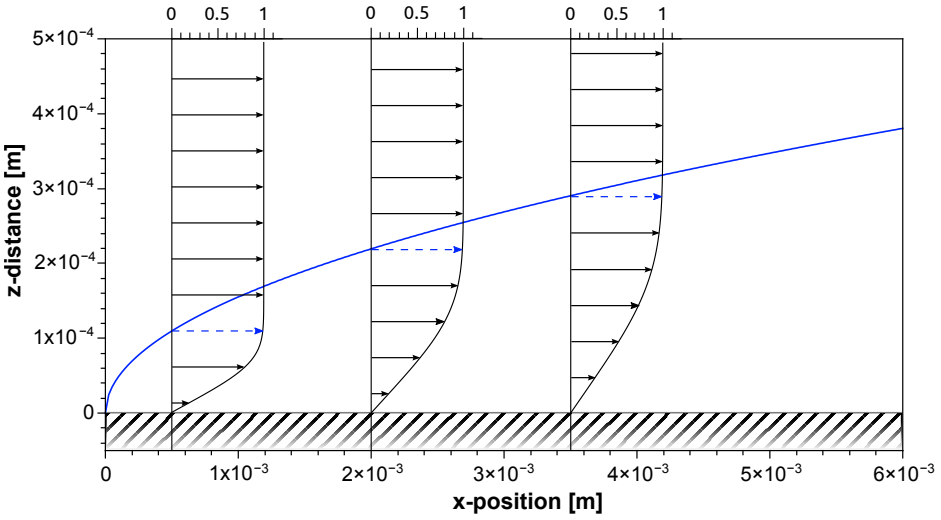

Figure 2.11.: Flow over a semi-infinite plate as described by the boundary layer model. The undisturbed parallel flow with $u_\infty = 1$ encounters the plate at x=0. Solving the Blasius equation leads to expressions for the boundary layer thickness (blue line) and the local flow velocity $u(x, z)$ along the plate (insets). The blue arrows indicate the local velocity at the boundary $\delta_{99}(x)$. For small enough distances from the surface, velocity is increasing linearly along the z-direction.

(denominated as δ_{99}). Disregarding the transition zone, the flow inside the boundary layer is affected by friction, while outside the boundary friction can be neglected.

To find an expression for the thickness δ of the boundary layer, a flat semi-infinite plate which is placed in an undisturbed parallel flow at x=0 is considered. The Navier-Stokes equation of fluid mechanics can then be written in form of the boundary layer equation as first described by Prandtl in 1904 [44]:

$$\begin{aligned} u\frac{\delta u}{\delta x} + v\frac{\delta u}{\delta y} &= -\frac{1}{\rho}\frac{\delta p}{\delta x} + u\frac{\delta^2 u}{\delta y^2}\,, \\ 0 &= \frac{\delta p}{\delta y}\,, \\ \frac{\delta u}{\delta x} + \frac{\delta v}{\delta y} &= 0\,. \end{aligned}$$

Here u is the velocity in x-direction, v the velocity in y-direction, ρ is the fluid density and p the pressure. From this equation, the Blasius differential equation can be derived [44].

$$2f''' + ff'' = 0 \tag{2.51}$$

Solving the Blasius equation analytically is not possible, but numerical solutions do

exist. By solving the differential equation, an expression for the thickness δ_{99} of the boundary layer in dependence of u_∞ and the position along the plate can be found to be

$$\delta_{99}(x) = 4.91 \cdot \sqrt{\frac{\eta x}{\rho u_\infty}} \approx 5 \cdot \sqrt{\frac{\eta x}{\rho u_\infty}} = \frac{5x}{\sqrt{Re}} \,. \tag{2.52}$$

Additionally an expression for the behavior of the flow velocity within the boundary layer, $u(x, z)$ can be derived. In figure 2.11 the results from solving equation 2.51 for $\delta_{99}(x)$ and $u(x, z)$ are depicted, showing the square-root dependence of the boundary layer thickness on the x-coordinate. For small distances above the surface ($y \leq 1/2 \cdot \delta_{99}(x)$), the local flow velocity increases linearly with distance from the surface (see insets of figure 2.11).

2.4. Fluorescence Correlation Spectroscopy

Fluorescence Correlation Spectroscopy (FCS) is an optical microscopy technique which can be used to gain insight into the dynamic properties of a system by statistical analysis of intensity fluctuations. FCS has been developed in the early seventies by Magde et al. [46]. In 1993 Rigler et al. [47] were able to demonstrate the capability of FCS as a method for single-molecule detection. Further aided by the development of improved light sources and single-photon detectors, FCS has since found wide-spread adaption in research, especially, but not limited to, biological sciences. For a short overview and current trends in FCS, see e.g. [48]. The basic and commonly found FCS setup uses a confocal epifluorescence microscope to detect fluorescent molecules in a small, usually sub-femtoliter volume. From the recorded time trace of the fluorescence signal $F(t)$, the auto-correlation, i.e. the correlation of the time series with itself, shifted by time τ can then be calculated as

$$G(\tau) = \frac{\langle \delta F(t) \delta F(t+\tau) \rangle}{\langle F(t) \rangle^2} = \frac{\langle F(t) F(t+\tau) \rangle}{\langle F(t) \rangle^2} - 1, \tag{2.53}$$

where $\langle F(t) \rangle = 1/T \int_0^T F(t) \mathrm{d}t$ is the time average of the signal and $\delta F(t) = F(t) - \langle F(t) \rangle$ are the fluctuations around the mean value. The result is a measure for the self-similarity of the recorded signal at increasing time-delay or in other words the probability that the value at $F(t+\tau)$ originates from the same event as the value at $F(t)$. A typical auto-correlation from a fluorescence measurement of diffusing molecules is shown in fig. 2.12. Depending on the time scale of the measurement, different sources contribute to the fluctuations in intensity. Typically contributions from effects such as antibunching, rotational diffusion or triplet-state dynamics will happen at short time scales of microseconds and below [49]. In comparison, the most common source of intensity fluctuations probed in FCS - and the one relevant to this work - is caused by the diffusion of the analyte molecules through the detection volume and happens at timescales that can reach into the millisecond range. In that case the decay of the auto-correlation curve is directly related to the diffusion time $\tau_D = x_0^2/4D$ of the probed

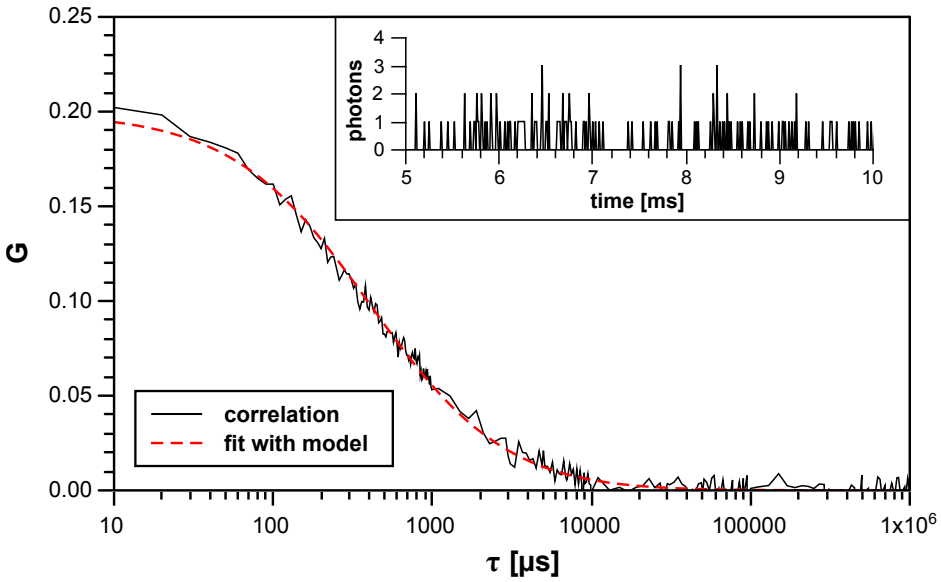

Figure 2.12.: Typical auto-correlation curve (black) from fluorescence measurement of freely diffusing molecules. The red curve is a fit with the standard FCS-model as defined in equation 2.55. The inlet depicts a short section of the original time trace.

analyte molecules. Another noteworthy feature of the calculated auto-correlation is that the amplitude is inversely proportional to the average number of molecules in the detection volume:

$$G(0) = \frac{1}{N} = \frac{1}{CV} = \frac{1}{c_{mol} N_A V \cdot 1000}, \tag{2.54}$$

with the number of molecules N, the volume V, the number concentration C, the molar concentration c_{mol} and the Avogadro constant N_A. To gain quantitative insight into the different parameters of interest, the auto-correlation can be fitted with a model depending on the probed dynamics and the geometry of the detection volume. For typical diffusion-based measurements and using the common approximation of a 3D-Gaussian shape of the detection volume, the resulting function is [46]

$$G(\tau) = \frac{1}{N}\left(1 + \frac{\tau}{\tau_D}\right)^{-1}\left(1 + \frac{1}{S^2}\frac{\tau}{\tau_D}\right)^{-1/2}. \tag{2.55}$$

Here, $S = z_0/x_0$ is the aspect ratio of the detection volume, as determined by its width x_0 and length z_0. The model ultimately depends on the characteristic sizes of the detection volume and the concentration as well as the diffusion constant of the analyte molecules. With knowledge of one pair out of the three parameters the respective third parameter can be determined through FCS. However, determination of those parameters usually requires a precise calibration of the setup. In practice this is not always straight-forward. As outlined in [50], aberrations in cover-slip thickness, refrac-

tive index or astigmatism of the laser beam used for illumination can severely impact the shape of the focus and negatively influence the FCS measurements, leading to relatively large errors in measured diffusion time and concentration in particular. While equation 2.55 is based on the assumption of diffusive transport of analyte molecules, FCS can also be used to probe active flow. Expanding the model to accommodate uniform, one-directional flow [51, 52], one can obtain a new model equation for $G(\tau)$:

$$\begin{aligned} G(\tau) = \frac{1}{N}\left(1+\frac{\tau}{\tau_D}\right)^{-1}\left(1+\frac{1}{S^2}\frac{\tau}{\tau_D}\right)^{-1/2} \cdot \\ \cdot \exp\left(-\left(\frac{\tau}{\tau_f}\right)^2\left(1+\frac{\tau}{\tau_D}\right)^{-1}\left(1+\frac{1}{S^2}\frac{\tau}{\tau_D}\right)^{-1/2}\right). \end{aligned} \tag{2.56}$$

Here the characteristic flow time τ_f has been introduced. The possibility to probe the velocity of fluorescent molecules in flow, coupled with the high resolution of FCS, have led to the adaption of FCS as a velocimetry method in microfluidics [52, 53].

3. Basic Single Molecule Detection

3.1. Motivation

This chapter will briefly address the necessary prerequisites of single molecule experiments and then present an exemplary setup capable of single molecule detection. A simple experiment is shown to establish the basic methods by which experimental data is recorded and analyzed.

3.2. Requirements of Single Molecule Experiments

What are the requirements for successful optical single molecule detection (SMD) in solution? First of all, the probed volume needs to contain one molecule or less on average. To this end, experiments have to be conducted in sufficiently diluted samples, usually below a few hundred pM of analyte molecules. In addition, the detection volume has to be reduced, commonly resulting in femtoliter volumes. Very low analyte concentrations, on the other hand, will result in experiments with very long average molecule arrival time and thus waiting periods between the detection of molecules (see section 2.3.2). Effectively these restrictions limit common single molecule experiments to the range between a few hundred fM and pM concentration of analyte molecules [21]. Lastly, a sufficient signal-to-noise-ratio (SNR) has to be achieved in SMD experiments to ensure efficient identification of single molecule events.

In this thesis, fluorescence-based SMD is investigated. The most common experimental realization for the detection of single molecules by molecular fluorescence is the use of confocal optics. Confocal optics with high-NA microscope objectives combine good photon collection efficiency with small detection volumes and are therefore an obvious choice for single molecule experiments. Due to their good efficiency and response time, in combination with ease-of-use, single-photon counting avalanche photodiodes (SPAD or APD) have found widespread use for the detection of the emitted fluorescence photons. In combination such a setup will result in good a detection efficiency.

The background in a SMD experiment will typically originate from elastic and inelastic scattering of the excitation light, remaining ambient light and the dark-count rate of the detector. Elastic Raleigh scattering of the excitation light can be greatly reduced by efficient filters, while inelastically scattered photons pose greater difficulties, since they exhibit a shift in wavelength that can be comparable to the wavelength shift of the fluorescence signal. Background photons from scattering scale linearly with the intensity of the excitation light and can therefore be reduced by conducting measurements at lower excitation power, at the expense of signal strength. In the case of some

experimental realizations, notably detection schemes based on dielectric waveguides, the contribution of inelastic scattering to the background can be quite substantial, as the source of inelastic scattering is in the waveguide itself. It is therefore beneficial to keep the waveguide small or separate detection and excitation paths. Additional signal noise can arise from the Poisson statistics of photon emission. Lastly for measurements conducted in biological samples, fluorescence signals from impurities can be a major source of unwanted background. In light of the potential future application of the findings in this work, experiments have been conducted with emitters emitting in the near-infrared (Cy7, Dy751, QDot800, see appendix B), since few naturally occurring compounds show emission in the infrared.

3.3. A Simple Single Molecule Detection Experiment

In a very basic single molecule detection experiment depicted in figure 3.1, dye molecules (Cy7, see appendix B for spectra) dissolved in a PBS buffer solution are detected by help of a microscope objective (**O**, NA 0.85, Leica Microsystems, Germany). To this end, the objective lens is focusing through a glass cover slip (Menzel cover glass "# 1.5", thickness 0.17 mm) into a vessel containing the sample with the dye solution (total sample volume ≈1 mL). The objective is illuminated by a collimated laser beam (λ=690 nm) out-coupled from a single-mode fiber to ensure a Gaussian illumination profile on the objective aperture. The choice of the objective has been motivated mainly by two factors. First, the detection efficiency is good enough to ensure reliable SMD and second the working distance of this objective is larger than for common high-NA oil immersion objectives. This will be useful for later experiments. The laser wavelength has been chosen such that it is exciting the dye with good efficiency, while keeping a good spectral separation from the emission wavelength of the dye. Fluorescence light from excited dye molecules in the illuminated focal volume is then collected by the objective, and focused onto an APD (SPCM-AQR-13, Perkin-Elmer) by a lens (L, f=300 achromat, AC254-300-B, Thorlabs) after passing a filter set (**D**, T740/140 650 dcip, Chorma and **F**, Brightline HC 785/62 Semrock) to remove scattered and reflected laser and background light. The total photon detection efficiency η_t for this setup is approximately 12%. Taking into account the total internal reflection of emitted photons at the glass-air interface between sample container and objective lens, the NA 0.85 microscope objective can collect ∼22% of the photons emitted by a dipole with a dipole moment perpendicular to the optical axis [54]. Of these photons ∼55% can be detected, due to the detection efficiency of the APD and losses from mirrors, lenses and filters at the emission wavelength of the dye (λ_{max}=780 nm). During the experiment, the number of photons detected by the APD is counted for discrete time-intervals, or "bins" of length t_{bin}, by a computer, resulting in a time trace containing the counted photon numbers for each time interval of the experiment. As molecules can diffuse freely in the sample volume, the number of molecules in the focal volume will fluctuate, leading to respective fluctuations in the number of detected photons. In absence of any molecules, the number of detected photons will

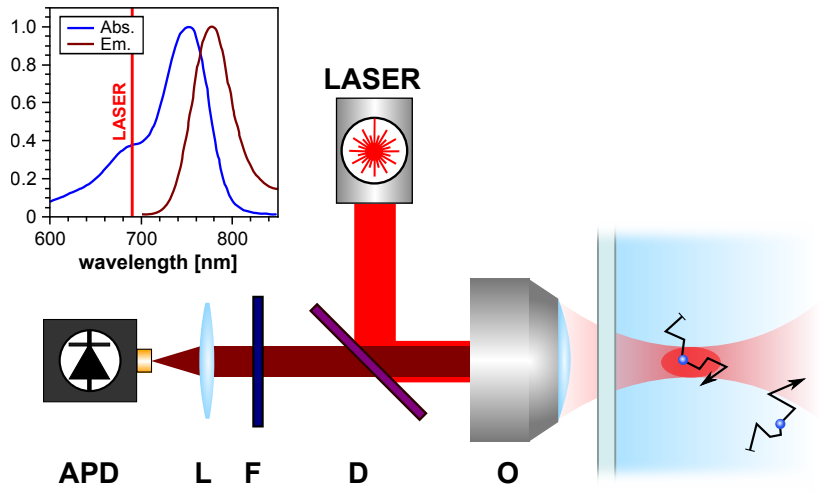

Figure 3.1.: Basic single molecule detection experiment: a laser (λ=690 nm) is focused by a microscope objective (O) into a sample vessel containing organic dye molecules (blue) in solution. During the experiment, the freely diffusing molecules may enter the focal volume (red), leading to their excitation and the subsequent emission of light. The emitted light is collected by the objective, passes a filter set (D, F) and is then focused onto an APD by a lens (L). The inset is showing the dye spectrum and the laser wavelength used for excitation.

default to the background count-rate which is mainly caused by remaining ambient and scattered photons, as well as the dark count-rate of the detector. If a molecule enters the focal volume, it will be excited and subsequently emit fluorescence photons, leading to a sudden increase in the number of detected photons. In figure 3.2a, a 5 s excerpt of a 30 s long time trace from such a simple SMD experiment is shown. In this experiment, the sample contained a 10 pM concentration of Cy7 and t_{bin} was set to 1 ms, i.e. the number of photons detected in 1 ms was counted. Over the course of the experiment, several distinct peaks in the photon count-rate indicate the diffusion of photons into the focal volume. Depending on the residence time in the detection area, the respective local detection efficiency and contributions from photophysical effects such as blinking or bleaching, the height of the peaks (i.e. absolute number of detected photons) will vary. In the next section, the identification of individual molecular fluorescence events will be discussed.

3.4. Evaluation of Experimental Data

The main point of interest in an SMD experiment is the number of counted molecules. In order to identify a signal originating from emission by a molecule, it has to be distinguishable from the background noise. The experiment shown in figure 3.2a has

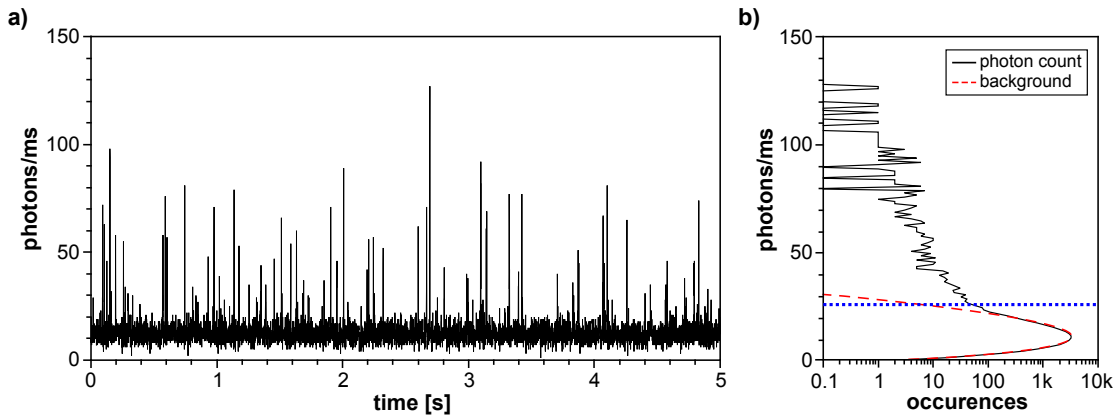

Figure 3.2.: **a)** 5 s long excerpt from a single molecule detection experiment, showing several peaks in photon count rate, originating from freely diffusing molecules in the focal volume. **b)** Histogram of photon counts resulting from the complete 30 s long measurement. The fitted distribution of background photons is printed in red. The blue dotted line indicates the threshold a for the identification of fluorescence events in the experiment.

several distinct peaks originating from fluorescence events. Several peaks , however, are much smaller and hard to distinguish from the background. The number i of photons originating from the background noise will be randomly distributed around a mean value, described by a Poisson distribution:

$$P_p(\lambda, i) = \lambda^i \frac{e^{-\lambda}}{i!}$$

with the expected value and variance λ. Photons originating from fluorescence emission by emitters (e.g. molecules or quantum dots) in the focal volume will lead to an additional contribution to the detected photon numbers. With large enough detection efficiency, this will lead to distinct peaks in the time trace.

For a simple evaluation of the time trace, it is convenient to set a threshold photon number a, above which an event will be counted as a fluorescent event originating from an molecule. In figure 3.2b, the histogram of photon counts detected in the entire 30 s experiment, shown in figure 3.2a, is displayed. The fitted distribution of background events (using a Poissonian distribution) is shown in red. In most experiments, the distribution of background photons and the distribution of fluorescence events will overlap. The extend of this overlap will depend on the mean background count rate and the number of detected fluorescence photons, determined by the detection efficiency of the setup. When deciding on a value for the threshold, potential trade-offs have to be considered. Setting a low threshold will include a larger number of fluorescence events, but increases the probability to erroneously count background fluctuations. Likewise a high background will prevent the inclusion of background events, but also miss a larger number of fluorescence events. Events originating from the background and

erroneously counted as fluorescence events will be referred to as "wrong positives". In figure 3.2b, a threshold (blue dotted line) was chosen such that it intersects the background distribution at a value of 5 occurences, corresponding to a=26 photons, meaning that on average 5 background events may be included as wrong positives. Every event in the histogram above a will be counted as an fluorescence event, resulting in a total number of 633 events for the shown experiment.

This simple analysis of the experimental time trace gives a first estimate of the number of detected molecules during the experiment. It does however also suffer from several limitations. To begin with, it does not consider the possibility of fluorescence bursts that persist for more than one bin in the time trace. If the molecule resides in the focal volume for a timespan longer than t_{bin} and does not switch to a dark-state due to photobleaching or blinking, the experiment will detect fluorescence photons for two or more bins. Consequently, the number of detected fluorescence events is usually not equivalent to the number of detected molecules. Furthermore, the overlap between the two photon distributions in the experimental time trace can make it difficult to correctly estimate the background distribution and set the threshold a. To improve the detection and counting of fluorescence bursts in experimental time traces, an algorithm is used for the evaluation of time traces, which has been developed by W. Grange et al. [55]. In short, the algorithm initially calculates a first estimate of the background distribution, setting a first threshold based on the number of accepted wrong positives and the estimated distribution and then performs a peak detection algorithm. Every identified peak is then counted and removed from the time trace. In a next step, a new estimate of the background distribution and threshold is calculated and the peak detection is repeated. Estimation of background and peak detection are then repeated until all peaks have been identified at the given threshold. This algorithm has proven to reliably detect and count fluorescence events even in the presence of large amounts of noise and is used in this work to determine the number of detected molecules during an experiment.

4. Single Molecule Detection in Flow

4.1. Motivation

In a diffusion-limited single-molecule experiment, the number of analyte molecules arriving in a given detection volume per time will depend strongly on the concentration of molecules and the diffusion constant of the molecules in question. Section 2.3.2 has discussed limitations of diffusion-based transport processes, showing that active transport is needed to ensure viable experimental time-frames for low concentrations of analyte molecules. By creating a directed flow through the detection volume, the sampled volume per time can be increased. This will provide the opportunity to detect a larger number of molecules per time. To illustrate this effect, the time until one molecule is detected under application of a steady flow has been plotted in figure 4.1 for three different concentrations. The calculation assumes experimental conditions as encountered in the experimental setup used in this chapter, resulting in a 3 fL detection volume. For comparison purposes the respective time to encounter one molecule through diffusional transport has been added (dashed lines, calculated with equation 2.48).

On the other hand, the downside of high flow rates is a reduced residence time in the detection volume. This can result in fewer detected photons and decreased signal-to-noise ratio. Too large flow rates can even lead to the inability of resolving single analyte molecules at all, as the number of molecules per bin approaches and eventually exceeds unity. Plotting the number of detected molecules versus the flow rate should thus exhibit a maximum. In fact Horrocks et al. did report a similar behaviour in a recent publication on single molecule detection in microfluidic chips [56], where molecules dissolved in a buffer solution have been pumped into a microfluidic channel by syringe infusion pumps and detected by a microscope objective. It is obvious that flow can be used as an advantage in single-molecule experiments, but will depend on the right set of parameters, most prominently the flow rate. The goal of this chapter is therefore to take a closer look at the underlying mechanisms of single molecule detection in presence of flow and to determine the optimal rate of flow for single molecule detection experiments.

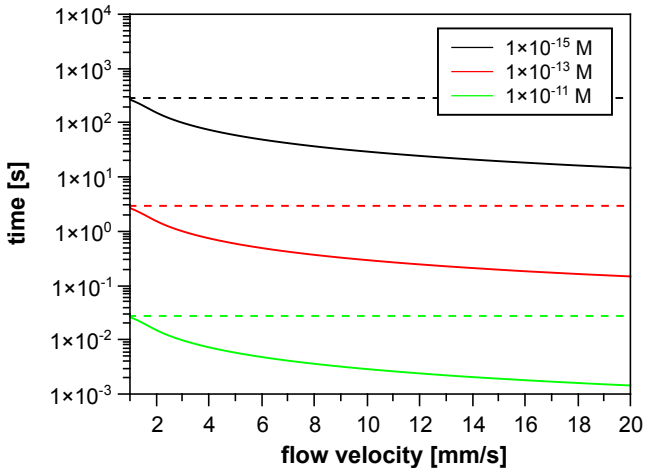

Figure 4.1.: Average time to sample one molecule (focal volume ≈3 fL) for three different molar concentrations. With lowered concentration it is necessary to increase the sampled volume through flow to detect sufficient molecules. For comparison the respective average arrival time by diffusion has been added (dashed lines).

4.2. Analytical Model for Single Molecule Detection in Laminar Flow

4.2.1. Derivation of Model

In this section, an analytic model is derived for the number of detected molecules during a single molecule detection experiment performed in a liquid sample with (constant) flow. The experiment is assumed to consist of B discrete time intervals or "bins" of length t_{bin}, where the number of detected photons is measured for each interval. The total length of the experiment is $B \cdot t_{bin}$. First, the sampled volume during each observed time interval t_{bin} is calculated:

$$V_S = V_0 + A \cdot v \cdot t_{bin} \,,$$

with the focal volume V_0, the cross-section A of the volume perpendicular to the flow and v the velocity of the flow. With increasing flow rate v, the sampled fluid volume passing through the detection volume V_0 per time interval will increase and consequently the average number of molecules that pass the detection volume:

$$N(v) = c \cdot V_S = c \cdot (V_0 + A \cdot v \cdot t_{bin}) \,, \tag{4.1}$$

where c is the number concentration of analyte molecules. With higher concentration and faster flow multi-molecule events, i.e. time intervals that contain the fluorescence photons from more than one molecule due to the presence of multiple molecules in the

sampled volume, are becoming increasingly probable. The probability to encounter i molecules at a given average number $N(v)$ of molecules can be calculated using the Poisson distribution

$$P_P(\lambda, i) = \lambda^i \frac{e^{-\lambda}}{i!},$$

with the expected value and variance λ, which in this case is given by $N(v)$ as obtained through equation (4.1). The resulting probabilities to encounter $i = 0 - 3$ molecules are plotted in figure 4.2 for a range of values of $N(v)$. Therefor, $P_P(N(v), i) \cdot B$ is equivalent to the number of bins in an experiment containing i molecules. The sum over i will again result in B. For typical experimental parameters encountered in this work ($c < 25$ pM, $v < 50$ mm/s), $N(v) < 5$ and thus any event with $i > 15$ can be neglected due to low probability.

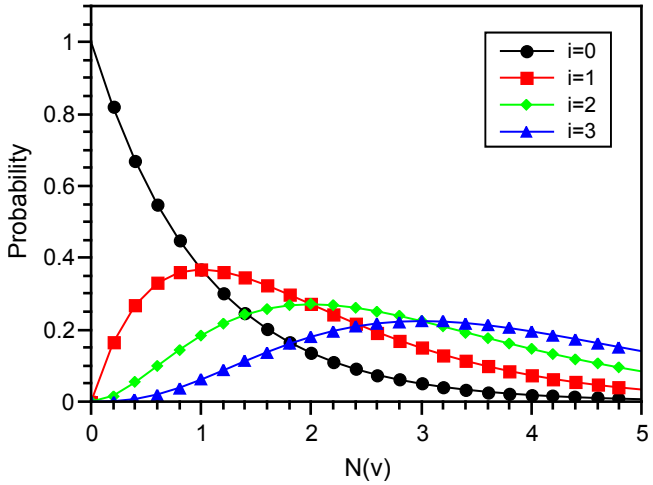

Figure 4.2.: Probability to encounter i molecules for a given average number of molecules in the focal volume $N(v)$. Each curve corresponds to different values of i.

The other important effect of an increasing flow velocity is the decreasing probability to detect a molecule during its passage through V_0, since the reduced residence time will diminish the number of potentially detected fluorescence photons. In absence of any molecules (i.e. $i = 0$), the average rate of photons will correspond to the background count rate $b = b_0 \cdot t_{bin}$, assuming an average rate of b_0 background photons per second. For $i > 0$, the contribution of photons emitted by the molecules has to be included. To estimate this contribution, it is assumed that on average $R_0 \cdot t_{bin}$ photons emitted by a stationary molecule can be detected during t_{bin} by the experiment, where R_0 is the average number of detected photons per second. Including the background count rate b, the combined average number of photons per time interval can then be calculated as

$$R_{total}(i, v) = b + i \cdot R(v)\,. \tag{4.2}$$

Here, $R(v)$ was introduced as the flow-rate dependend number of detected photons during t_{bin}. For a moving molecule, the residence time in the detection volume of width x_0 at the given flow rate will decrease (since $t = x_0/v$) and the average number of detected photons per molecule and time interval t_{bin} is reduced as long as $x_0/v < t_{bin}$. When x_0/v approaches t_{bin}, the number of emitted photons will saturate towards $R_0 \cdot t_{bin}$, which is described phenomenologically as

$$R(v) = \tanh\left(\frac{v}{x_0} \cdot t_{bin}\right) \cdot R_0 \cdot x_0/v\,. \tag{4.3}$$

In a typical single molecule detection experiment, the detection efficiency will vary over the detection volume, usually resembling a gaussian function, as e.g. originating from the intensity distribution in the focus of a microscope objective used to collect molecular fluorescence emission. This can be taken into account in the model by modifying R_{total} with an adjusted gaussian function, simulating the reduced number of detected photons from molecules passing the detection volume in areas of lowered detection efficiency. To this end, the detection volume is divided into concentric shells of equal size with decreasing detection efficiency according to the gaussian function:

$$R_{eff}(i, x, v) = b + i \cdot \exp\left(-\frac{x^2}{2\sigma^2}\right) \cdot R(v)\,. \tag{4.4}$$

Here, x corresponds to the x-th shell of the detection volume and σ is width of the gaussian function. For the purpose of approximating the experimental observations, the detection volume was divided into 10 shells and σ was set to 3.

Knowing the average photon counts, the probability to encounter n photons at a given flow rate v can now be calculated:

$$P(v, n) = \frac{1}{10} \cdot \sum_{x=0}^{9} \sum_{i=0}^{15} P_P(N(v), i) \cdot P_P\left(R_{eff}(i, x, v), n\right)\,,$$

where the result from equation (4.4) was used as the mean of a Poission distribution to calculate the photon emission statistics. Summing over x and dividing by 10 accommodates for zones of differing detection efficiency in the focus and taking the sum over i will consider multi-molecule events. Multiplied with the total number of bins B in the measurement, this corresponds to a function defining the histogram of photon counts in a single molecule detection experiment:

$$H(v, n) = B \cdot \frac{1}{10} \cdot \sum_{x=0}^{9} \sum_{i=0}^{15} P_P(N(v), i) \cdot P_P\left(R_{eff}(i, x, v), n\right)\,. \tag{4.5}$$

The resulting histogram (see figure 4.3a) can now be used to estimate the number of detected fluorescence events at a given flow rate v.

Since the model is assumed to estimate the number of fluorescence events detected

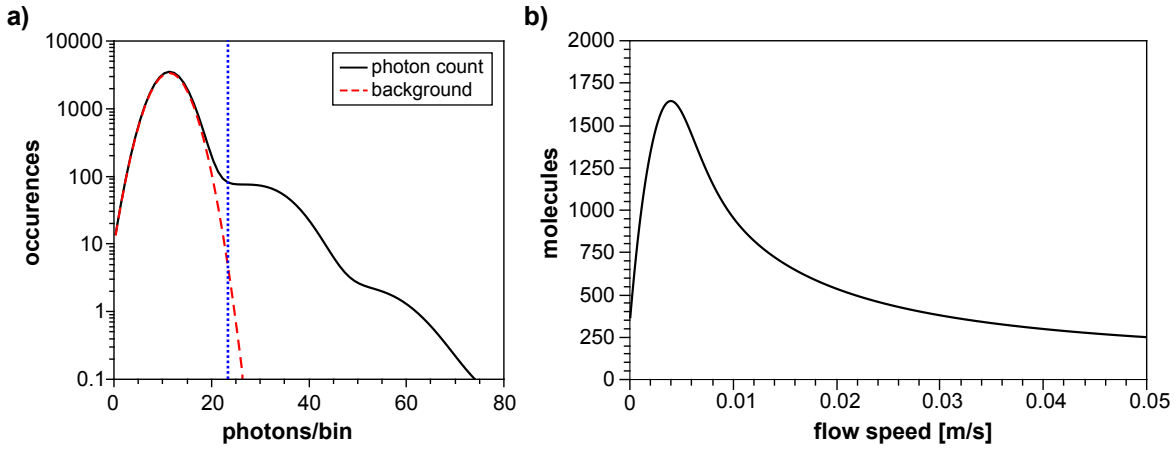

Figure 4.3.: **a)** Histogram of photon counts (black solid line), as calculated by equation (4.5), with the distribution of background photons (red dashed line) and threshold a (blue dotted line, assuming 5 wrong positives) for counting of fluorescence events. **b)** Approximate number of molecules detected in an experiment, obtained by counting the number of fluorescence events above the threshold in a) at the respective flow speed.

during an SMD experiment, the results obtained from the model are treated similarly to experimental data, as described in section 3.4. By summing up $H(v,n)$ over n from a lower threshold a, determined by the amount of accepted "wrong positives", to infinity the number of detectable events containing photons from molecular emission can be calculated. For a simple approximation of the threshold, it is sufficient to find the (upper) value of n for which the distribution of background photons assumes a:

$$a = B \cdot P_P(b,n) \tag{4.6}$$

The second Poisson distribution in equation (4.5) can be approximated by a normal distribution. Integrating the resulting new equation for $H(v,n)$ up to an upper limit where the probability to detect that number of photons has decayed sufficiently (e.g. 500), the integral over $H(v,n)$ can be evaluated using the error function, arriving at

$$\int_a^{500} H(v,n) \cdot dn = \\ = B \cdot \frac{1}{10} \cdot \sum_{x=0}^{9} \sum_{i=0}^{15} P_P(N(v),i) \frac{1}{2} \left(\operatorname{erf}\left(\frac{500 - R_{eff}}{\sqrt{2 \cdot R_{eff}}} \right) - \operatorname{erf}\left(\frac{a - R_{eff}}{\sqrt{2 \cdot R_{eff}}} \right) \right) . \tag{4.7}$$

This variant is better suited for use in fitting algorithms and was mainly used in this thesis. Evaluating equation (4.7) with common parameters for focal volume, R, etc. leads to the typical curves as depicted in figure 4.3b. For the purpose of fitting

experimental data, the velocity v in equation 4.7 is substituted by

$$v_{fit} = c_v \cdot s \,, \tag{4.8}$$

where c_v is a fitting parameter and s the stirring rate applied to the rotor. The fitting parameter thus acts as a scaling constant between stirring rate and flow velocity.

4.2.2. Scope and Limitations

The model presented in the previous section describes the behavior of SMD experiments in flow based on several experimental parameters, notably size of focal volume, time resolution and emission characteristics of the emitters considered. By adjusting these parameters, some accommodations can be made for different detection schemes (e.g. waveguides with larger detection volume) and emitters (different dyes or emitter types like quantum dots).

There are limitations to the model that should be considered, however. The model contains assumptions about the mentioned parameters, which need to be known with some confidence to ensure reliable predictions. In particular the determination of size and shape of the detection volume of an SMD experiment is often difficult (cf. section 4.4) and a major potential source of error. Still, in comparison to methods such as FCS, this model only requires a reasonably good approximation of the total volume and area perpendicular to the flow, as opposed to knowledge of the exact shape of the volume [57].

The next issue concerns the determination of "detected" molecules in the model. As outlined in section 3.4 and by Grange et al. in [55], an accurate determination of the detection threshold a in SMD experiments is a non-trivial task. Notably the distributions of background photons and fluorescence emission usually overlap, which entails a certain amount of "undetected" fluorescence events or erroneously detected background events in experimental data. During the calculation of detected fluorescence events, performed by integrating equation (4.7), the threshold is determined as a fixed value by calculating the corresponding photon number for which the distribution of background photons will assume a. It does therefore not consider that the relative amount of bins originating from either background or fluorescence photons is changing with flow rate, since the probability to encounter i molecules is dictated by equation (4.1). Nevertheless this approach offers an acceptable approximation of the results from analyzing experimental data for a wide range of flow rates and concentrations. Due to high probability of multi-molecule events and short residence time, the overlap between background and fluorescence distributions will increase for high flow rates, eventually resulting in histograms where background and fluorescence distributions cannot be separated effectively anymore. This will result in a reduction of detected fluorescence events, which is however even more pronounced in experiments, since the fixed threshold used in the model will lead to the inclusion of events that would not be considered in comparable experiments.

At low flow rates, on the other hand, deviations are expected from experimental

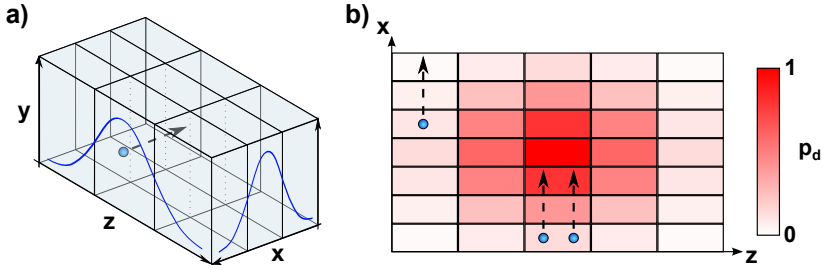

Figure 4.4.: Principle of the Monte Carlo simulations. **a)** The simulation volume, corresponding to the detection volume, is represented by an $x \times z$ 2D-array. Each cell has a detection probability modeled after a 2D-gaussian. Molecules (blue) are moving through the volume in x-direction. **b)** A representation of the resulting array with discrete, color-coded detection probabilities $p_d(x, z)$, containing randomly distributed molecules. Molecules "enter" the simulation array at the lowest row and transverse it in x-direction. At each time-step, if a molecule is occupying any cell (x, z), a photon can be emitted, with the detection weighted by $p_d(x, z)$.

data, since the contribution from diffusional transport is not included. As the relative importance of diffusional import is decreasing with increasing flow rate, the effect can be neglected for fast flow and is assumed to be small in the range of flow rates of interest.

Finally, the proposed model is based on steady laminar flow. Under certain conditions that can be encountered in experiments with high flow rates and high Reynolds numbers, turbulent flow can occur. The chaotic and instable nature of turbulent flow cannot be covered by the model and therefore no reliable predictions can be made.

4.3. Monte Carlo Simulations

4.3.1. Method

In order to crosscheck the assumed experimental conditions and the analytic model presented in section 4.2, a program has been written that uses a Monte-Carlo approach to simulate SMD experiments under conditions of laminar flow. Aside from the flow rate determining the velocity at which molecules pass through the simulation volume, the simulation considers the emission rate R_s of photons by the molecules, the detection efficiency p_d at different positions in the focus (see figure 4.4), the bleaching rate p_{bl} of the molecules and the rate of background photons b_s. The following part explains the working principle of the simulation:

1. In the first step, a 2D array V_{sim} is created that serves as a representation of the detection volume. Each cell (x, z) in the detection volume is associated with a certain probability $p_d(x, z)$ to detect a photon emitted by molecules in that cell, modeled after a 2D Gauss function (see figure 4.4).

2. Assuming that the "flow" in the simulation is progressing parallel to the rows of the array, each cell of the first column is filled at random with i molecules according to the probability to encounter a certain number of molecules at the given concentration (i.e. $P_P(V_{cell} \cdot c, i)$, where P_P is the Poisson distribution, and $V_{cell} \cdot c$ the average number of molecules per cell volume at concentration c.

3. The molecules are moved in time-steps of $t_{sim} = 10^{-7}$ s in direction of the flow through the simulated detection volume. The step width is thus determined by the speed at which the molecules are moved, i.e. the simulated flow rate.[1]. Given a spatial resolution of 100 nm, the maximum speed that can be simulated is thus 1 m/s. This enables the simulation of a wide range of flow speed without sacrificing too much computation time.

4. After each time step, the detection subroutine checks if a molecule is present in any position (x, z). Each molecule in the detection volume can then "emit" a photon with a probability according to the preset emission rate $R_s = R_0 \cdot t_{sim}$, modified by the detection efficiency at the position in the focus. If a generated random number is lower or equal to the calculated probabilities, the photon is assumed to be detected and added to a buffer counter. To account for (random) noise, e.g. from stray light or the detector's dark count rate, an additional photon may be added to the buffer, determined by $b_s = b_0 \cdot t_{sim}$. Similarly p_{bl} determines if a molecule bleaches at this point, which will lead to its removal from the simulation.

5. If the number of steps exceed the width of a cell, as determined by size of the detection volume and the number of cells in the array, the molecules "jump" to the next cell and the first row of the array is filled with new molecules by the randomized routine as described earlier.

6. The "movement" and "detection" steps are now repeated until the simulation time exceeds the binning time t_{bin} of the experiment, at which point a read-out of the buffer is performed. This value is then stored as the detected number of photons in an output array representing the experimental time trace.

7. The simulation time is reset and the buffer emptied. The simulation will continue until a predefined maximum simulation time is reached.

8. Upon completion of the simulation, the output array is written to disk and can be analyzed further.

A listing of the main components of the simulation program can be found in appendix D.

[1] t_{sim} is the internal time resolution of the simulation. Each "bin" of length t_{bin} will contain S steps of length t_{sim}, where $S = t_{bin}/t_{sim}$

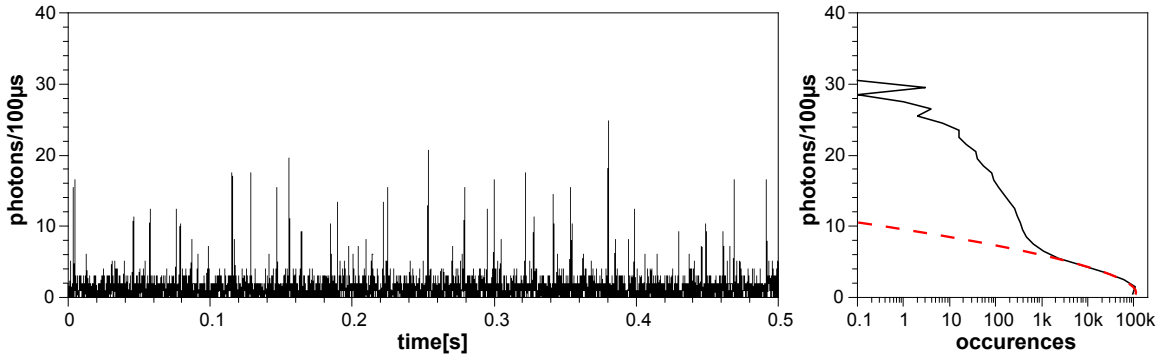

Figure 4.5.: 0.5 s long part of a time trace created by the Monte-Carlo simulation at a sample concentration of 20 pM (left). On the right side, the histogram of the entire, 30 s long time trace is shown, with an approximation of the contribution by the background photons (red).

4.3.2. Simulation Results

The Monte-Carlo simulation has been used to create time traces at various flow speeds, which have subsequently been analyzed by the same methods as the experimental data. The probabilities to detect a fluorescence photon, a background photon and for the bleaching of a molecule have been chosen such that the resulting time traces match with experimental results. The resulting values for the internal time interval of $t_{sim} = 1 \times 10^{-8}$ s have been determined to be $R_s = 3.6 \times 10^{-4}$, $b_s = 1.1 \times 10^{-4}$ and $p_{bl} = 1.3 \times 10^{-5}$. A short excerpt of a 30 s trace generated by a simulation of a 20 pM sample is depicted in figure 4.5, together with the histogram of the entire trace. Both trace and histogram closely resemble experimental results.

The results obtained by analyzing the simulated time traces at flow rates between 0.05 and 50 mm/s with the peak detection algorithm (cf. [55]) show a behavior very similar to what can be observed in the experiments and simulations (4.6). After an initial fast increase of detected molecules, a maximum is reached at 5 mm/s and the number is subsequently declining. Further analysis of the simulated traces by a FCS-in-flow model shows an average residence or flow time τ_F that is inversely proportional to the flow speed of the respective simulation, as expected for the simple laminar flow in the simulation. Deviations in shape and absolute position of the maximum of detected molecules in respect to experiments or analytical model can be attributed to differences to the simulated conditions. Most notably the simulation is containing only a rough approximation of the detection volume (cf. section 4.4), affecting the absolute number of detected molecules, as well as the behavior at different velocities. As will be discussed later, the concept of a laminar, linearly increasing flow is also not entirely correct under all encountered experimental conditions.

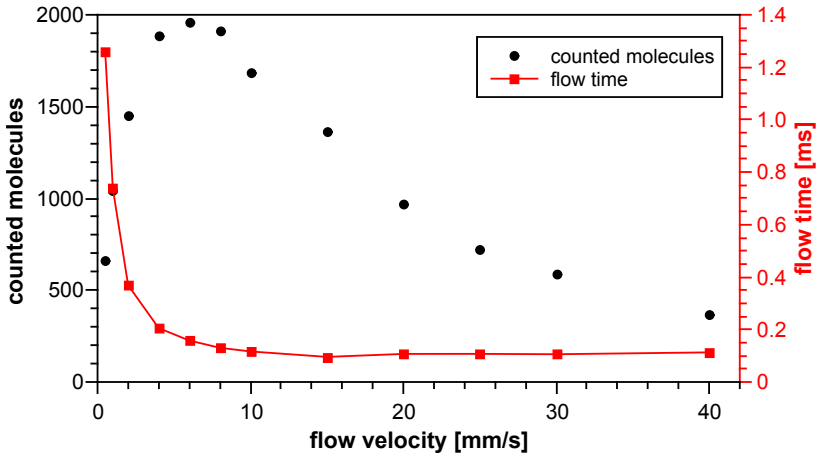

Figure 4.6.: Resulting number of detected molecules (black circles, left axis) and measured flow time τ_F (red squares, right axis) by performing Monte-Carlo simulations at different flow speeds ranging from 0.5 up to 40 mm/s. The characteristic behavior observed in experiments and analytic model is reproduced by the simulations.

4.4. Flow Measurements

4.4.1. Experimental Setup

For the single molecule detection experiments in flow, a microscope objective (NA 0.85, Leica) is used. The basic setup resembles figure 3.1 from chapter 3.3, a detailed depiction of the setup can be found in appendix A.

The microscope objective is mounted on a 3-axis fiber launch system (MBT610/M, Thorlabs) and is focusing through a glass cover slip (Menzel no 1.5, 170 µm) at varying distances inside a sample vessel containing Cy7 dye in a PBS buffer solution. The microscope objective is illuminated by a collimated laser beam (λ=690 nm) outcoupled from a single-mode fiber to ensure a Gaussian beam profile. The beam size is adjusted by an aperture to illuminate half of the back-aperture of the microscope objective. The reduction in illuminated aperture leads to an enlarging of the point spread function (PSF), but ensures fewer deformations when focusing at different distances from the surface, an effect which will be examined more closely in the next section. For the purpose of defining the distance between surface and focus, the position of the focus is defined by its center (as given by the maximum of a gaussian fitted to the objective's PSF obtained according to [58]). By moving the microscope objective closer towards the cover glass, we can move the focus deeper into the sample. Fluorescence light from dye molecules in the illuminated focal volume is then collected by the objective, and focused onto an APD (SPCM-AQR-13, Perkin-Elmer) by a lens (f=300 mm, AC254-300-B, Thorlabs) after passing a filter set to remove scattered and reflected laser and background light. The flow rate in the sample again can be adjusted

by use of a small rotor driven by an electric motor to stirring rates between 500 and 30000 rpm. A microscope objective will limit the experimentally accessible region to a thin zone above the surface of the sample vessel, where surface effects influencing local flow rate in the sample are strong. The fluid molecules at the solid-fluid interface are assumed to be immobile respective to the surface. This is the well-known no-slip condition from fluid mechanics. With increasing distance, the influence exerted on the fluid particles by surface friction decreases, and fluid molecules will be able to move faster. In effect this is resulting in lowered local flow rates at a given global flow (as induced by the rotor) in the regions close to the surface.

During the experiment, a time trace of the detected number of photons per bin is recorded. The obtained trace for each velocity and position is then analysed (cf. section 3.4) to count the number of individual fluorescence bursts during the experiment.

4.4.2. Illumination and Detection

As a simple rule-of-thumb, the width of a focus produced by a high-NA microscope objective can be estimated to be about half the illumination wavelength. Obtaining a more precise knowledge of shape and size of the focus is important for the purpose of calculating the number of expected single molecule events as outlined in section 4.2. To this end, the illumination point spread function of the objective is calculated. In case of SMD experiments with the setup described in the previous section, the objective is focusing through a layered sequence of dielectric media with different refractive index (RI) n_i, with n_1 denoting the RI of the medium between objective and cover slip, n_2 the RI of the cover slip of thickness d and n_3 the RI of the sample. Every microscope objective will be designed according to a certain set of values for refractive indices, cover slip thickness and focal position. In this "design case", the focus will typically show minimal aberrations and best confinement. However, deviations from those design values will cause the focus of the objective to develop deviations in shape and position, including deformations and fringes. Notably moving the focus from the surface deeper into the sample volume can quickly degrade the qualtiy of the focus. Typically such deviations are more pronounced on high-NA objectives.

Using the method and computational implementation from [58], the PSF of an arbitrary objective can be calculated. In fig. 4.7 a-c, the PSF has been calculated for three positions of the NA=0.85 air objective used in the experiments in this work. By changing the displacement of the microscope objective towards the cover slip, we can move the position of the focus inside the sample space. With increasing displacement, the PSF will however exhibit increasingly strong deformations and fringes. When the focus is corresponding with the cover-sample interface ("design case", fig. 4.7 a, displacement d=0 µm), the focus is symmetric and well-defined. Increasingly pronounced side-lobes and fringes are appearing for d=10 µm (fig. 4.7 b) and d=20 µm (fig. 4.7 c). Due to the higher refractive index in the sample space (assumed to be n_3=1.33) the displacement of the PSF is larger by a constant factor of 1.4 than the corresponding objective displacement. The cover-sample interface in figure 4.7 is always located at -d.

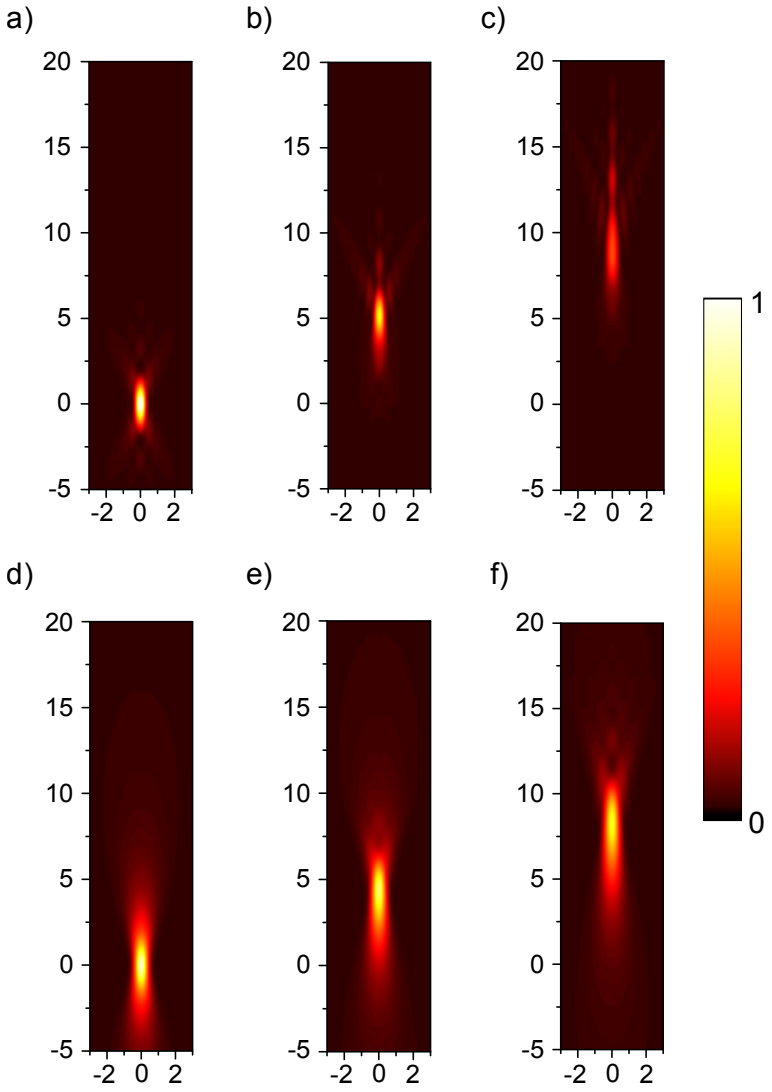

Figure 4.7.: PSF of an NA=0.85 microscope objective calculated according to [58]. **a** to **c**: design case (cover slip thickness d^*=170 µm, and cover slip RI of n_2^*=1.515, with increasing displacement d of the objective (a: 0 µm, b: 10 µm, c: 20 µm).**d** to **f**: Resulting PSF by underfilling the back-aperture of the objective (β=2). The PSF is noticeably larger than in the case of $\beta \leq 1$, but less prone to deformations for increasing displacement of the objective (d: 0 µm, e: 10 µm, f: 20 µm).

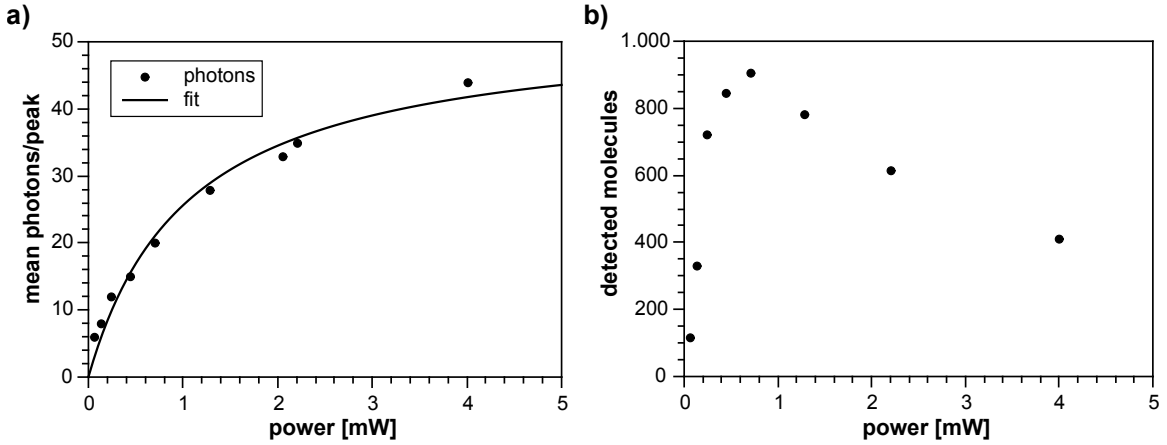

Figure 4.8.: **a)** Saturation of fluorescence emission as a function of excitation power for the NA=0.85 objective with filling factor β_G=2. The fit with equation 2.1 results in I_S=1.06 mW and R_I=52.8 photons/ms. **b)** Detected molecules at the respective excitation power. The detection efficiency is showing an optimum around 0.75 mW for this setup.

Since this deformations to the PSF at increasing displacement make a direct comparison of SMD experiments conducted at different focus positions difficult, it is beneficial to reduce deformations as far as possible. This can be achieved by reducing the illuminated fraction of the objective back aperture (so-called underfilling), which effectively lowers the NA of the objective in respect to the illumination. The illuminated fraction is described by the filling parameter $\beta_G = r_a/r_i$, defined as the ratio of the objective aperture radius to the illuminating beam waist radius. Thus, a larger value for β_G is equivalent to a reduction of illumination beam waist. The effect of increasing β_G to a value of 2 has been calculated and shown in figure 4.7. While pictures **a** to **c** depict the results for the design case, assuming a setup perfectly matched to the parameters the objective has been optimized for and with β_G=0 (uniformly flat illumination of the objective aperture), **d** to **f** are the resulting PSFs for β_G=2 at the same values for objective displacement. In this second sequence it is obvious that increasing β_G leads to an increase in width and length of the PSF. At the same time, however, the focus better retains a gaussian shape and deformations are less pronounced.

While the increased extension of the PSF is a trade-off for experiments relying on a smaller focal volume, the advantages are obvious when doing experiments at multiple and especially larger distances from the cover-sample interface.

With the increase in size of the PSF, the resulting lowered power density in the illuminated area necessitates an increased excitation power for efficient SMD (cf. section 2.1). A measurement was performed to estimate the saturation behavior of dye molecules when illuminated by this setup. Figure 4.8a is showing the average peak height[2] in dependence of the power entering the objective. The data points have then

[2]As determined by estimating the distribution of background and fluorescence photons and calculating the arithmetic mean of the fluorescence-peak height distribution.

been fitted with equation (2.1), which yielded I_S=1.06 mW and R_S=52.8 photons/ms. The first value may appear large for objective-based setups, but is a direct result of the large illuminated volume. The increase in fluorescence emission with increased excitation power is accompanied by an linear increase in the number of background photons, resulting in an decreasing signal-to-noise ratio. Looking at the number of detected molecules (figure 4.8b) in this set of measurements, a maximum is reached around 0.75 mW. Consequently an excitation power of 0.8 mW has been chosen for the experiments in this chapter. As an additional welcome side-effect, bleaching and blinking of dye molecules is reduced at lower power.

4.4.3. Results and Discussion

Surface flow In a first experiment, the the number of detected molecules as a function of flow is measured. The experiments are conducted with the setup from section 4.4.1. To this end, the focus of the objective lens is moved to a fixed position 6 µm above the surface of the glass cover slip of the sample vessel. A series of 30 s long time traces is recorded and analyzed with the burst-detection algorithm. Each subsequent measurement is conducted at a fixed speed, for a total range from 0 (diffusion only) to 14000 rpm. The number of detected molecules at each stirring rate is shown in figure 4.9. After switching the rotor on, with increasing flow and consequently influx of molecules, a fast increase of detected molecules is observed, resulting in a distinct maximum around 2000 rpm. Subsequently the number of detected molecules starts to decline again, as lowered residence time and increasing overlap between adjacent fluorescence bursts decreases the probability to detect a molecule. The results strongly resemble the shape seen both in the results from the analytic model derived in section 4.2 and the Monte-Carlo simulations. Fitting the data with the model based on equation (4.7) yields a fitting constant $c_v = (1.7 \pm 0.1) \times 10^{-6}$ m/s · rpm, for a flow velocity of 3.4 mm/s at the maximum count rate.

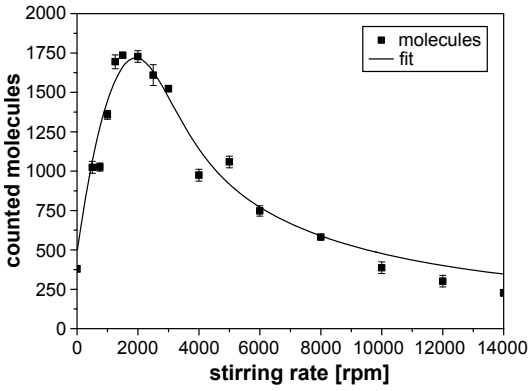

Figure 4.9.: Number of detected molecules (squares) in a SMD experiment as a function of stirring rate at a fixed position 6 µm above the surface. The number of molecules is going through a clear maximum around 2000 rpm. The solid line is the resulting fit with the model based on equation (4.7).

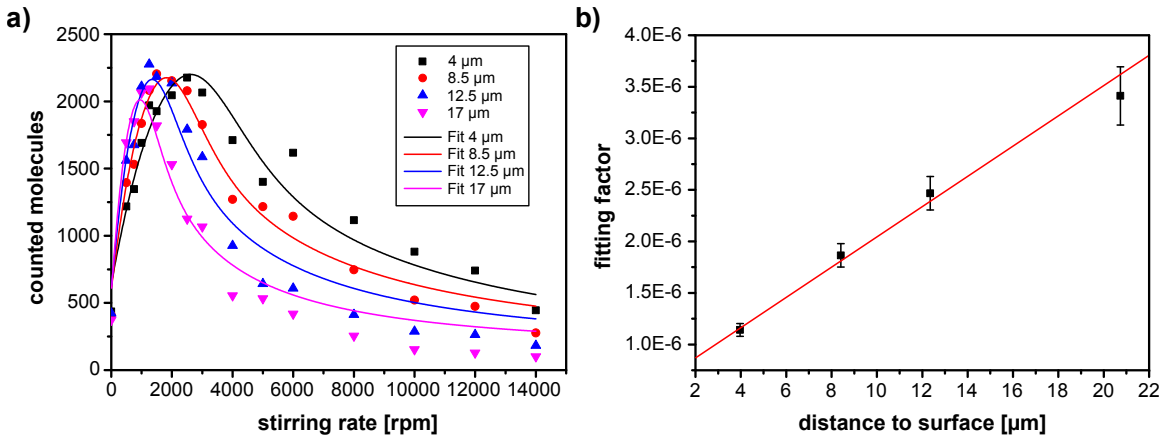

Figure 4.10.: **a)** Experimental data from single molecule experiments at different distances from the surface. The solid lines are the resulting fits using a custom fitting function based on equation (4.7). **b)** Fitting constant c_v for objective displacement values ranging for 3 µm to 15 µm. With increasing distance, the increase in c_v corresponds with an increased local flow velocity.

Since the position of the focus inside the sample volume can be adjusted by moving the objective perpendicular to the cover glass, a vertical flow profile can be recorded. The flow profile of the surface flow is shown in figure 4.10. At each position, again the number of molecules per 30 s have been recorded for stirring rates ranging from 0 to 14000 rpm. The measurements resemble the familiar behavior shown earlier, but with increasing distance from the surface the maximum of each curve in figure 4.10a is shifted towards lower stirring rates. This is in agreement with the assumption of a vertical velocity gradient in the sample fluid above the cover glass (compare section 2.3.3). Each set is then fitted with the model described by equation 4.7. The resulting fits are represented by the solid lines in figure 4.10a. To compensate the increased size and distortion of the focus for large displacement into the sample, the PSFs for the respective displacement have been calculated (cf. section 4.4.2) and then fitted with Gaussians to estimate their size at different displacement values. The obtained values are used in the fitting model to correct the effect of the displacement. From the fit with the flow model, a scaling constant c_v is obtained for each position, which links the stirring rate of the rotor with the local flow velocity as defined in equation (4.8). The resulting values for c_v are shown in figure 4.10b. With larger distance from the surface c_v is increasing linearly, corresponding to a faster local flow at a given stirring rate, which is in line with expectations. Through the fitting constants the local velocity during the experiments in figure 4.10a can be calculated. The maximum of each curve is found to be at a flow velocity around 3 mm/s, with a small shift towards higher velocity with increasing distance. The drift can be explained by the influence of the changing PSF, which also influences the position of the maximum. In comparison the maximum was found to be located at a velocity of ≈6 mm/s in the Monte-Carlo

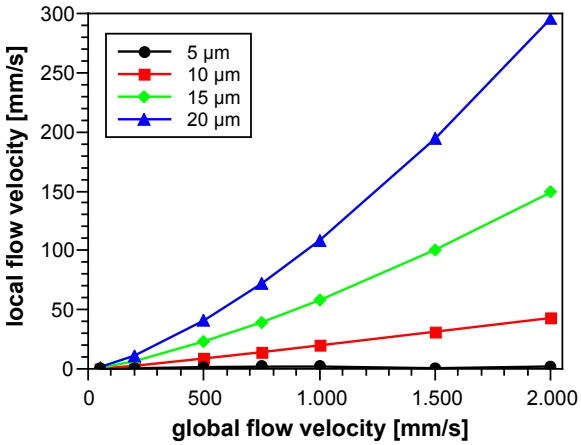

Figure 4.11.: Local flow rate for varying global flow rates at different vertical positions (in µm) over a flat surface. The relation is not linear, but rather of a higher order.

simulations (section 4.3), which is notably larger, but likely caused by differences between the actual experimental parameters and the approximated representation in the simulation.

However, due to several reasons, the fitting error associated with c_v is growing with increasing distance. First, with increasing distance from the surface, the local flow velocity corresponding to a given stirring rate is increasing (see section 2.3.3. Due to technical limitations, the lowest possible stirring rate of the motor used for stirring is 500 rpm. At larger surface-focus distances it becomes therefore difficult to experimentally resolve the maximum of the molecule count rate within the accessible range of stirring rate. Second, the analytic model derived in this thesis assumes a linear relation between local and global flow rate. This is correct according to the boundary layer theory of fluid mechanics, but simulations (cf. figure 4.11) show that the correlation between the two can deviate from a purely linear relation especially at large surface-focus distances and higher flow rates. The result is a difference between the "true" local flow velocity and the flow velocity assumed by the model. Third, as described in section 4.2.2, the calculation is expected to overestimate the number of detected molecules compared to experimental data for high flow rates due to the way the detection threshold is determined. As a consequence of the last two points, the number of experimentally detected molecules can deviate considerably from the calculated results at high stirring rates. This is especially visible in figures 4.10 and 4.13, where the fits for large displacements of the objective deviate visibly from the experimental results at high stirring rates. Lastly, the focal length perpendicular to the flow is relatively large ($\sim$ 6-8 µm) for the chosen illumination conditions and each experiment is measuring the average flow rate in the elongated focal volume. In this context it should be noted that the elongation of the PSF will become more pronounced at large displacement - despite lowered illuminated aperture. For experiments that

require a high spatial resolution, a smaller illuminated volume is desirable and can be achieved by illuminating the entire aperture of the objective. This will, however, come at the price of stronger deformations of the focus that need to be corrected in the model.

Flow at an artificial step Having established the behavior of SMD measurements in laminar flow, the presented model can be used to probe flow, e.g. for use in velocimetry. For this purpose, an micrometer-sized artificial step has been manufactured on top of the cover-glass on the sample container. An artificial step can be used to create a small vortex in its wake that could potentially trap molecules to enhance detection efficiency. CFD (computational fluid dynamics) simulations performed with the Flow Simulation plugin of Solidworks (Solidworks 2009, Dassault Systemes) on a 3D model of the steps confirm the formation of a low-velocity vortex at the step. Figure 4.12a depicts the resulting flow lines and local flow velocity for a global flow velocity of 0.5 m/s parallel to the surface. Furthermore grid-like structures formed from series of steps or grooves are exploited in microfluidics as mixing-devices, since they facilitate the creation of vortices that can disturb the otherwise laminar flow encountered in microfluidic devices. The step has been created by spin-coating the cover glass between sample volume and objective with UV-glue, which is then exposed to UV-light through a mask containing an $\approx$ 1 mm wide slit. After removal of unexposed glue, a step with a height of $\approx$ 12 µm remains. The detailed protocol for the creation of steps is described in appendix A.2. Figure 4.12b has a SEM-image of a cut through one of the steps, showing the profile, as well as a schematic drawing.

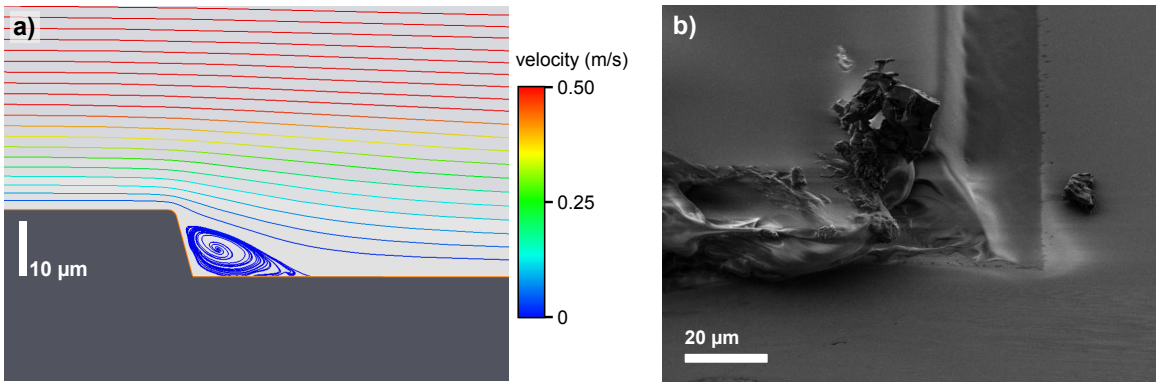

Figure 4.12.: Artificial steps for flow manipulation. **a)** Flow lines around a 12 µm high step. The flow lines are color-coded to the local velocity at the position. A small vortex is forming directly behind the step and the velocity is greatly reduced. **b)** SEM image of a cut through one of the steps fabricated for this work, showing the profile of the step.

Comparing the number of recorded molecules and the respective values of c_v to the earlier experiment, two major effects can be observed. The main influence of the step is a lowered flow rate compared to the undisturbed flow. Consequently,

the maximum of molecule counts is shifted to higher stirring rates. However, once the vertical displacement of the focus is in the range of the step's height (>12 µm, equivalent to $\gtrapprox$ 9 µm objective displacement), a sudden increase in local flow velocity occurs. This behavior is mirrored in the resulting values of c_v (cf. fig. 4.13b. Here a deviation from the slope of the first 3 data points appears at 17 µm above the surface. This points to an area of reduced flow rate directly behind the step.

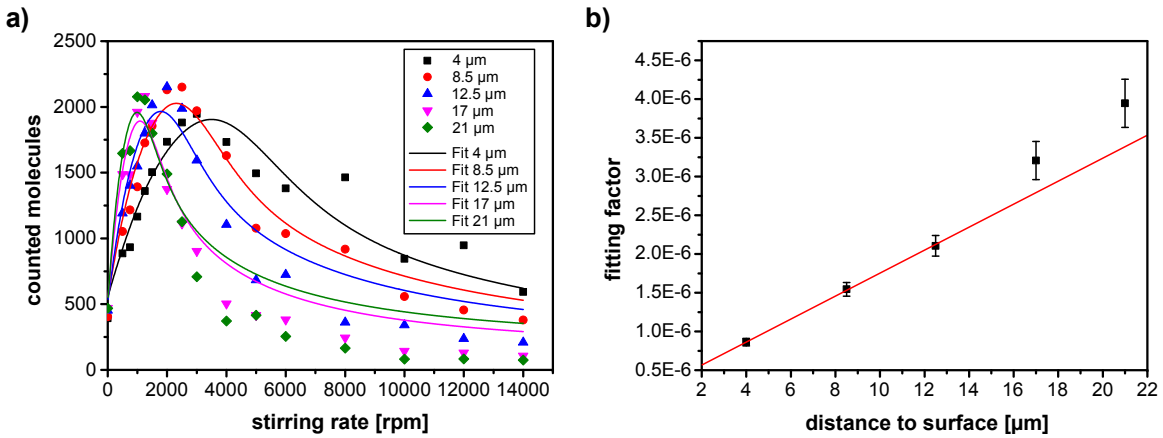

Figure 4.13.: **a)** Measured number of counted molecules 2 µm behind the step at different vertical distances. For an objective displacement greater than 9 µm, the objective is focusing above the step and the increase in local flow velocity is resulting in a sudden shift of the maximal count rate towards lower stirring rates. **b)** Fitting constant c_v for different objective displacement values corresponding to the measurement in a). At 17 µm we see a sudden jump in c_v, caused by the increase of local flow rate above the step.

To cross-check the results from this model with established FCS models, the recorded time traces have been analyzed with a flow-based FCS model as defined by equation (2.56). In figure 4.14a the characteristic flow time τ_F, as determined by fitting the auto-correlated raw experimental data with equation 2.56, is plotted for four sets of data recorded above a flat surface and at an objective displacement ranging from 3 to 15 µm. Since the residence time of molecules in the focus is given by $t = x_0/v$ for steady laminar flow, the flow time τ_F is expected to behave as $1/v$, which is indeed observed. As the stirring rates approach $\approx$ 6000 rpm, the calculated value for τ_F asymptotically approaches 0.1 ms, which is the time resolution used in the experiments. Fitting autocorrelation curves with $\tau_F < 0.1$ms would require to record the experimental time traces at a higher time resolution. For those values above 6000 rpm stirring rate, calculating the flow velocity (assuming an effective 0.9 µm diameter of the focus) yields comparable values to the results from the analytical model. On average the flow velocity obtained from the FCS analysis is higher by a factor of 1.3, which is in good agreement, considering that both approaches are subject to certain limitations. Most prominently the size (and shape) of the focal volume can only by

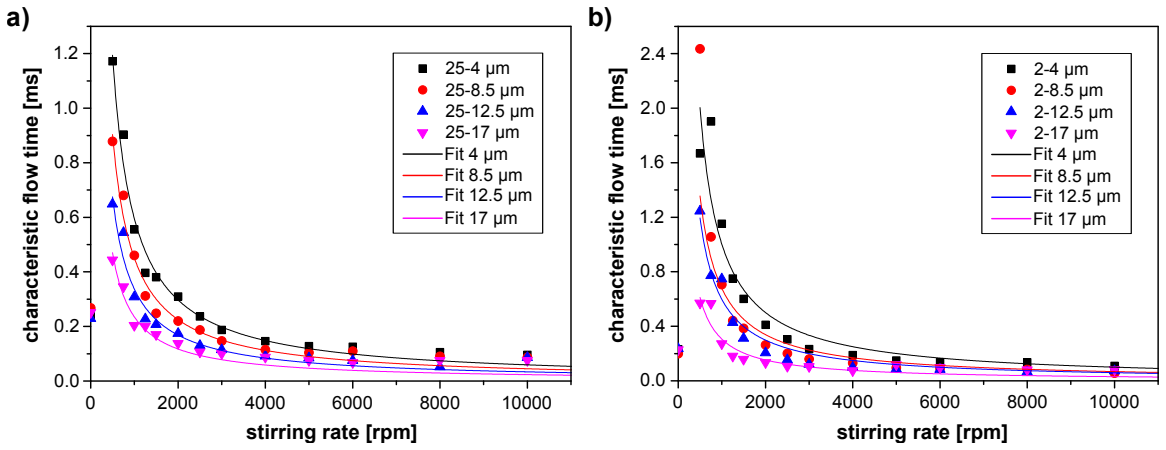

Figure 4.14.: Resulting characteristic flow time τ_F from autocorrelated experimental data at different vertical distance, fitted with equation 2.56 (symbols). The resulting values of τ_F for different stirring rates have been overlayed with a simple reciprocal function of the type $y = 1/(b \cdot x)$. **a)** depicts the results for the flat surface. The flow time is behaving as $1/s$ with increasing stirring rate s. **b)** depicts the results at 2 µm behind the step. Here, in addition to a generally reduced flow time, the influence of the step is causing a deviation of the simple $1/s$ behavior seen in a).

approximated to some degree. This is especially important for FCS measurements, which rely on a good agreement between the underlying model and experimental parameters [57, 50]. Similarly this also affects the quality of the fits performed with the analytical model from section 4.2.

In figure 4.14b, the same analysis has been performed for the experiments 2 µm behind the step. On top of a visibly increased flow time, the data in figure 4.14a now cannot be explained with a simple reciprocal function proportional to $1/v$. The modified flow behind the step is resulting in a non-linear relation between global flow rates (stirring rate) and local flow rate behind the step.

4.5. Conclusions

SMD experiments in flow are showing a characteristic behaviour with a distinct maximum in the detection rate at a certain flow rate. A model to estimate the number of detected fluorescence events in SMD experiments under conditions of flow has been developed which could reproduce the experimental findings. Additional Monte-Carlo simulations have further confirmed the behavior. Based on the model, an optimized flow rate can be applied in a SMD experiment to maximize the detection efficiency of the setup, which is expected to be particularly beneficial in low-concentration measurements and microfluidic devices. In addition the flow profile of a laminar flow over a flat surface was probed by moving the focus to different distances from the surface

and detecting the number of fluorescence events. After fitting the data with the model, a velocity profile could be obtained. The results from the flat surface where compared to experiments at a step-like structure, which showed the influence on the flow by the step. When used in a calibrated setup with sufficient knowledge of the shape and size of the detection volume, as well as the emission properties of the dye, the model presented in this work can therefore be used as a velocimetry method to determine the local flow rate e.g. in microfluidic systems. In comparison with other techniques, only a relatively simple setup is required and less emphasis is put on the precise knowledge of certain parameters. While the spatial resolution in the experiments in this work is so far lower than e.g. in common FCS-velocimetry experiments, it can easily be brought up to the same resolution by increasing the illuminated aperture of the objective and improved confocality - at the cost of stronger susceptibility of size and shape of the PSF to displacement of the objective.

5. Single Molecule Detection by Waveguides

5.1. Motivation

To realize a fully integrated single-emitter detection system, e.g. for use in lab-on-a-chip assays, a combination of dielectric optical waveguides with microfluidics seems promising [59, 60]. However, truncated dielectric waveguides are commonly considered to have too low photon collection efficiency and a too low signal-to-noise ratio (SNR) to allow for direct lens-free single-molecule detection. Nevertheless, recent experiments suggest that single-molecule detection in aqueous solution via dielectric waveguides is possible [1, 61]. Using a method based on the reciprocity theorem of electromagnetic theory (cf. chapter 2.2.5), it is confirmed in this chapter through numerical simulations and experiments that single-emitter detection via dielectric waveguides is indeed possible. The relevant parameters of the resulting optical system, i.e. the overall detection efficiency and the detection volume, for any type of single-mode waveguide can be predicted. As a relevant example a cleaved single-mode optical fiber is considered and the remote detection of single fluorescent colloidal semiconductor quantum dots is demonstrated experimentally by placing the cleaved fiber end in their close proximity. The results confirm the predicted spatial dependence of the detection efficiency. Besides demonstrating remote detection of single emitters using optical waveguides this also provides the basis for straightforward design and analysis of the optical performance of arbitrary waveguides integrated into micro-fluidic chips, which is demonstrated through simulation of a simple proof-of-concept design.

A fiber-based SMD setup is then demonstrated that is capable of detecting single fluorescent molecules in solutions with concentrations down to the attomolar range, by excitation and detection of single-molecule fluorescence through a cleaved single-mode optical fiber. While simultaneous excitation and detection through the same fiber will lead to high background from inelastically scattered photons in the fiber, the detection efficiency is shown to be large enough under the right conditions to ensure efficient detection of molecules. As outlined in section 2.3, molecule arrival times put increasing constraints on SMD experiments at low concentrations. It is shown that the fiber-based setup used here can overcome this constraints through simple but rapid and turbulent mixing. A closer look at SMD under conditions of flow is taken in chapter 4.

5.2. Simulation of Emission and Detection by Waveguides

In section 2.2.5, an expression was derived (equation 2.37) that provides a method to calculate the fraction of dipole emission which is incoupled into an arbitrary dielectric waveguide in close proximity. By determining the field distribution created by the outcoupled waveguide-mode, it is possible to determine the incoupled power for arbitrary dipole positions and orientations. To verify the reciprocity-based derivation of the incoupling efficiency, it was crosschecked versus numerical mode matching results (2.31). Therefore (i) the electric field $\boldsymbol{E}_W$ that is emitted by the fiber facet and (ii) the electric and magnetic field distributions of a point dipole close to the fiber facet for different dipole positions and orientations with identical geometry has been calculated by means of finite-difference time-domain (FDTD) simulations (FDTD Solutions, version 8.0.0, Lumerical Solutions Inc., Vancouver, Canada). Due to the larger statistical weight of parallel orientations of dipole moments in regard to the waveguide surface, the results in the following part are restricted to this dipole orientation. The fraction of dipole emission incoupled into the fiber mode is maximal for a parallel orientation. Non-parallel oriented dipole moments will result in lowered total incoupled power, but otherwise behave the same. The simulation setup is shown in Fig. 5.1a. A single-mode fiber is modeled by a cylindrical core of dielectric material with index n = 1.4580 and a diameter of 3.5 µm that is surrounded by a cladding of index n = 1.4530. Figure 5.1b shows the cross section of the near-field intensity distribution of the fundamental fiber mode (λ=800 nm), obtained using a finite-difference-frequency-domain (FDFD) algorithm [62] (MODE Solutions, version 5.0.4, Lumerical Solutions Inc., Vancouver, Canada). The single emitter is approximated by a point dipole source with dipole moment parallel to the fiber facet and an emission spectrum modelled as a Gaussian with a center wavelength of 800 nm and spectral width of 60 nm, resembling the emission spectrum of quantum dots and dyes used in the experiments. Figure 5.1c shows a longitudinal section of the field intensity at a free fiber facet normalized to the maximum of the fundamental mode propagating within the fiber. As the beam exits the fiber its on-axis intensity first decreases, then increases again to more than 1.5-times the value compared to fiber-mode maximum before finally decaying towards zero. As in the calculated intensity distribution in section 2.2.4, this peculiar behavior reminds of a focusing effect, however, it can be readily explained by considering the Bessel-shaped field distribution inside the fiber [31] which results in a very short-ranged Bessel beam directly after the fiber facet exhibiting typical intensity oscillations [34, 37]. Similarly, after a distance of about 5 µm, the Bessel beam breaks down and the beam starts to diverge and gradually approaches the behavior of a Gaussian beam with a divergence compatible with the fiber's numerical aperture (NA = 0.12).

Now all the ingredients to perform the aforementioned crosscheck are available. A linear relation between the efficiency η of SE power coupled into the waveguide mode and the square of the absolute value of the projection of the fiber-mode field-component

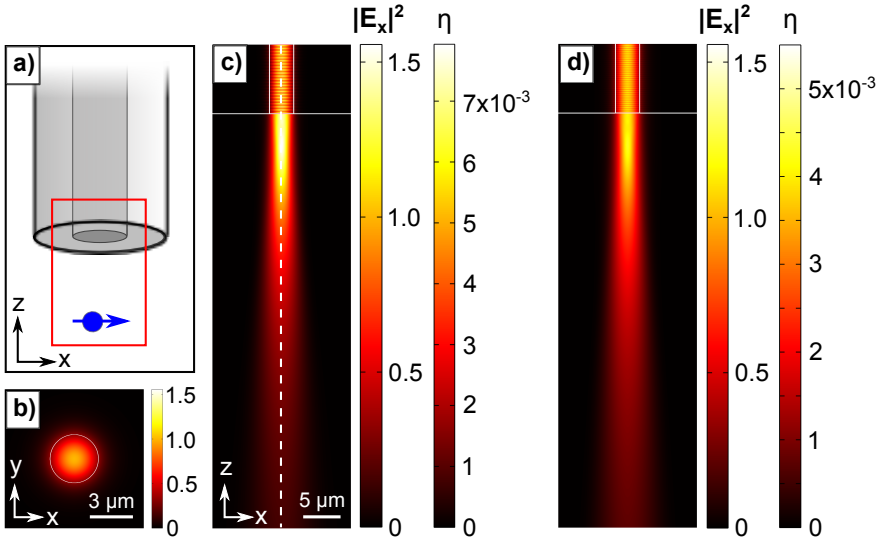

Figure 5.1.: **(a)** Geometry used in simulations. A single-mode fiber sits at variable distance z above a point dipole. The red box denotes the actual simulation volume, as pictured in (c). **(b)** FDFD-simulation of the fundamental fiber mode profile (λ=800 nm) inside the fiber. **(c)** x-component of the normalized electric field intensity $|\boldsymbol{E}_W|^2$ of the outcoupled fundamental fiber mode (longitudinal section including the optical axis (white dashed line) of (a) in air. The identical plot can be used to show the position dependence of a SE's in-coupling efficiency η when it is oriented along the x-axis. The two different scales differ only by a constant factor β. **(d)** outcoupled fiber mode in water, analogous to (c). The lowered field-confinement results in reduced in-coupling efficiency. Figure adapted from [2], © 2014 American Physical Society.

at the position $\boldsymbol{r}_0$ onto the SE's dipole moment unit vector $\hat{\boldsymbol{p}}$ is found:

$$|\boldsymbol{E}_W(\boldsymbol{r}_0) \cdot \hat{\boldsymbol{p}}|^2 = \beta \cdot \eta \tag{5.1}$$

This allows to calculate the in-coupling efficiency of SE emission into the fiber mode using the intensity distribution caused by mode excitation (see Fig. 5.1c, right scale). For the simulated geometry, evaluating several SE positions along the optical axis, the scaling factor $\beta = 196.2$ is obtained, with a standard deviation $\sigma_\beta = 0.5$, which is due to slight spatial variations of β caused by numerical artefacts. Using the scaling factor, a maximum in-coupling efficiency of η=0.79% has been calculated, corresponding to the SE positioned in the intensity maximum of the outcoupled field. Similarly, it is possible to simulate a waveguide out-coupling into water, which will be of importance for experiments later in this work. Replacing the lower halfspace with water (n=1.33), the scaling factor $\beta = 282.3$ is obtained, resulting in a maximum in-coupling efficiency of η=0.43%. Obviously, the higher refractive index leads to a lowered confinement of the outcoupled field, in turn reducing the in-coupling efficiency of emitted photons

into the waveguide mode. The calculated value is of the same order of magnitude as the efficiency obtained from ray optics in section 2.2.2 (0.3%), but in particular offers the possibility to determine the spatial distribution of the photon collection efficiency of the fiber.

5.3. Detection of Single-Molecule Emission by Waveguides

5.3.1. Experimental Setup

In order to experimentally verify the predicted spatial dependence of the in-coupling efficiency, a carefully cleaned microscope cover slip (Menzel cover glass "# 1.5", thickness 0.17 mm) was spincoated with a 100 pM solution of QDot800 ITK Carboxyl quantum dots (QDs) (Invitrogen/Life Technologies) and a subsequent 200 nm layer of PMMA. Excitation of the quantum dot fluorescence is provided by an asymmetric dark-field scheme employing an off-axis needle-like beam that is created by placing a small aperture (diameter 1.5 mm) in the beam path of a coherent white-light source (λ= 530 nm, SuperK Power with SpectraK AOTF, NKT Photonics) and displacing the lens laterally to the beam axis. The beam is thus focused at an incidence angle close to the critical angle of total internal reflection, which exceeds the numerical aperture of the fiber. This configuration provides efficient excitation of quantum dots while keeping the background in the detection path very low. As the focusing lens a microscope objective (1.30 NA, PL Fluotar 100x, Leica) is used, resulting in a spot-size of $\approx$ 1 µm×2.5 µm. For imaging, the sample is scanned in the x-y-plane using a piezo stage (P-527.3CD, E-712, PI Physik Instrumente). To collect the fluorescence, a cleaved single-mode optical fiber (FS-SN-3224, Thorlabs) is situated perpendicular to the surface at a variable distance z ranging from about 2 to 50 µm, adjusted by a piezo positioner (PIFOC, PI Physik Instrumente). To perform a distance calibration the mechanical contact between fiber and sample was detected by imaging the sample with a CCD camera and observing a sudden defocusing of the sample upon approach of the fiber. Quantum dot fluorescence entering the fiber is outcoupled at the far end and focused onto a single-photon-counting avalanche photodiode (APD) (SPCM-AQR-13, Perkin-Elmer) after passing a band-pass filter (XF-3307, Omega Optical) to remove remaining excitation light. For a schematic drawing of the experimental setup see Fig. 5.2.

The analysis of recorded scanning images was performed by fitting a 2D elliptical Gaussian to the recorded spots. Since the fiber gathers light from a sample area comparable to its core diameter, the size and shape of the recorded spots is determined by the illumination point-spread-function (PSF) that can therefore be considered constant. After selecting suitable fluorescence spots and fitting the 2D Gaussian, the resulting amplitude was used as a measure for the quantum dot emission coupled into the fiber.

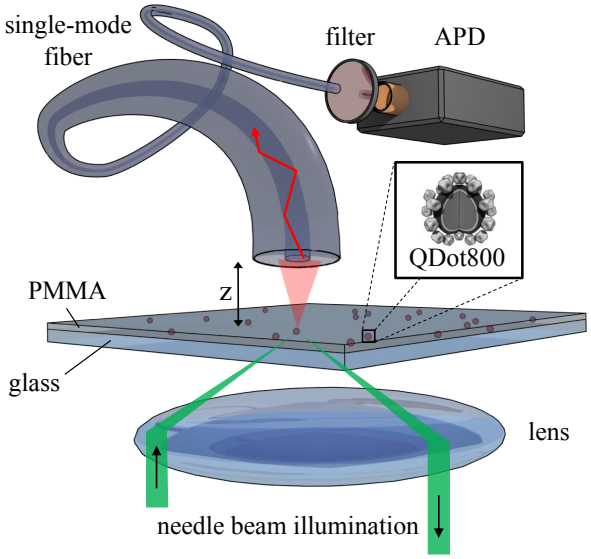

Figure 5.2.: Experimental setup: a single mode fiber is situated above a microscope cover slip coated with QDot800 (red spheres, inset) in a 200 nm thick PMMA layer. On the other end of the fiber the quantum dot fluorescence is delivered to an APD through a filter. Figure from [2], © 2014 American Physical Society.

5.3.2. Simulations of the Experimental Geometry

To afford a direct comparison with the setup used in the experiments, the intensity distribution and in-coupling efficiency in presence of a substrate at varying distances (as also depicted in Fig. 2.8) supporting a layer that contains the single emitters was simulated. The dipole source is held in a 200 nm thick PMMA layer (n = 1.48431) [63] on top of a semi-infinite glass substrate (n = 1.45334; comparable to material used in experiments) [64]. The results are shown in Figure 5.3 (black dots). The decay observed without an additional surface is now superimposed by a weak oscillation caused by Fabry-Perot interferences between the reflecting fiber and sample surfaces, showing a period of half the wavelength. These interference oscillations increase in amplitude for small distances, as shown in the inset of Figure 5.3. As a reference, the incoupled power for the free fiber case (i.e. no substrate), obtained by reciprocity is shown in Figure 5.3 (red solid line). The curve fits nicely to the overall trend of the distance-dependence which has been observed for the previously described geometry (see figure 5.1), but appears to be shifted to smaller values. This deviation can be explained by reflections at the air-PMMA interface, leading to lower intensity at the SE position. Owing to reciprocity, the power incoupled to the fiber mode changes accordingly, when compared to the case of a free fiber. Taking this into account one can get almost perfect agreement between the free fiber case and the exact, more complicated geometry (Figure 5.3, red dashed line). Additionally, the oscillatory behavior is contributing to the relatively large spread seen in the experimental data. The PI-

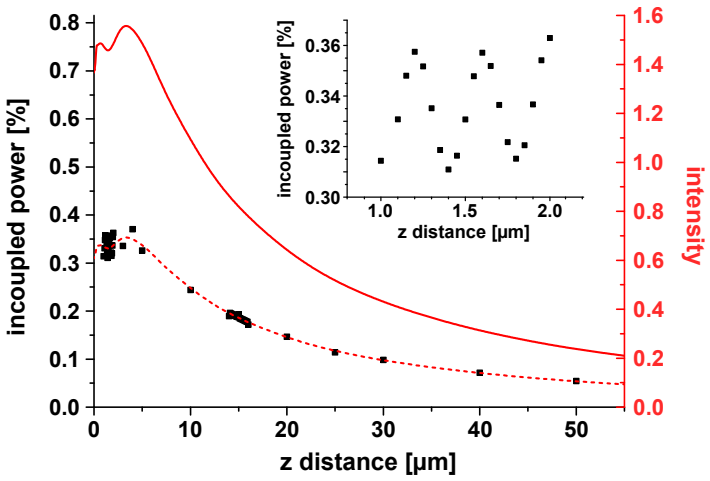

Figure 5.3.: Simulated SE in-coupling efficiency for various distances between fiber and SE. The black dots represent the incoupled power of a SE embedded in a PMMA layer on top of a glass substrate at various distances to the fiber. The red solid line shows the incoupled power for the case of a free fiber, obtained by reciprocity. The red dashed line includes the expected reflection at the air-PMMA interface. The scaling of both axes of ordinates is linked via reciprocity. The inset is a magnification of the region around 1.5 µm distance. Figure from [2], © 2014 American Physical Society.

FOC piezo-scanner used for step-wise adjusting of the fiber-sample distance provides nanometer accuracy, however the absolute distance, and therefore the zero-point on the z-axis, cannot be determined with similar accuracy. Since the uncertainty in the fiber-sample distance is on the order of a quarter wavelength, an additional uncertainty of about the modulation amplitude of the intensity distribution (about 10%) in the gap has to be considered.

5.3.3. Emitter-Fiber Distance Measurements

Figure 5.4a shows three representative images obtained by raster-scanning the sample and recording the fluorescence signal at each pixel. Spots of fluorescence emission originating from quantum dots are clearly visible, with a signal-to-noise ratio of up to ∼15. To determine the distance dependence of the in-coupling efficiency into the fiber, raster scans of the same sample region for a range of sample-fiber distances between 2 µm and 50 µm have been recorded. As the total detected number of photons of each individual QD will depend on the orientation of the QD's emission plane [26] relative to the orientation of the fibers optical axis, each individual QD spot will exhibit a different maximum amplitude. Therefore, each single-QD distance dependence was normalized to its maximum emission intensity. The experimental data are depicted in Fig. 5.4b together with the normalized analytical and simulation results of the intensity of the outcoupled fiber mode along the optical axis.

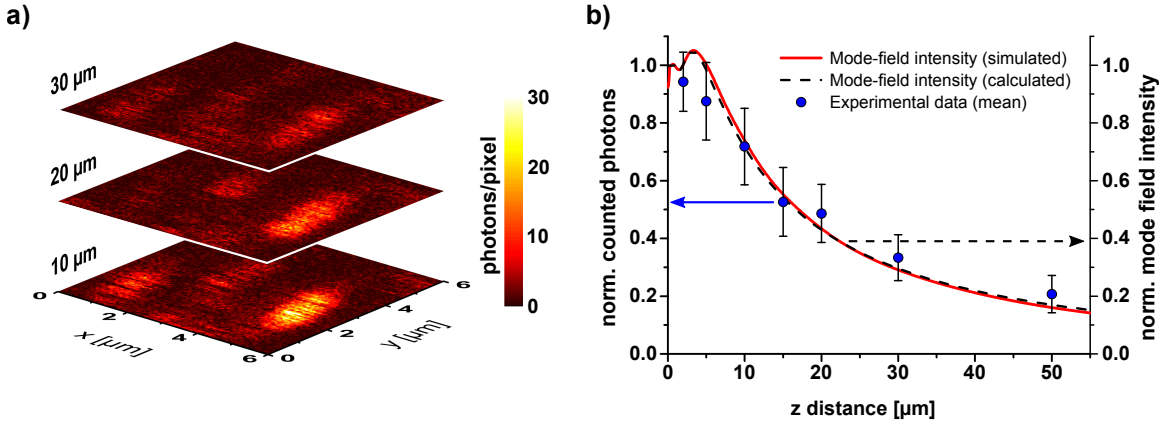

Figure 5.4.: **a)** Fluorescence images of a sample area (6 µm × µm, 120 × 120 pixels, 3 ms/pixel) containing the signatures of three quantum dots recorded at fiber distances of 10 µm, 20 µm and 30 µm from the PMMA surface. The spots differ in amplitude and exhibit "dark" lines due to blinking. The elongated shape of the spots is a result of the illumination conditions. **b)** Normalized photon count from 28 emission spots of QDot800 (left axis). The blue dots indicate the mean value. The red line is showing the simulated mode-field intensity resulting from a cut along the optical axis in Fig. 5.1c (right axis). The dashed black line indicates the analytically calculated mode-field intensity along the optical axis obtained by assumption of a Bessel mode outcoupled at the fiber end-facet (see fig. 2.7). Figure from [2], © 2014 American Physical Society.

Note that several factors add to the relatively large spread observed in the experimental data. The main contributions are due to fitting uncertainties, caused mainly by the blinking of the QD800, and distance dependent intensity oscillations due to the presence of the interface and some uncertainty in the absolute fiber-sample distance (cf. appendix 5.3.2). Overall, the observed distance dependence of the in-coupling efficiency is in good agreement with predictions. The detected quantum dot fluorescence signal is decaying with increasing gap between fiber and sample, decreasing to half of the maximum signal at a distance of ∼20 µm. It can be concluded that in a microfluidic chip, to ensure efficient single-molecule detection via an integrated waveguide with comparable NA, analyte molecules have to pass the waveguide facet within a distance of 20 µm or less. The maximum distance to sustain effective single molecule detection will depend on the characteristic field distribution of the waveguide and the background noise and thus the SNR of the measurement. For an application in a lab-on-a-chip device the same waveguide can be used for both excitation and detection. Due to the large illuminated liquid volume and possible scattering processes within the waveguide, background noise can become significant, demanding for short waveguides and high manufacturing quality to maintain a suitable SNR. In an alternative geometry that avoids such problems, two waveguides, one for excitation and

one for detection oriented perpendicular to each other, can be used. In both cases the intensity distribution of the outcoupled fields will affect both detection and excitation, which depend on the relative position of the analyte molecule with respect to the waveguides. In comparison to detection schemes employing standard microscope objectives, the overall detection efficiency of waveguide-based systems is low. A typical objective with a numerical aperture of 0.85 will result in a maximum collection efficiency of almost 0.3 (30%) [54], if the molecule's dipole moment is oriented perpendicular to the optical axis. However, it should be noted that the presence of an interface between molecule and objective will limit the maximum collection angle due to total internal reflection at the interface, reducing the efficiency (cf. chapter 3). Despite the reduced collection efficiency it can be seen that single molecule detection with waveguides can be achieved, if background contributions are carefully controlled.

5.4. Single Molecule Detection in Solution with a Fiber-based Setup

Combining the small dimensions and flexibility of optical fibers with the potentially short measurement times achievable by active transport into a single molecule sensor, suggest applications in restricted geometries, point-of-care diagnostics, and in time-critical assays. Specifically this may include direct, on-site, and real-time detection of viruses by means of their specific DNA, the detection of other pathogenes including proteins, real-time monitoring of rare but important marker molecules in medical applications, or mobile environmental ultra sensing. For this work a setup was used whose principle was originally developed by P. Haas, A. Wild and B. Hecht in Basel[65, 66]. It combines the characteristics of waveguides and active flow into a compact and simple, yet powerful scheme for single molecule detection, able to demonstrate SMD at concentrations in the attomolar range [1].

5.4.1. Experimental Setup

The experimental setup is depicted schematically in figure 5.5a (for further details see appendix A). To minimize background, the system has been optimized for fluorescence detection in the near infrared (750 - 830 nm), as few naturally occurring compounds emit fluorescence above 600 nm [3]. The excitation light (635 nm, 2 mW at the fiber exit) is transmitted through a 20-30 cm length of optical fiber and emitted via a 90°-cleaved fiber end into the liquid sample volume. Here it excites single molecules close to saturation whose fluorescence is coupled back into the fiber if they reside in the detection volume. The excitation power of 2 mW has been found to provide the best signal-to-noise ratio and to ensure mostly saturated excitation of the dye molecules in previous experiments [66, 67].

Following the method described in sections 2.2.5 and 5.2, the photon collection efficiency of a single-mode fiber as used in the experiments and submersed in water can be calculated. For fluorescence photons emitted around 800 nm the peak collec-

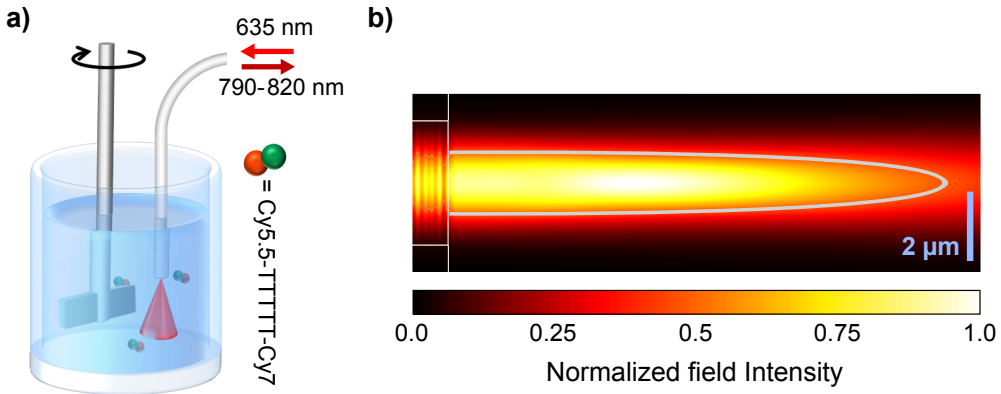

Figure 5.5.: Principle of quantitative single-molecule detection at ultralow concentrations using excitation at 635 nm and fluorescence detection at 790-820 nm. **a)** Schematic experimental setup showing the analyte container with the optical fiber positioned close to the rotor blades and some analyte molecules (green-red dots). **b)** Estimated detection volume of a single-mode optical fiber as used in the experiments (center plane). The rectangular area to the left is the fiber core. The figure has been obtained by convoluting the field-distribution of the 800 nm fiber mode launched from fluorescence photons emitted by analyte molecules and the 635 nm mode launched by the laser, responsible for excitation. The gray elliptic outline depicts the FWHM. The blue scale bar has a length of 2 µm. The total volume inside the ellipse resembles an ellipsoid with a volume of 24 fL. Figure adapted from [1], © 2010 American Chemical Society.

tion efficiency is found to be ≈0.45 %, i.e. about 0.45 % of the total emission of a molecule is transmitted through the fiber towards the detector (cf. section 5.2). Since the same fiber is used to excite the molecules, the effective detection volume will depend not only on the incoupling efficiency into the fiber mode at 800 nm, but on the outcoupled intensity distribution of the 635 nm fiber mode launched by incoupling the laser into the fiber. Therefore the total detection volume can be estimated by a convolution of the outcoupled 635 nm mode with the 800 nm mode. Taking the full-width-half-maximum (FWHM) of the resulting spatial distribution, the detection volume resembles an ellipsoid centered on the fiber facet and with a semi-major axis of 14 µm and a semi-minor axis of 0.9 µm, for a volume of ≈20 fL. The resulting cumulative spatial detection efficiency obtained from the respective simulations is depicted in figure 5.5b.

The effect of the outcoupled mode that is used to excite the molecules on the shape of the detection volume can however depend strongly on the encountered local intensity. The photon emission by fluorescent molecules is subject to the excitation intensity and will saturate for high intensity. In that case, the detection volume will effectively depend mostly on the incoupling efficiency as determined in section 5.2, while the contribution by the outcoupled mode will be "flat". Since the experiments in this work

have been conducted just below the onset of saturation, a roughly linear response to the excitation intensity can be expected.

The use of a single-mode fiber as optical transducer is hindered due to background generated by inelastic scattering processes in the fiber, exhibiting a spectrum extending $\sim$ 100 nm beyond the excitation wavelength. The fiber background is proportional to the intensity coupled into the fiber as well as to the length of the fiber. For fiber lengths of 30 cm, this generic background could already prevent successful single-molecule detection using standard dye molecules with their typically rather small Stokes shift. However, the Stokes shift can be increased by using a covalently linked donor-acceptor pair of dye molecules exhibiting efficient fluorescence resonant energy transfer (FRET) or suitably chosen colloidal semiconductor quantum dots. Here a Förster pair consisting of 5 thymidine bases connecting a Cy5.5 molecule at the 3' end and a Cy7 molecule at the 5' end (Cy5.5-TTTTT-Cy7, Genelink and Microsynth) is used. The Förster pair is excited at a wavelength of 635 nm while the emission maximum for Cy7 occurs at 767 nm - well within the setup's detection bandwidth (see appendix B).

5.4.2. Single Molecule Detection Experiments

Figure 5.6 displays a time trace of measured photons with a binning time of 100 µs recorded from a 10 pM dye solution with the rotor initially turned off. The trace shows a constant level of background counts with a Poissonian distribution due to background generated in the fiber, but no fluorescence bursts due to diffusing molecules. As soon as the stirring is switched on (after 20 s), fluorescence bursts appear at a high rate and the histogram deviates from a Poissonian distribution. It may be noted that the signal-to-noise ratio seems to be unusually small compared to conventional single-molecule experiments. However, due to the fact that the fluorescence bursts can be clearly distinguished from the Poissonian background, detection of single-molecule events is possible with high efficiency (see [55]). Small improvements of the signal-to-noise ratio will lead to a further increased detectability. Since molecules can only be efficiently collected if they reside within a relatively small volume close to the fiber end (see section 5.2), diffusion is no longer sufficient at low concentrations (pM and below) to have a sufficient number of molecules passing the detection volume per unit time. In addition, excitation of molecules takes place in a much larger illuminated volume, albeit at lowered intensity, due to the Bessel-like beam emerging from the fiber end. Therefore, even for moderate concentrations, stirring is needed to ensure that enough molecules reach the effective detection volume before being bleached (figure 5.6, rotor off). Stirring rates of 20000 rpm have been found to yield best results if at the same time the relative position between fiber and rotor is optimized (see section 5.4.3). For the characteristic dimensions of the rotor (r=1.5 mm) and the rather large velocities imposed by the stirring, Reynolds numbers of several thousands are easily achieved. The result is a highly turbulent flow in the sample volume which ensures rapid mixing [68]. It is expected that the fiber end acts as a discontinuity in the flow profile, which leads to the formation of additional vortices at the fiber end, which ensure the

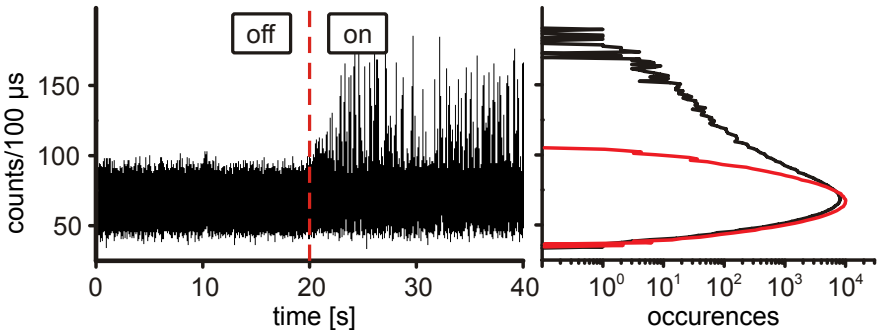

Figure 5.6.: Fluorescence time trace recorded from a 10 pM solution showing the difference between rotor off (0-20 s) and on (20-40 s), respectively. Right panel: Corresponding histograms calculated separately for rotor on (black trace) and off (red trace) showing a deviation from Poisson distribution only for the rotor-on case. Figure from [1], © 2010 American Chemical Society.

rapid exchange of fluorescent molecules in the detection volume at the fiber facet close to the core. The fact that detection of molecules for too low stirring rates is impossible indicates a sudden onset of vortex formation at the fiber end at rotor speeds of $\sim$ 5000 rpm. The onset of vortex formation is also supported by an autocorrelation analysis of recorded time traces, which shows a broadening of the fluorescence bursts instead of a narrowing for higher stirring rates (see figure 5.9b). These additional vortices do not appear in the vicinity of an infinitely extended boundary between liquid and glass which is encountered in detection schemes based on microscope objectives. In addition, the typical small working distances of high-numerical-aperture microscope objectives limit the accessible detection range to the low-velocity flow sheets encountered close to the surface (as seen in section 4.4).

In order to demonstrate the possibility to detect ultra-small concentrations of dye molecules within short measurement times of 60 s, a series of measurements has been performed for solutions with analyte concentrations varying over six orders of magnitude between 100 pM and 100 aM. Each acquired 60 s time trace is subjected to an analysis by a burst counting algorithm to determine the number of fluorescence bursts (see section 3.4 and [55]). Figure 5.7a shows typical 10 s portions of fluorescence time traces obtained from solutions containing analyte molecules in concentrations as indicated together with the respective histograms. For the higher concentrations ($\geq$ 1 pM) the mean number of molecules that enter the detection volume per bin time is larger than one, causing occasional large count rates. In the corresponding histograms this leads to a pronounced deviation from the Poisson distributed background with a rather broad range of large amplitude bursts. With decreasing concentration, the number of detected fluorescence bursts decreases and the peak count rate above background observed in the histograms tends towards $\sim$50 counts/100 µs, limited by the saturation emission rate of single Cy7 molecules and the maximum overall detection efficiency.

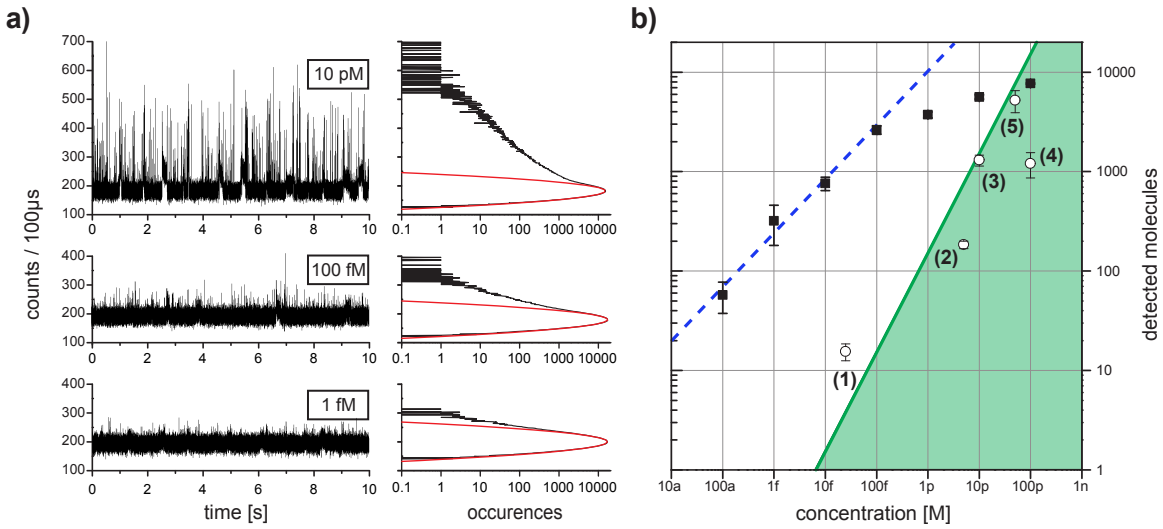

Figure 5.7.: Dilution series. **a)** Representative 10 s portions of 60 s time traces for different concentrations of dye molecules as indicated as well as respective histograms (black) with best fits to the Poissonian background (red) as needed for burst detection. **b)** Filled squares: counted bursts above threshold as a function of the concentration measured within a 60 s integration time. A linear dependence is obtained between a concentration of 100 fM down to 100 aM (**blue dashed line as guide-to-the-eye**). Above 100 fM the number of counted bursts deviates from linearity since bursts start to overlap in time (see [55]). Open squares: Experimental data for diffusion-based assays taken form the literature (1:[69], 2:[70], 3:[71], 4:[72], 5:[73]). Note that [69] relies on active transport of analyte molecules through a capillary. All values have been scaled to a detection value of 10 fL. Solid **green** line and shaded area: Theoretical upper limit and accessible area of the number of molecules entering the detection volume during 60 s considering Brownian motion only, see section 2.3.2. Figure from [1], © 2010 American Chemical Society.

At a concentration of 100 aM, the number of detected fluorescence burst is still on the order of several tens. This number does not only allow a reliable detection of single molecules at this concentration but lets reasonably envision an extension of the technique to even lower concentrations. Quite remarkably, 100 aM is already about 1000× smaller than the smallest concentration reported in the literature for diffusion-based single-molecule detection [70, 71, 72, 73]. Figure 5.7b summarizes the results obtained by measuring a dilution series with the fiber-based setup. As a reference, values for conventional diffusion-based single-molecule detection experiments in solution as reported in the literature are plotted as well. Furthermore, the expected number of molecules that enter the detection volume within 60 s enter solely due to Brownian motion as a function of the concentration (solid green line) is plotted, according to the discussion in section 2.3.2. This line describes the upper limit for the number of

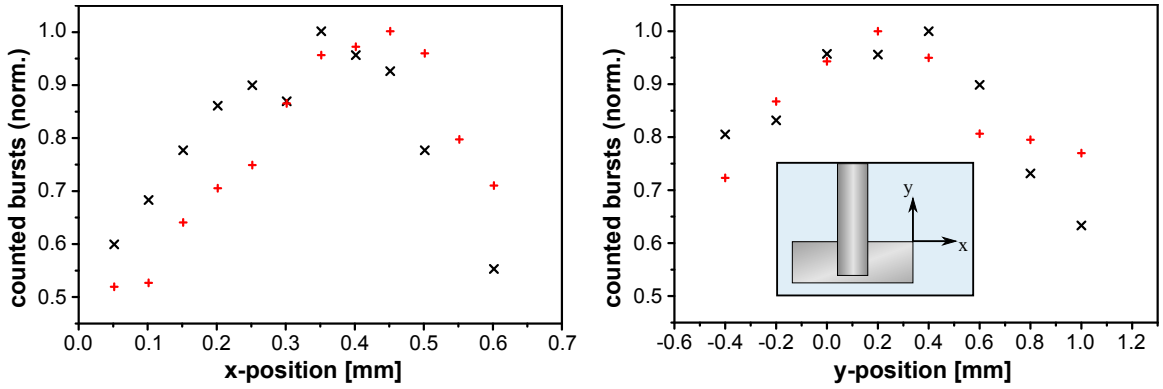

Figure 5.8.: Dependence of the number of fluorescence bursts on the radial fiber position (left) and vertical fiber position (right). The position is determined outwards from the edge of the rotor. (+) has been measured from high to low values, (x) from low to high values. Figure adapted from [1], © 2010 American Chemical Society.

detected molecules during 60 s in a conventional diffusion-based single-molecule assay while the shaded area designates the regime accessible to conventional single-molecule detection assays. In conclusion it is clearly demonstrated that by combining turbulent flow and detection through a finite-sized optical fiber the fundamental detectability limit of diffusion-based single-molecule detection assays can be overcome. As a result, fast quantitative single-molecule detection down to concentrations of 100 aM has been achieved.

5.4.3. Optimization of the Fiber Sensor

Since the velocity profile in the sample container varies as a function of the distance to the rotor, it is to be expected that the detection rate of the setup strongly depends both on the stirring rate of the rotor and on the fiber position relative to the rotor. Therefore, to optimize the detection rate, an optimal fiber position and stirring rate has been determined. To this end, series of 30 s time traces have been recorded at different axial and radial positions of the fiber at a fixed stirring rate of 20000 rpm. Coordinates have been determined by measuring the distance to the upper corner of the rotor, counting outwards (see inset in figure 5.8). To limit the influence of bleaching, the measurements have been conducted at high concentrations (100 pM) and the experiment is performed both by moving the fiber outwards and inwards. After each separate measurement the fiber was moved by 50 µm to a new position. Figure 5.8 shows the result of the radial (x) variation of the fiber position. A maximum in the number of counted bursts is found at a fiber position of 0.45 mm when moving from 0.6 mm to 0.05 mm and at a fiber position of 0.35 mm when moving back, respectively. Accordingly, a position of x=0.4 mm has been chosen for all subsequent measurements.

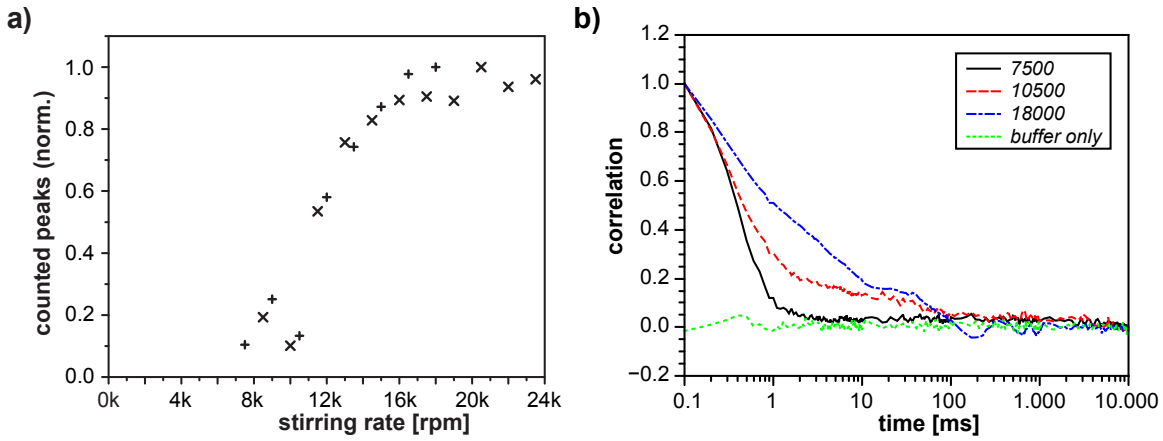

Figure 5.9.: **a)** Dependence of detected molecules on the stirring rate at fixed position. (+) has been measured form high to low values, (x) from low to high values. **b)** Autocorrelation of three time traces at different stirring rate from a), showing increasing fluorescence burst-width for increasing stirring rates indicating the formation of vortices. An additional shoulder is visible for stirring rates $>$ 7500 rpm, indicating two sources for intensity fluctuations with different time constants. The autocorrelation has been normalized for better comparability. Figure adapted from [1]

The optimal position in axial (y) direction has been determined in similar fashion. A set of measurements has been performed changing the height of the fiber in steps of 200 µm. A maximum is found at a position of 0.3 mm as seen in figure 5.8. Accordingly, for subsequent measurements a position of y=0.3 mm has been chosen. In comparison to the radial fiber scan, the maximum in the y-scan is much broader. Therefore the vertical position of the fiber can be considered less critical for optimal detection.

In similar experiments, time traces have been recorded for different stirring rates but at fixed radial and vertical position. At stirring rates above ≈16000 rpm the number of detected molecules begins to saturate (see figure 5.9). A rate of 20000 rpm, well within saturation, has therefore been chosen for the experiments. Additionally an autocorrelation analysis of time traces recorded at different stirring speed (1 pM concentration) has been performed, which shows increasing burst-width for increasing stirring speed indicating the formation of vortices. The results are displayed in figure 5.9b. Additionally the tilt of the fiber relative to the flow has been found to influence the detection efficiency. Best results were obtained when the fiber was slightly tilted into or out of the flow direction by $\sim$ 5-10°, which can favor the formation of vortices at the fiber end-facet.

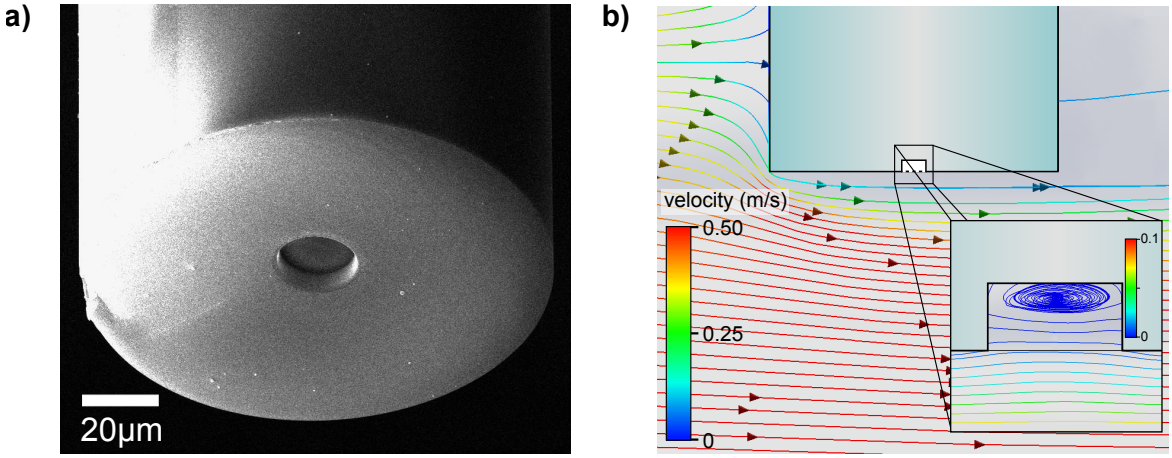

Figure 5.10.: **a)** SEM picture of an optical single-mode fiber modified with a centered pod-like structure (Ø=20 µm, depth 6 µm). **b)** Simulation of flow (v_∞=0.5 mm/s) at the end facet of a modified fiber. The flow lines are color-coded with the local flow velocity. The pod (zoomed-in view in inset) creates a low-velocity vortex potentially capable of trapping analyte molecules. Note the different scale in the inset.

5.4.4. Manipulating the Flow for Improved Detection

As demonstrated in the previous sections, the fiber sensor is relying on very high stirring rates for effective detection of molecules. While first fluorescence bursts begin to appear around 6000 rpm, below stirring rates of ≈ 12000 rpm no significant numbers are detected during experiments and stirring rates above 16000 rpm are necessary for optimal detection. Since autocorrelation analysis of measured time traces showed an increased residence time (fluorescence burst-width) for high stirring rates, it was concluded that small vortices begin to form at the fiber end, capable of temporarily trapping molecules. At such high stirring rates and thus high Reynolds numbers, the flow within the sample volume is highly turbulent and chaotic, complicating calibration of the setup.

Following the concepts from chapter 4, artificial structures could be created to manipulate the flow at the fiber end in a way to allow successful SMD at lower stirring rates. In particular creating a step-like structure should lead to the creation of a small vortex directly behind the step. An easy realization of such an idea was found in the form of a small pod-like pit at the fiber end, which can be created through focused ion beam (FIB) milling. To this end, cleaved and thoroughly cleaned fiber tips are coated with a thin layer of gold to create a conductive layer preventing charging effects. A circular pod (Ø 15-30 µm, depth 5-15 µm) is then milled into the central part of the fiber end with the FIB. A SEM picture of one of the resulting structures can be seen in figure 5.10a.

With the help of the flow simulation module of Solidworks (Dassault Systemes Solidworks 2012), a 3D simulation of the flow around a model of a modified fiber tip was

performed. In figure 5.10b the resulting flow lines at an initial flow velocity of 0.5 m/s are depicted. The color of the flow lines corresponds to the local flow velocity. The flow is deflected around the fiber, creating a low-velocity surface flow directly at the fiber surface. A zoom-in to the central part containing the pod (inset in figure 5.10b) illustrates that a vortex is formed inside the pod, in line with expectations. Flow simulations at different velocities confirm the formation of similar vortices at both lower and higher stirring rates.

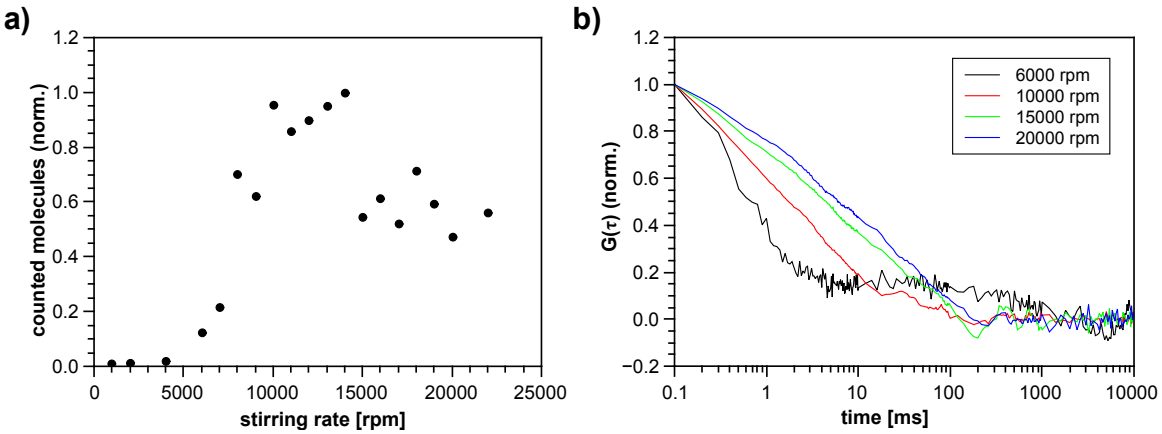

Figure 5.11.: Molecules detected with a fiber modified with a pod structure(Ø=25 µm, depth 15 µm). In comparison to simple cleaved fibers, detection of molecules is possible at lower stirring rates and less effective at higher stirring rates.

The results of one series of measurements in which the influence of the stirring rate on the number of detected molecules was investigated is shown in figure 5.11. The pod structure for this fiber has a diameter of 25 µm, and a depth of 15 µm. With this modification, a notable detection of single molecules takes place at stirring rates above 6000 rpm, while the molecule count rate saturates at stirring rates as low as 10000 rpm, in obvious contrast to the results with unmodified fibers. For stirring rates of 15000 rpm and above the number of detected molecules decreases again. Overall the number of detected molecules is fluctuating more than with the unmodified fibers, indicating that the postulated vortex inside the pod might not be table or rather be influenced strongly by the turbulent flow in the sample container. An autocorrelation analysis of the recorded time traces again shows an increase in burst-width with increasing stirring rate (figure 5.11b), similar to the experiments with the unmodified fibers. In comparison, the autocorrelation of the traces obtained from the modified fibers shows much longer burst-widths than the normal fibers, compatible with the formation of low-velocity vortices inside the pod structure. It is possible that the decline in the number of detected molecules observed for stirring rates above 14000 rpm is a result of decreasing exchange of molecules between the high-velocity flow around the fiber and the low-velocity vortex inside the pod. While only a limited number of experiments have been conducted with modified fibers, these preliminary

results show that a manipulation of the flow on the microscale can be used to influence and potentially enhance SMD experiments.

5.5. Conclusions

A theoretical and numerical method to assess the detection efficiency of arbitrary dielectric waveguides in single molecule detection experiments has been presented in this chapter. The method was used exemplarily to predict the spatial distribution of the detection efficiency for a single-mode optical fiber. The predicted behavior could be confirmed experimentally by detecting single semiconductor quantum dots at varying distances along the optical axis from the end facet of an optical fiber. The advantage of this method is that it is providing a simple way to analyse and optimize arbitrary waveguides. This can provide increased detection efficiency or a way to adapt them to different experimental problems, helping in the design of compact and fully integrated optofluidic lab-on-a-chip setups. As a simple example, an optical fiber terminated by a hemispherical lens positioned on top of the guiding core is considered. The resulting field distribution is shown in figure 5.12. This simple modification already yields a maximum field strength and consequently detection efficiency that is one order of magnitude larger than the one achieved with a simple cleaved fiber. The price to pay for the increased absolute efficiency is a smaller detection volume - but this again can be desirable e.g. for single molecule experiments at higher concentrations, where it would not be possible to probe single molecules with large detection volumes.

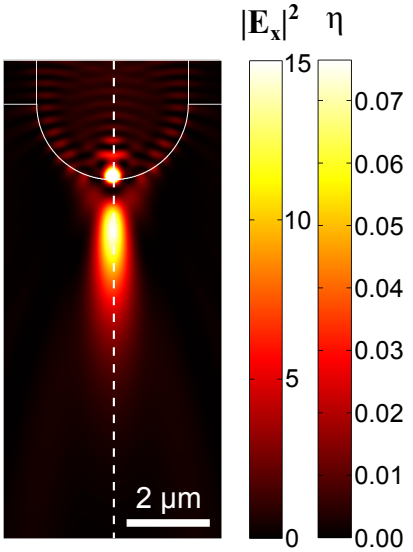

Figure 5.12.: Simulated intensity distribution of a single-mode fiber with a hemispherical lens placed on top of the core. Compared to a cleaved fiber, the outcoupled field is concentrated in a small volume, resulting in much higher local intensity and detection efficiency, respectively. Figure from [2], © 2014 American Physical Society.

In the second part of this chapter, an experimental implementation of SMD via dielectric waveguides was demonstrated. A sensor based on a commercially available single-mode fiber was shown that is able to detect molecules down to attomolar concentration. Here, the diffusion limit was overcome by providing active transport of analyte molecules by means of rapid mixing. The resulting turbulent flow deviates from the results derived for laminar flow in the previous chapter and results in increased demands for careful calibration of the sensor. Autocorrelation analysis of the recorded time traces has revealed the formation of vortices for high stirring rates, which are believed to play an important role in the detection process by trapping molecules in the detection volume.

In a first set of proof-of-principle experiments, the possible advantages of structural manipulations to the fiber's end-facet to improve local flow close to the fiber core was investigated. The experiments revealed that by simple modifications a low-velocity vortex was created and the stirring rate necessary to detect single-molecule events with the fiber sensor could be reduced. While a more in-depth investigation is necessary, the initial results seem promising to reduce the necessity for careful calibration of such fiber sensors.

Overall the fiber-sensor was demonstrated to provide an efficient approach to fast SMD at low analyte concentrations by means of dielectric waveguides.

6. Single Molecule Detection in Microfluidic Chips

6.1. Motivation

The concept of Lab-on-chips (LOCs), the miniaturization of multiple different functionalities onto a single substrate has been compared to the impact of integrated microelectric systems in its possible influence on life sciences [74]. The great potential of microfluidic LOC systems is the integration of an entire diagnostic procedure into a small and easy-to-use device that can offer fast, sensitive and cost-efficient detection of e.g. disease markers or environmental pollutants. The promise for point-of-care diagnostics in particular has led to huge interest from the research community and industry in the last decade. Overviews on development, methods and future possibilities of LOCs can be found in [75, 76, 77, 78, 79].

So far the combination of compact, integrated optics with microfluidic devices has proven difficult to realize, despite great interest due to the versatility of fluorescence-based detection schemes. This chapter describes a series of experiments that have been conducted with microfluidic chips containing dielectric waveguides that can be used to excite and collect fluorescence from analyte molecules in an internal fluid channel on the chip. The microfluidic chips have been produced in the group of Roberto Osellame and Giulio Cerullo at the Istituto di Fotonica e Nanotecnologie at the department of physics of the University of Milan.

6.2. Design and Fabrication of Microfluidic Chips

6.2.1. Design

To realize the goal of detecting single molecules with an LOC, it is necessary to combine a suitable detection scheme with sample containment and transport in a single, compact experimental approach. To this end, chips have been fabricated that contain a fluid channel for sample transport which is intersected by dielectric waveguides. By coupling a suitable light-source into the waveguides, emitters located in the fluid channel can be excited. Provided that the resulting emission is coupled into the waveguide with sufficient efficiency, it can be detected with a suitable detector, e.g. an APD. The schematic layout of the microfluidic chips used in this thesis can be seen in figure 6.1. The waveguides are laid out along the long side of an elongated, rectangular block of fused silica (typical dimensions $10 \times 4 \times 1$ mm), while the fluid channel is created along the smaller side of the chip, intersecting the waveguides. During fluid

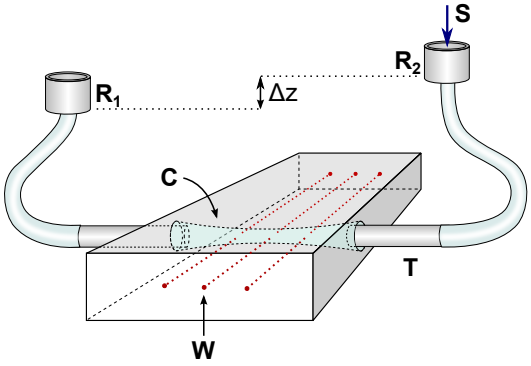

Figure 6.1.: Schematic design of microfluidic chips. The chips are made from small rectangular slabs of fused silica. A fluid channel (C) is reaching through the small side of the chip and is used to transport the liquid sample (S). Tubing (T), consisting of metal needles with flexible silicon tubes is connected with the channel to facilitate filling with sample fluid. The end pieces of the tubes form small reservoirs (R). By changing the height difference Δz between the reservoirs, the flow rate inside the channel can be adjusted. The waveguides (W) are placed along the long side of the chip and intersect the channel. By coupling light into the waveguides, emitters in the fluid channel can be excited.

channel fabrication, the fluid channel shape and direction can be laid out flexibly. For the experiments in this work different variants have been created. An overview of the different chips is available in appendix C. The channel openings are connected with tubing consisting of thin metal needles fixed to the chip and flexible silicon tubes. The ends of the silicon tubes are outfitted with small reservoirs for the liquid sample. By changing the offset Δz between the reservoirs, a hydrostatic pressure can be applied between the reservoirs, which is used to induce flow inside the channel.

6.2.2. Fabrication

The method used in manufacturing of the chips is called *Shape Controlled Femtosecond Laser Irradiation followed by Chemical Etching* (SC-FLICE) [74, 80]. In brief, an Ti:sapphire or more recently, Yb-based bulk or fiber laser is used to irradiate the fused-silica substrate with focused femtosecond laser pulses at repetition rates up to a few MHz. At high enough energy densities, exceeding a given threshold, the dielectric substrate material becomes highly absorbing, enabling permanent material modifications. With increasing laser fluence, those modifications will change from "smooth" modifications with mainly positive or negative refractive index changes (a), to the formation of sub-wavelength nanogratings (b) and finally disruptive modifications due to creation of voids and microexplosions (c). Typically regime (a) is used for the fabrication of waveguides in the substrate, while (b) is used to prepare the substrate for microchannel etching.

Waveguide writing While the underlying physical mechanisms behind permanent refractive index changes in glasses are not fully understood so far, three main theories have emerged as possible explanations [74].

- Formation of color centers: A change in absorption caused by the color-centers results in a refractive-index change (Kramers-Kronig mechanism) [81].

- Thermally induced material densifications: The laser beam induces melting, which on resolidification leads to density variations and therefore, refractive index variations. The density variations can be mediated by so-called *non-uniform cooling*, where a molten region rapidly solidifies from the outward towards the center, putting the center region under pressure due to absence of free surface for expansion.

- Direct structural change by laser pulses: The laser pulse can lead to rearrangement of the network of chemical bonds in the glass matrix, resulting in local density changes that alter the refractive index.

It should be noted that arguments in favor and against all mechanisms could be found in experimental studies of laser-written waveguides. Effectively, a mixture of all three mechanisms is suspected to be involved in the creation of refractive index changes, with the relative importance depending on material and writing parameters.

Microchannel fabrication The fabrication of microchannels by SC-FLICE is a two-step process. After irradiation of the substrate by femtosecond laser pulses, the modified areas are etched by a watery solution of hydrofluoric acid (HF). The refractive index changes induced by laser irradiation are known to increase the etching rate in the according regions. For regime (a), commonly used for writing of waveguides, the change in etching rate is relatively small. In contrast, regime (b) offers a much higher relative increase of the etching rate. This has been attributed to the nanogratings typically associated with regime (b). The nanogratings act as channels for the HF, enabling diffusion of HF into the fused silica. Due to eventual exhaustion of the HF in deeper channels, typically "dead-end" channels produced with this method don't reach further than about 2 mm into the material. By etching the channel from two sides, it is possible to increase the depth of the channels almost by a factor of 2. One of the drawbacks of the original FLICE method is the conical shape of the microchannels. Due to longer exposure and higher etching rate close to the surface of the chip, the diameter of the microchannels would grow smaller with increasing channel length. In contrast SC-FLICE is able to produce a uniform cross-section along the entire length of the channel. This is achieved by irradiating a conical spiral with increasing diameter the further the channel reaches into the material (see fig. 6.2). The increase in irradiated volume effectively counters the decrease in etching efficiency, yielding an uniform channel cross-section along the entire channel. Along with the obvious advantages of uniform channels, longer channels can be produced as well.

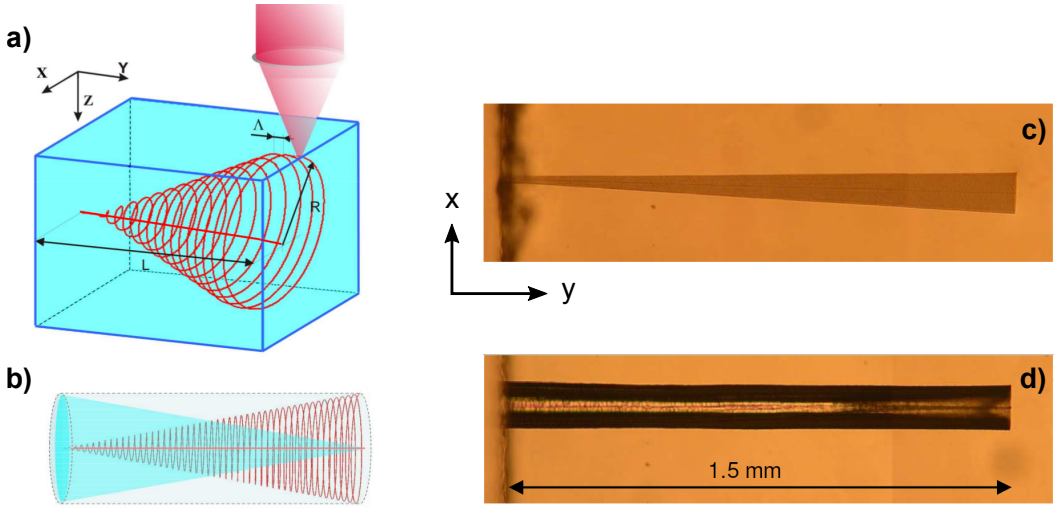

Figure 6.2.: Principle of SC-FLICE microchannel fabrication. **a)** A conical spiral is inscribed into the substrate. **b)** The conical microchannel (blue), compensating conical spiral (red) and final cylindrical microchannel (grey). **c)** Microscope image of the conical spiral inscribed into the substrate and **d)** resulting microchannel. Picture reproduced from [80] with friendly permission from the Optical Society of America, © 2009 OSA.

6.3. Waveguiding

The dielectric waveguides of the microfluidic chips are intended to be used for excitation and detection of single molecules in the fluid channel. In the first set of experiments, light will be coupled into the waveguides to test the excitation of molecules in the channel at high concentration and to ensure that excitation of molecules is only taking place in the volume that is illuminated by the outcoupled waveguide mode.

In-coupling of laser light Coupling the light from the diode laser of the experimental setup into the on-chip waveguides is done using the same principle as in the fiber-based setup, by focusing the laser light onto the waveguide with an aspheric lens of suitable focal length (f=12 mm-f=20 mm, depending on chip and waveguide). To ensure accurate positioning of the waveguides relative to the focal spot of the lens, the chip is placed on a micrometer stage allowing for positioning and rotation of the chip. Another lens is placed on the opposite side of the chip, creating an far-field image of the outcoupled waveguide mode that allows to monitor the transmitted power with a power meter. At the intersection between the fluid channel and the waveguides, additional coupling losses are expected between the outcoupled mode in the fluid channel and the second part of the waveguide, depending on the refractive index of the medium in the channel. The measured outcoupled power behind the chip is therefore lower than the outcoupled power in the fluid channel. Since not all waveguides are fully functional after fabrication, transmission and incoupling efficiency vary between the

different waveguides. Therefore every waveguide has been tested by the group in Milan after fabrication. The testing protocols can be found in appendix C.

Raster-scanned images To image the volume illuminated by the out-coupled waveguide mode, images have been recorded by raster-scanning an optical fiber (FS-SN-3224, 3M, USA) in close proximity over the chip and measuring the outcoupled signal (compare figure 6.3a). To this end, one end of the fiber has been placed in a positioning system (T-LS 28M, Zaber Technologies Inc.) that can be controlled by the PC via serial port. A custom-made Labview software ("ZaberScan") is used to drive the positioner. The other end of the fiber is connected to the standard single molecule detection setup such that a fluorescence signal from the fluid channel will be coupled into the fiber and detected by the APD. The software will then record and save the signal at each position, resulting in a 2D map of the scanned area.

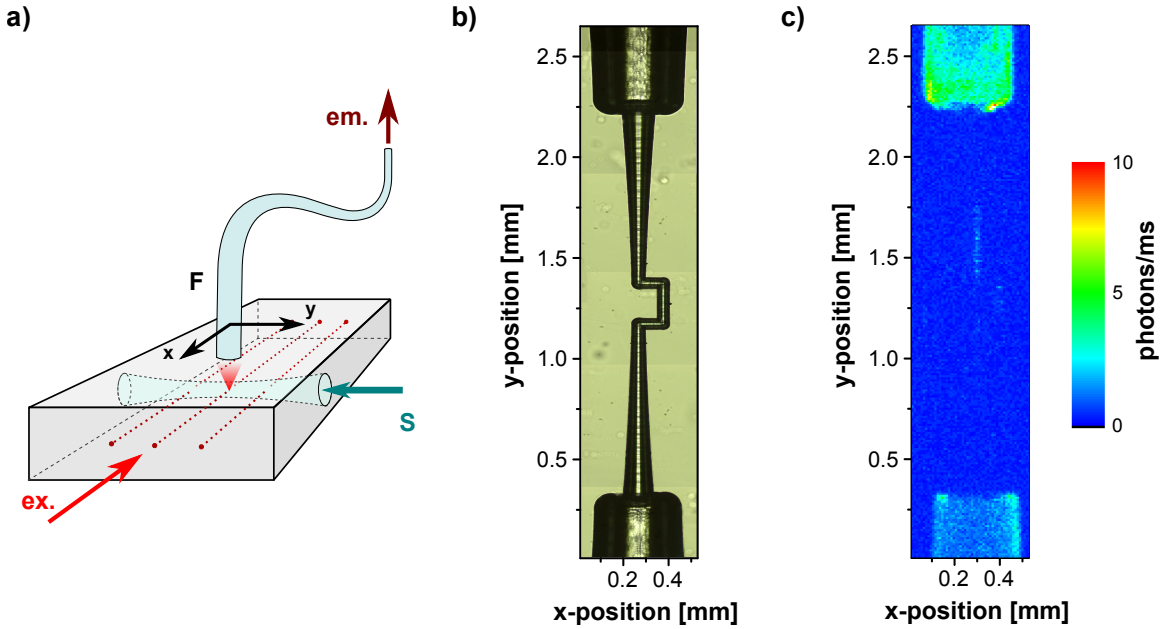

Figure 6.3.: **a)** Configuration for raster-scanning the microfluidic chips with an optical fiber (F). The sample (S) is pumped into the fluid channel and excited via the integrated waveguides (red dotted lines). Emission is collected by the fiber and measured with an APD. **b)** Microscope image of the fluid channel of the chip "ZigZag" (total length of channel ∼2 mm) with parts of the connections for tubing at the top and bottom. **c)** Image obtained from raster-scanning the fiber over the same area of the microfluidic chip. The channel was filled with pure water and the 690 nm laser was coupled into one of the waveguides. Image resolution 10 µm. The bright parts at top and bottom are autofluorescence from the connection between chip and tubing. In the middle part, the fluid channel is faintly visible, but otherwise no fluorescence signal can be recorded.

A microscope picture of the $\sim 0.5 \times 2.5$ mm large area around the fluid channel of the chip "ZigZag" and the scanned image of the same area is shown in figure 6.3b and 6.3c respectively. For this scan, 690 nm light from the laser diode has been incoupled into one of the waveguides of the chip and the channel has been filled with pure water. Therefore any collected photons will be due to scattering or autofluorescence. The connections between the channel and the tubing are shining up brightly, presumably due to autofluorescence from the glue used in the connection. The comparatively large diameter of the connectors also results in a reduced distance between those parts and the fiber, further enhancing the signal measured at the corresponding positions. In the central part of the image, a faint signal from the channel is visible. The parts shining up are those closest to the waveguide used in the experiment. Overall there is no unwanted strong source of fluorescence visible that would impede molecular fluorescence detection experiments

In the next step, waveguiding and specific excitation of dye molecules in the fluid channel have been tested. To this end, the channel has then been filled with 1 nM solution of Cy7 in PBS and the fiber has been scanned over the central part of the chip, where the waveguides reach towards the channel. The chip "ZigZag" contains a total of five waveguides, two framing the central u-shaped channel part (waveguides 1 and 5), one at each "bend" of the channel (2 and 4) and one in the central part (3), respectively (see appendix C for additional microscope images of the chip). Only the three central waveguides show sufficient waveguiding. The two outer waveguides have not been used in this work. Picture **a)** in fig. 6.4 is showing the recorded image after coupling light into waveguide 2, the waveguide at the top bend. The entire length of the channel at this point is lighting up. In picture **b)**, the laser has been coupled into the middle waveguide (3). Again, fluorescence emission from the channel is clearly visible. Note that the illuminated part of the channel has a total length of $\approx$ 160 µm in **a)**, but only $\approx$40 µm in **b)**, yielding an illuminated volume of $\approx$12 pL and 3 pL. In comparison no fluorescence emission could be measured from the channel after moving the chip downwards by a few micrometers, therefore not coupling the laser into a waveguide anymore (**c)**).

6.4. Single Molecule Detection Experiments

Detection of single molecules inside the microfluidic chips is performed in three different configurations. The first configuration is using a microscope objective to detect fluorescence photons from analyte molecules, while the molecules can be excited through the objective or the integrated waveguides (see figure 6.5a). The second configuration fully resorts to the integrated waveguides for excitation and detection of molecules (see figure 6.5b). And finally, an optical fiber is employed to detect molecules that have been excited with the integrated waveguides, analogous to figure 6.3a.

SMD with an objective The most straightforward SMD experiments in the chips can be performed by using a microscope objective for the detection of fluorophores con-

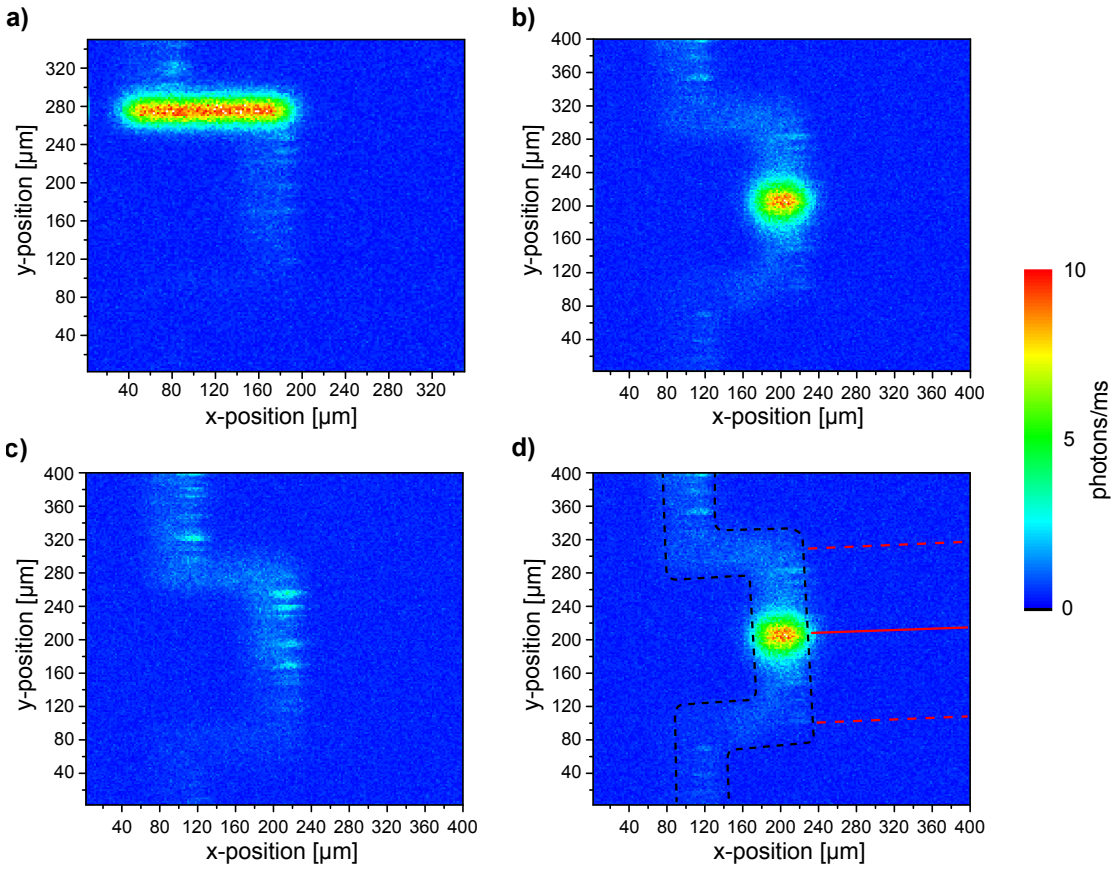

Figure 6.4.: Images obtained from raster-scanning the fiber over the microfluidic chip ("ZigZag"). The chip was filled with 1 nM solution of Cy7 and the 690 nm laser was coupled into the upper (**a**), central (**b**) and no (**c**) waveguide, respectively. Image resolution 2 µm. The channel is faintly visible due to scattered light and fluorescence from the dye. Only the parts of the channel illuminated by the waveguides light up, showing effective waveguiding. An overlay outlining the channel shape (black dashes) and position of the waveguides (red) is added in **d**).

tained in the sample inside the fluid channel of the chips (see figure 6.5a). Experiments have been performed in two main configurations, first by simultaneously exciting and detecting the molecules with the objective and later by exciting the molecules with the internal waveguides of the chip, while using the objective only for detection of the molecules. To implement the chip into the existing setup, a custom fixture has been created to place the chip upright in front of the objective, thus allowing control of the position of the chip by means of a 3-axis micrometer screw (see appendix A, figure A.2). For this experiments, the chip "ZigZag" was used. In the first configuration, the the laser beam is directed towards the objective by a flip mirror. Thus, the molecules are excited through the objective lens. In this way, single dye molecules could be detected easily inside the channel, although the overall efficiency was lower than in

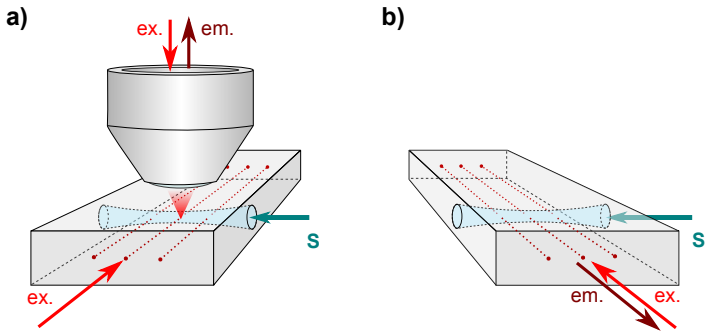

Figure 6.5.: Configurations used for single molecule detection experiments in the microfluidic chips and schematic design of the chips. The channel (light blue) is intersecting the waveguides (red dotted line), dividing them into two parts. **a)** Using an alternative detection scheme (pictured: microscope objective), while exciting through internal waveguides. In this configuration the objective can alternatively be used for simultaneous excitation and detection or be replaced by an optical fiber. **b)** Internal waveguides (red dots) used for excitation and detection of fluorescent molecules in the sample **(S)** inside the fluid channel.

objective-based experiments in the standard sample vessel (the SNR was about half the SNR of previous measurements with the same microscope objective). This is likely due to surface roughness of the fluid channel and non-optimal thickness (in respect to the design case of the objective optic) of the wall separating chip surface and fluid channel. A short time trace from a respective SMD experiment (10pM Cy7 dye in buffer solution, diffusion) is depicted in figure 6.6a.

Having established the possibility of SMD inside the fluid channel, in the next step the excitation path is switched from the objective to one of the internal waveguides of the chip. Some care has to be taken when in-coupling the laser into the on-chip waveguides and aligning the objective with the illuminated waveguide. As seen in chapter 5.2, the power density by the out-coupled waveguide mode will decrease quickly with increasing distance from the waveguide. Therefore it is advisable to position the objective focus close to the waveguide's end facet. If the focus of the objective was placed inside the out-coupled waveguide mode, characteristic fluorescence bursts from dye molecules could be recorded (see figure 6.6B). In comparison to the previous set of measurements, the overall number of detected photons per molecule was lower when using the on-chip waveguides. The likely explanation for the lowered efficiency is a combination of comparatively low power density in the out-coupled waveguide mode and further increased deviations in the PSF of the objective caused by having to focus deeper into the fluid channel. Experiments that used the internal waveguides for excitation in general showed a reduced signal-to-noise ratio in comparison to the "pure" microscope objective measurements. Since the emission rate of fluorescence emission by molecules depends on the excitation power (cf. section 2.1), a power dependency of the recorded fluorescence signal was measured to examine the excitation of dye

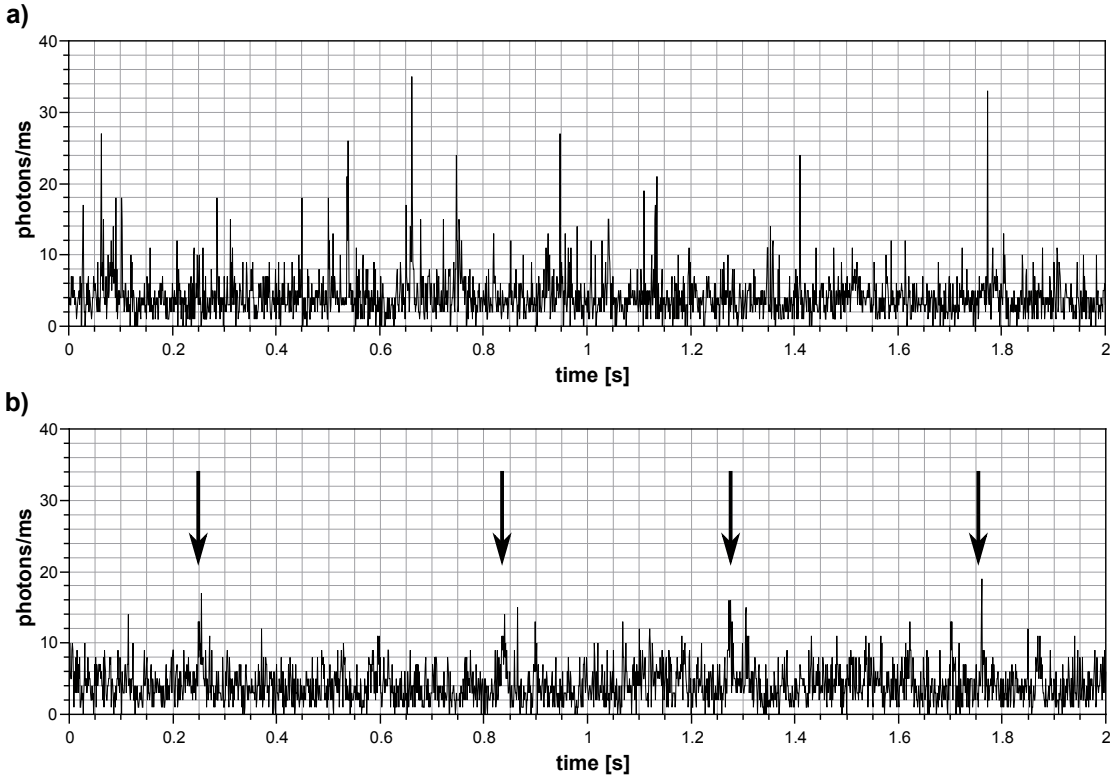

Figure 6.6.: Excerpts form characteristic time traces of diffusion-based single molecule detection experiments in the microfluidic chips. Sample concentration 10 pM Cy7. **a)** Objective used for simultaneous excitation and detection of fluorescent molecules in the sample. **b)** Using the internal waveguides for excitation of fluorescent molecules and the objective for detection. The red arrows indicate the position of four of the single molecule events.

molecules by the internal waveguides. The waveguide showing the best in-coupling efficiency was chosen and by using a filter wheel, the power of the diode laser was adjusted while the outcoupled power on the opposite side of the chip was measured. For six different values of outcoupled power, ranging from 0.15 mW to 3.5 mW, three sets of measurements have been performed and the histogram of each measurement was analyzed. To estimate the average number of detected fluorescence photons per bin (1 ms binning time), it was attempted to separate the distribution of background photons and fluorescence photons and to determine the difference between the mean value of both distributions. The resulting curve is plotted in figure 6.7. Since both distributions cannot be fully separated due to significant overlap, determining the exact value of the average photon emission per bin is difficult. Nevertheless it is clearly visible that the fluorescence emission was not saturated even for 3.5 mW. Since the power was measured at the out-coupled mode behind the chip, actual power in the first waveguide and fluid channel is expected to be even larger due to coupling losses to the second waveguide. In comparison to the single-mode fibers used in chapter 5.4,

where an outcoupled power of 2 mW was found to be on the onset of saturation for the dye molecules in the experiments, the mode-field diameter (MFD) of the on-chip waveguides is about 2× larger (8-9 µm vs. 4.5 µm). This resulted in an accordingly lower power density for the same incoupled power.

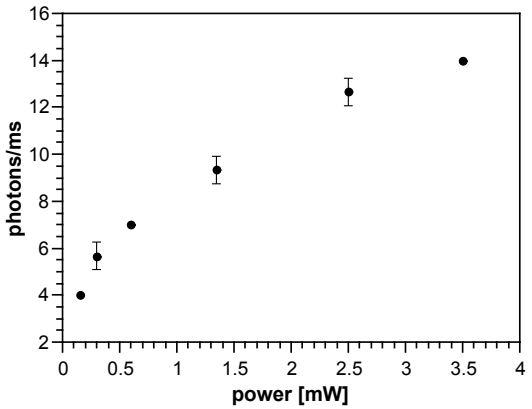

Figure 6.7.: Power dependence of fluorescence emission form single dye molecules in the microfluidic chip when excited by the internal waveguides. Even for 3.5 mW, the emission is not yet saturated.

While proof-of-principle SMD measurements have been successfully conducted using a microscope objective, nevertheless the setup and the microfluidic chips can still be optimized for improved detection efficiency. Choosing objectives with large working distance should improve the focusing into deeper parts of the fluid channel and the outcoupled waveguide mode. Alternatively the chip design could be reworked towards one better suited for efficient SMD with objectives, most prominently by taking the design parameters of the objective into account. Typical microscope objectives are designed for a fixed cover glass thickness (e.g. 170 µm), so a similar thickness for the chip walls would benefit experiments. Finally, the larger MFD of the internal waveguides necessitate higher amounts of power compared to the other experimental approaches. Depending on incoupling and detection efficiency, lasers with higher power output or waveguides with a lowered MFD might be necessary.

SMD with internal waveguide Undoubtedly great potential for optical SMD with microfluidic chips lies in fully integrated setups using internal waveguides for excitation and detection of fluorescent molecules. Such a setup would pave the way to compact, efficient and automated commercial applications. To test the applicability of the integrated waveguides, the microfluidic chips have been used in a configuration similar to the fiber-based setup. The laser is incoupled into one of the on-chip waveguides to excite fluorescent molecules inside the channel and simultaneously used to detect fluorescent light emitted by excited molecules. Typically the amount of background photons created in a dielectric waveguide from inelastic scattering processes scales linearly with waveguide length. Due to the short length of the on-chip waveguides

(typically 3-10 mm, depending on waveguide and chip), naively a very low background count-rate is to be expected in chip measurements, which would be beneficial to any SMD experiment. However, actual measurements show a much larger background in comparison to equally sized optical fibers. Background count rates originating from on-chip waveguides exhibit one to two orders of magnitude larger background rates per unit length. This results in the same or higher background as in SMD experiments conducted with the fiber sensor, which is typically employing a 20-30 cm piece of optical fiber. The origin of the comparably high background remains unclear due to open questions yet surrounding fabrication and mechanism of dielectric on-chip waveguides, but impurities and color centers created during the waveguide fabrication are suspected to play an important role.

For the purpose of SMD through the on-chip waveguides, Cy7 diluted to concentrations ranging from 5 pM to 5 nM in the custom buffer (B) has been pumped into the chips "single", "carpet" and "squeeze", and different flow rates have been applied through hydrostatic pressure. No single molecule events could be recorded during the experiments. While exceptionally high analyte concentration in the nanomolar range or very large flow rates affected the background count rate, the experiments did not result in discernible single-molecule events. It is suspected that this is caused by the inefficient excitation and consequently incoupling. Due to the high background count-rate generally the laser power incoupled into the waveguides had to be reduced, resulting in lowered emission from the dye molecules (cf. 2.1). At the same time, the intensity distribution of the outcoupled waveguide mode inside the fluid channel remains unclear. Surface roughness from the etching process and inherent faults in the waveguide can contribute to an overall lowered incoupling of fluorescence photons into the waveguide mode. Many waveguides exhibit concave conical features at the intersection with the fluid channel, caused by slight etching into the waveguides during the microchannel fabrication. With the exception of a very narrow region directly at the waveguide-facet, simulations of similarly modified waveguides show a drastically lowered out-coupled intensity in the important region close to the end facet, which translates into similarly reduced incoupling into the waveguide mode (see figure 6.8). The intensity distribution at larger distances remains largely unchanged.

SMD through an optical fiber As the integrated waveguides have proven inefficient at detecting single molecules, a different detection scheme has to be employed. But while microscope objectives are an relatively easy and efficient way to detect single molecules inside the chips, they do result in comparably bulky optics. Optical fibers on the other hand would allow for easier realization of compact setups. The viability of SMD by an optical fiber has been shown in chapter 5. With the position of the fluid channel determined by the raster-scanning experiments, the fiber was placed on top of the illuminated channel segment and a time trace was recorded at concentrations of 10 pL and below to ensure the measurement takes place in the single molecule regime. Binning frequencies of 10 kHz ($\widehat{=}$0.1 ms binning time) and 1 kHz ($\widehat{=}$1 ms) have been used while recording the time traces. No single molecule events could be recorded

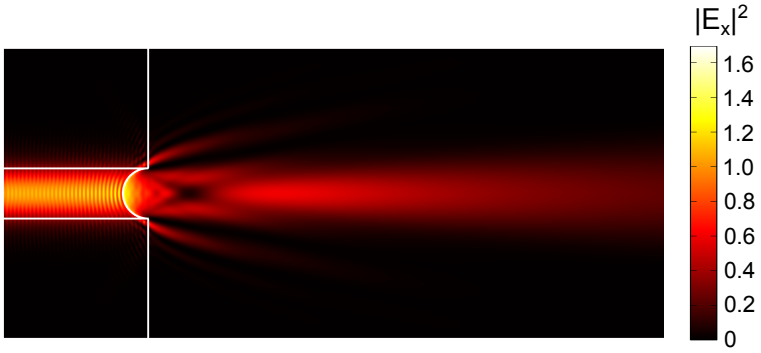

Figure 6.8.: Simulated intensity distribution behind a waveguide modified with an concave half-sphere, resembling a partially-etched waveguide in microfluidic chips. With the exception of a very narrow region directly at the waveguide-facet, the outcoupled intensity close to the waveguide is noticeably lower in comparison to an unmodified waveguide.

during the measurements. The likely explanation is the low incoupling efficiency of the low-NA single-mode fibers for large fiber-emitter distances (cf. chapter 5.3.1) - the fluid channel of the microfluidic chips is typically found in a depth of >100 µm. To counter the problems of using single mode fibers at large emitter-fiber distances, a batch of new chips has been designed and manufactured that has the fluid channel "bend" upwards in the central part of the chip, thus reducing the distance between emitter and fiber to ∼30 µm(see chip "CHMOD.04 ch.B" in appendix C). The distance between the waveguides and the chip surface likewise had to be reduced. In the experiments the displaced waveguides proved difficult to handle and the coupling efficiency between the laser and the waveguide mode was found to be significantly lower. Consequently the light intensity in the channel was lower compared to the unmodified chips. With further reduction of power available for the excitation of molecules, again no single-molecule events could be detected, despite the promising design.

Adjusting the flow rate in the fluid channel The effect of flow on single molecule measurements has been covered in chapter 4, where it has been shown that the number of detected single molecule events can vary greatly with flow rate. Flow can be induced in the channel of the microfluidic chips in two ways. Either by pumping the sample solution into the channel with a syringe connected to the tubing or through hydrostatic pressure applied to the channel by creating an vertical offset Δz between the two sample reservoirs. Qualitatively the influence of flow can be visualized by adjusting the offset between the two reservoirs during a measurement. The time trace from one measurement is shown in figure 6.9. As the flow rate is increased and decreased again by lowering and raising one reservoir during the measurement, the density and height of fluorescence peaks as well as the background changes. For a more quantitative approach, a series of experiments was performed where the offset between the reservoirs was increased by a micrometer screw in discrete steps. However the relation

between flow and offset of the reservoirs has proven to be erratic. Analyzing the time traces by means of autocorrelation and FCS models shows that even when there is no offset applied to the sample reservoirs, (slow) sample flow was present in the fluid channel during some measurements. Several recorded time traces of the experiments conducted at large Δz/high flow rates have also shown fluctuations of background and peak frequency on a timescale of a few seconds, resulting in correlation curves that exhibit more than one decay constant. It is likely that this fluctuations are an accompanying effect of irregular, changing flow rates in the sample channel during the measurements. At the time the experiments have been done, a full theory of SMD in flow had not yet been developed and no independent method for calibration of the flow rate was available. It was therefore not possible to conduct reliable and reproducible measurements showing the influence of the flow rate. Instead care was taken to minimize the flow in the channel and experiments were restricted to diffusional transport.

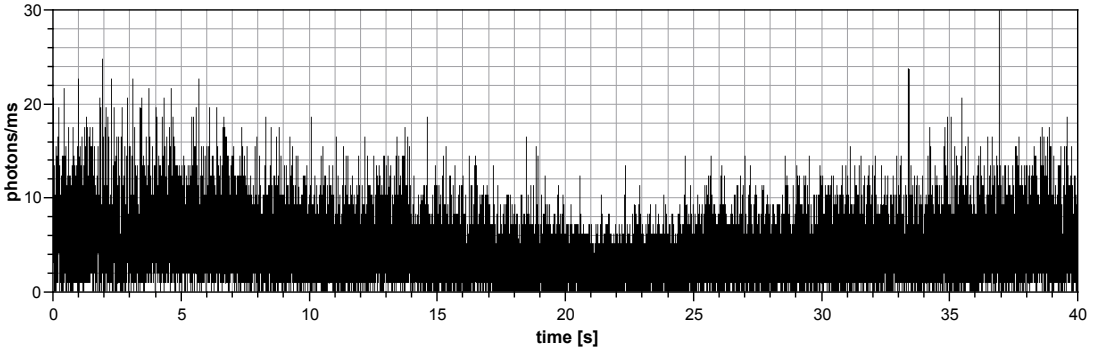

Figure 6.9.: Experimental time trace showing the effect from varying the vertical offset between the two sample reservoirs of the microfluidic chip. The flow rate is first slowly increased until it reaches a maximum around 20 s and is subsequently reduced again. With changing flow rate, the number of molecules as well as the background count rate is affected. In this measurement the dye molecules have been excited by the internal waveguides, while the objective was used for detection. Sample concentration was 10 pM.

6.5. ROXS Buffer Experiments

Common fluorescent dyes as those used in this thesis often exhibit distinct dark states (blinking) and are prone to photobleaching when excited for extended periods of time with high intensity. A dye molecule in the dark triplet state T_1 can return to the singlet state by quenching with molecular oxygen, a process which can lead to the creation of reactive singlet oxygen. The involvement of singlet oxygen in chemical reactions that can lead to the destruction of the dye molecule make it an undesired byproduct.

Removal of oxygen from the sample can prevent destruction of the dye molecule, but at the same lead to increased triplet state lifetime [82], reducing the brightness of the dye molecule and increasing the probability for further chemical reactions from the triplet state. As a potential method to increase photostability and reduce blinking in organic dyes, an alternative buffer containing a reducing and oxidizing system (ROXS) [83] has been tested for its potential use in single molecule detection experiments. The working principle of the ROXS buffer is based on simultaneous application of reducing and oxidizing agents (ascorbic acid and methylviologen) that can quickly recover triplet and ionized states of the dye molecule in combination with an oxygen scavenging system (glucose and enzymatic oxygen scavenger) to remove molecular oxygen from the buffer solution. The buffer recipe can be found in appendix B. The ROXS buffer has been kindly provided by the group of Markus Sauer (Lehrstuhl für Biotechnologie und Biophysik, Biozentrum, University of Würzburg)

To test the effect of the ROXS buffer on single-molecule measurements, experiments where conducted in the microfluidic chip. The necessity to remove oxygen from the sample when using the ROXS buffer makes the chips well-suited for these experiments, since they can effectively seal-off the sample from surrounding air during even extended measurements, thus preventing the re-absorption of oxygen from the environment. For the experiments, Cy7 has been diluted to 5pM both in standard PBS buffer and ROXS buffer, which has then been pumped into the microfluidic chip. To maximize the potential residence time of the analyte molecules in the detection volume, the flow rate in the chip has been minimized by putting the sample reservoirs at equal height after the sample has been pumped in. To prevent photobleaching from affecting the count rate, the sample flow is shortly increased at regular intervals between measurements, such that depleted sample volume is replaced. All experiments have been carried out with the microscope objective (NA 0.85, Leica) used to both excite and detect the molecules, while the internal waveguides of the chips have not been used. Using the peak detection algorithm to analyze the recorded time traces (5 allowed wrong positives), the PBS sample resulted in an average number of 1730±160 detected molecules per 60 s. In the same time span, the ROXS sample lead to the detection of 1930±230 molecules on average. At first glance, the difference between the two buffers seems to be rather small, with only a slight advantage in using the ROXS buffer. However, looking closer at the recorded time traces paints a somewhat different picture. Comparing the histograms of a representative PBS and ROXS measurement (see figure 6.10 A), the histogram from the ROXS experiment is showing a significantly larger "tail" from fluorescence photons compared to the PBS measurement. This is a first hint that the ROXS buffer is leading to wider fluorescence peaks in the time traces - an assumption that is confirmed by directly looking at the time traces from the measurements. The increased photostability and decreased blinking of the dye molecules in the ROXS buffer enables the molecules to emit photons for a longer time while in the objective's focus without entering a dark state or bleaching. Calculating the autocorrelation of PBS and ROXS measurements confirms the increased width of fluorescence bursts (figure 6.10 B). While the PBS sample results in a time constant τ_D of $\approx 300\mu s$, the resulting time constant in the ROXS buffer is $\approx$ 1ms, i.e. three

times longer. This explains the previous observations: the ROXS buffer does not lead to the detection of significantly more molecules, since the objective-based setup is able to efficiently detect the molecules in the PBS sample as well, but the molecules survive for longer time in a bright state. The slight increase in detected molecules with the ROXS buffer can be explained by the enhanced maximum emission rate and photostability of the dye molecules observed in the experiments, which will increase the probability of successfully detecting a molecule over the random background noise.

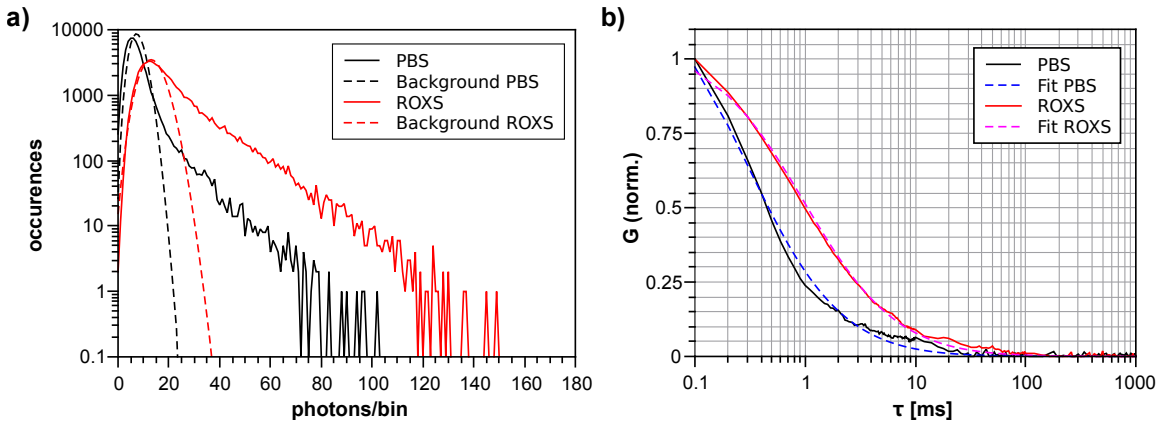

Figure 6.10.: Comparison between measurements in PBS buffer and in the special ROXS buffer, conducted in the microfluidic chip: **a)** Representative histograms of PBS and ROXS experiments. ROXS buffer leads both to higher maximum emission and to more bins containing fluorescence photons. **b)** Autocorrelation of diffusion-based experiments. ROXS buffer is resulting in a significantly larger value for τ_D ($\approx$ 1 ms) in comparison to PBS ($\tau_D \approx 0.3$ ms).

In conclusion the ROXS buffer is able to significantly enhance the emission properties and photostability of the dye used in the experiments. At the same time this effect is not translated into a significantly increased number of detected molecules in the experiments described earlier. For the objective-based setup, which is already offering a very good detection efficiency, the ROXS buffer does therefore not offer an obvious advantage. Given the more complicated sample preparation procedure for the ROXS, the standard PBS buffer is the more practical alternative for such experiments. However, the ROXS buffer can be a useful asset in detection schemes that possess comparatively low detection efficiency and consequently react more favorably to increased photostability and emission rate. A good example would be waveguide-based detection schemes as discussed in this thesis. The low-oxygen requirement of the ROXS buffer prevent its application in the fiber-based sensor setup, as the rapid stirring and unfavorable volume-surface ratio of the sample lead to a fast re-absorption of environmental oxygen. A fully encapsulated fiber setup or submersion in a nitrogen atmosphere could solve this problem at the expense of experimental complexity. On the other hand fully

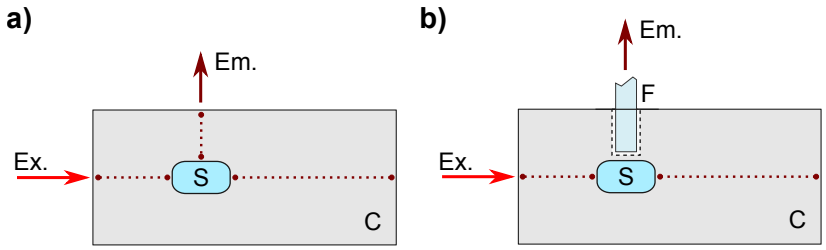

Figure 6.11.: Proposed alternative design towards a microfluidic chip (C) in a fully integrated SMD setup. **a)** Additional waveguides on top of the fluid channel containing the sample (S), for the collection of fluorescence emission, placed perpendicular to the waveguides (red dotted line) used for excitation. **b)** Small holes are created over the channel, reducing the wall thickness. On-chip waveguides are used for excitation. An optical fiber (F) is placed in the hole to collect the fluorescence emission.

integrated detection schemes based on microfluidic chips could benefit greatly from the ROXS buffer, if chips with efficient waveguides can be successfully created.

6.6. Conclusions

Microfluidic chips with integrated dielectric waveguides are very interesting as a basis for LOC systems aiming at optical detection of molecules or cells. In the experiments conducted for this thesis the possibility of using the integrated waveguides to excite fluorescent molecules was shown. Single dye molecules could be successfully detected inside the fluid channel by use of a microscope objective while exciting them through the internal waveguides. However, the ultimate goal of the experiments, simultaneous excitation and detection through the integrated waveguides or detection through an additional optical fiber placed on the chips could not be realized. The problems encountered during the work with the microfluidic chips fall into two categories, namely issues with design and fabrication (placement and properties of the waveguides) and experimental issues (adjusting the flow reliably, incoupling into the waveguides). During the work with the chips it became apparent that some improvements to the design would be necessary to support SMD by waveguides in the microfluidic chips. A first step was taken with the second generation of chips ("SMOD.04 ch.B") that reduced the distance between fluid channel and chip surface, allowing to place an optical fiber much closer to the fluid channel and analyte molecules, but unfortunately these chips proofed difficult to work with due to complicated coupling between laser and on-chip waveguides.

Another idea for an improved design is shown in figure 6.11. Here, additional waveguides placed perpendicular to the original waveguides would allow for efficient excitation at high intensity while keeping a low background count-rate in the detection channel due to the 90° geometry. As such chips have so far proven difficult to create

(writing the vertical waveguide makes it necessary to constantly adjust the adaptive writing optics to the changing focusing depth), in a simpler realization, a hole is drilled above the channel, potentially by the same technique as used in the microchannel production. Finally, an optical fiber is placed into the hole and fixed in place by using glue of appropriate refractive index. As the fiber is now situated closer to the emitters, the incoupling efficiency should increase significantly, while eliminating the need for waveguides close to the chip surface, which was responsible for the difficult coupling in the second generation of chips.

The ROXS buffer studied earlier approaches the problem from a different angle. Here, the efficiency of the emitters is enhanced. The low-oxygen requirement of the ROXS buffer makes it predestined to be used in a sealed-off environment as provided by the chips. It remains to be seen whether waveguide-based single molecule detection in the microfluidic chips can be realized by a combining improved chip designs with enhanced emission provided by the ROXS buffer.

7. Summary and Outlook

In this thesis, fluorescence-based single molecule detection at low concentrations has been investigated. The usual suspect for the efficiency of an optical single molecule experiment is the photon detection efficiency of the setup, i.e. the fraction of emitted fluorescence photons that can ultimately be detected. But provided that the photon detection efficiency is sufficient, another major practical limitation for single molecule experiments can be identified in the concentration of analyte molecules. At a low concentration of analyte molecules (below fM), the time between the successive arrival of two emitters can quickly escalate to several hours and beyond if the transport of analyte molecules is solely provided by diffusion. Consequently an efficient detection of single molecules within reasonable timeframes cannot be ensured in absence of a form of active transport.

The first topic of this thesis (chapter 4), is therefore the influence of flow on SMD experiments. By providing a steady laminar sample flow, the amount of sampled volume per time can be significantly increased. However, the reduced residence time in the detection volume of the setup will simultaneously reduce the number of detected photons. In experiments a characteristic behavior was observed under such conditions, with a distinct maximum number of detected molecules appearing at medium flow rates of a few mm/s. Additional Monte-Carlo simulations of an SMD experiment in laminar flow reproduced the experimental findings. An analytical model, which is based on basic experimental parameters, has been derived that can predict the number of detected molecules as a function of sample flow rate. The model has proven to closely resemble the experimental results and was used to fit experimental data at different flow rates. With help of the analytic model it is also possible to probe local flow by means of SMD experiments. As a first demonstration, the influence exerted by a small microstructure on surface flow has been measured. This approach is of interest to the development of microfluidic devices by offering a simple method to investigate the flow characteristics in such devices.

As the second topic of this work (chapter 5), the suitability of dielectric single-mode waveguides for single-emitter detection has been investigated. While the photon detection efficiency of such waveguides is low in comparison to typical microscope objectives, they offer great advantages in other areas. The promise of compact and cheap assays by using small and flexible or integrated waveguides cannot be denied. Here a method has been presented that can be used to analyze emission and photon detection characteristics of arbitrary waveguides. The analytical results and FDTD simulations have been experimentally confirmed by measuring the incoupling of quantum dot emission into an optical fiber at different distances. The methodology can also be applied to optimize specific emission and detection characteristics of waveguides in respect to ex-

perimental requirements. By simple modifications to the end facet, it has been shown that it is possible to enhance incoupling efficiency by one order of magnitude and create a more focused detection volume, which can be advantageous for high concentration single molecule experiments. As a first realization of waveguide-based sensors, a setup based on a commercially available optical fiber is presented. It was found to efficiently detect single molecules down into the attomolar concentration regime. Such a sensor can be of great use e.g. in diagnostic cases where biomarkers are usually present in very low concentration, such as early-onset disease diagnosis. To reliably measure such a low analyte concentration, a small rotor is used to stir the sample volume. Interestingly this setup was found to work efficiently at high flow rates, where turbulent flow is encountered. This is in contrast to the relatively modest laminar flow encountered in the previous part. Obviously there are distinct differences between the low-Reynolds number laminar flow of chapter 4 and the high-Reynolds number turbulent flow present in the experiments with the fiber sensor. Notably, autocorrelation analysis strongly suggests the involvement of vortices which appear at high flow rates at the tip of the optic fiber. While the turbulent flow is more difficult to handle, the high volume throughput in combination with the creation of small vortexes that can trap molecules in the detection volume offer an promising option for highly sensitive SMD sensors without the need for comparatively elaborate experimental setups.

Finally, in the last part of the thesis (chapter 6), by combining waveguides and microfluidics, the approaches of the previous chapters are brought together and an integrated and compact SMD experiment has been investigated. Small chips made of fused silica, with microfluidic channels and integrated dielectric waveguides have been used to perform different SMD experiments. The possibility of SMD in such chips was successfully shown. The integrated waveguides could be used for excitation of dye molecules, which were then detected through a microscope objective. However, it was not yet possible to detect single molecules using only the internal waveguides, which were limited by an unusually high background count rate and low incoupling of fluorescence emission. A better understanding of the waveguide formation process is necessary to improve the waveguides and reduce the contribution of background photons. Another reason was found to lie in the design of the chip's layout. Taking the findings from chapter 5 regarding the spatial distribution of the detection efficiency of waveguides into account, several improvements to the design of the chips could be proposed that should aid their implementation in future SMD experiments. During the experiments with the chips, the influence of an alternative buffer containing a reducing and oxidizing system (ROXS) was tested. While this buffer's low-oxygen requirement limits its use in the experiments presented in the earlier chapters of this work, the microfluidic chips are exceptionally suitable for such experiments due to providing an experimental environment sealed off from the surrounding atmosphere. The buffer was found to considerably reduce dark states and improve emission rate and should proof beneficial in particular in detection schemes with a low signal-to-noise ratio.

Detection of single emitters, especially at ultra-low emitter concentration remains a topic of high interest to ongoing research. With the advent of lab-on-a-chip tech-

nology the need for compact and efficient schemes capable of detecting single emitters has increased. This work aims to contribute to the progress towards this goal by investigating solutions to two major obstacles encountered on the road towards the realization of a powerful, cheap and easy-to-use sensor based on a "lab-on-a-chip". Incorporating the findings of this work into the creation of future lab-on-a-chip designs, by combining active transport through flow and efficient detection through dielectric waveguides, offers an exciting outlook for the future of single molecule detection.

8. Zusammenfassung und Ausblick

In den vergangenen 25 Jahren haben die Entwicklung von neuartigen fluoreszenten Farbstoffen, sowie von erschwinglichen und empfindlichen Instrumenten, zu einer rapiden Entwicklung von optischen Einzelmolekültechniken geführt. Einzelmolekülfluoreszenztechniken bieten eine hervorragende Empfindlichkeit und die Möglichkeit, Verhalten zu untersuchen, das in herkömmlichen Ensemble-Messungen anderenfalls verborgen bliebe. Gerade im Bereich der Biophysik haben sie sich zu einer der einflussreichsten Einzelmolekülmethoden entwickelt.

Einzelmolekülfluoreszenz bildet die Grundlage für hochempfindliche Methoden zur Detektion von Biomolekülen, wie DNS oder Proteinen. Mit fluoreszenten Marker-Molekülen, etwa den sogenannten „molecular beacons“, ist es mit Einzelmoleküldetektion möglich, Genexpression, spezifische Antigene oder Krankheits-Marker zu beobachten.

Allerdings gibt es dabei in der praktischen Anwendung von Einzelmolekülmethoden Einschränkungen. So ist die Konzentration der untersuchten Farbstoffmoleküle auf einen Bereich zwischen einigen hundert Femtomol und einigen Nanomol pro Liter beschränkt. Die obere Grenze ergibt sich direkt aus der Notwendigkeit sicherzustellen, dass sich während einer Einzelmolekülmessung durchschnittlich weniger als ein Molekül im Beobachtungsvolumen aufhält. Niedrige Konzentrationen können auf der anderen Seite dazu führen, dass die Zeitdauer, die im Mittel zwischen zwei aufeinanderfolgenden Moleküldetektionen vergeht, stark zunimmt und einige Stunden und mehr betragen kann. Die Ursache hierfür ist, dass Diffusion als Transportprozess bei niedriger Molekülkonzentration sehr ineffizient ist. In solchen Fällen wird offenbar ein alternativer Transportprozess benötigt.

Die Arbeit betrachtet zunächst den Einsatz von laminarer Strömung in Experimenten zur Einzelmoleküldetektion. Durch die Strömung wird ein ausreichender Volumentransport gewährleistet, der es ermöglicht, die Menge an messbarem Probenvolumen pro Zeit deutlich zu erhöhen. So kann die Limitierung, die diffusionsbasierte Messungen bezüglich der minimal zugänglichen Konzentration aufweisen, umgangen werden. Während der von einer Strömung getragene Volumentransport die Menge an Molekülen, die das Detektionsvolumen pro Zeiteinheit durchqueren, erhöht, wird allerdings zugleich die Verweildauer im Detektionsvolumen verringert. Dadurch nimmt die Menge an messbaren Fluoreszenzphotonen ab, so dass eine Detektion wieder erschwert wird. Im Rahmen der Arbeit wurde ein theoretisches Modell entwickelt, das dass zu erwartende Verhalten einer Einzelmolekülmessung in Abhängigkeit der Strömungsgeschwindigkeit vorhersagen kann. Das Modell konnte sowohl durch Monte-Carlo-Simulationen gestützt, als auch experimentell bestätigt werden. Es zeigte sich ein klares Maximum in der Menge an detektierten Molekülen bei Strömungsgeschwindigkeiten von eini-

gen mm/s. Gegenüber diffusionsbasierten Messungen können so mehr Moleküle gemessen werden. Allerdings kann die Strömungsgeschwindigkeit, und damit der Volumendurchsatz, nicht beliebig erhöht werden, ohne schließlich wieder eine Abnahme der detektierten Moleküle zu bewirken. Die optimalen Messbedingungen können mittels des entwickelten Modells vorhergesagt werden. Mit Hilfe des analytischen Modells ist es zudem möglich, lokale Strömungsverhältnisse mittels Einzelmolekülmessungen zu untersuchen. Als eine erste Demonstration wurde der Einfluss von kleinen Mikrostrukturen auf die lokalen Oberflächenströmung gemessen. Ein solcher Ansatz bietet eine einfache Möglichkeit, um die Strömungsverhältnisse in mikrofluiden Systemen zu untersuchen.

Als zweites Thema dieser Arbeit werden anschließend dielektrische Wellenleiter am Beispiel von single-mode Glasfasern und ihre Eignung zur Verwendung in Einzelmolekülexperimenten betrachtet. Gegenüber klassischen Versuchsaufbauten, die zum effizienten Nachweis der Fluoreszenzemission üblicherweise Mikroskopobjektive mit hoher numerischer Apertur (NA) verwenden, haben Wellenleiter eine geringe NA. Dadurch ist auch der Anteil der Fluoreszenzemission, der durch einen Wellenleiter detektiert werden kann, deutlich verringert. Allerdings bieten Wellenleiter auch einige potentielle Vorteile. So ermöglichen sie eine höhere Flexibilität für in-situ Messungen und können als Grundlage für hochintegrierte Optiken in kompakten Sensoren genutzt werden. Um die Charakteristika von Wellenleitern in einem Einzelmolekülexperiment besser zu verstehen, wurde ein theoretischer Ansatz auf Basis des Reziprozitätstheorems entwickelt. Damit wird es möglich, die Detektionseffizienz eines Wellenleiters, sowie deren räumliche Verteilung, zu berechnen. In Kombination mit numerischen Simulationen des aus einem Wellenleiter ausgekoppelten Strahlungsfeldes können somit beliebige Wellenleiter und ihr Verhalten in Einzelmolekülexperimenten untersucht werden. Die beschriebene Methode kann auch zur Optimierung von spezifischen Emissions- und Detektionseigenschaften von Wellenleitern genutzt werden. Durch eine einfache Modifikation der Endfläche des Wellenleiters konnte etwa gezeigt werden, dass sich die Einkopplungseffizienz um eine Größenordung steigern lässt und zugleich ein deutlich stärker fokussiertes Detektionsvolumen erzeugt wird. Die experimentelle Bestätigung der durch Theorie und Simulation erhaltenen Ergebnisse erfolgt, indem die durch eine Glasfaser detektierte Emission einzelner Quantenpunkte in Abhängigkeit des Abstandes zwischen Faser und Quantenpunkt gemessen wird. Schließlich wird eine experimentelle Realisation eines Einzelmolekülsensors auf Grundlage einer handelsüblichen single-mode Glasfaser gezeigt. Mit diesem Sensor ist es möglich, einzelne organische Farbstoffmoleküle bis in den attomolaren Bereich zu detektieren. Wie bereits im vorausgehenden Teil beschrieben, müssen die Farbstoffmoleküle bei derart niedriger Konzentration aktiv ins Detektionsvolumen befördert werden. Dies kann durch schnelles Durchmischen des Probenvolumens mit einem Rotor erreicht werden. Dabei entstehen turbulente Strömungsbedingungen im Probenvolumen, die sich von den zuvor beschriebenen laminaren Strömungen unterscheiden. Interessanterweise sind die entstehenden Turbulenzen eine entscheidende Voraussetzung für die erfolgreiche Detektion von einzelnen Molekülen mit dem faserbasierten Sensor. Während turbulente Strömungen schwieriger zu handhaben sind, bietet der hohe Volumendurchsatz in Verbindung mit

kleinen Wirbeln, die Moleküle im Detektionsvolumen „einfangen“, einen vielversprechenden Ansatz für hochempfindliche Einzelmolekülsensoren bei verhältnismäßig einfacher experimenteller Realisation.

Schließlich werden die Ansätze aus den vorangehenden Teilen im letzten thematischen Abschnitt in Form von Experimenten an kompakten Chips mit mikrofluiden Kanälen und integrierten Wellenleitern kombiniert. Derartige Chips, hergestellt aus Quarzglas, können die Basis eines zukünftigen Lab-on-a-chip Systems bieten. Ein wenige Mikrometer im Durchmesser betragender Kanal dient dem Transport der zu untersuchenden Probenflüssigkeit durch den Chip. Den Kanal überschneidende Wellenleiter werden zur Anregung und Detektion der im Kanal befindlichen Farbstoffmoleküle genutzt. In den durchgeführten Versuchen gelang es, erfolgreich Einzelmoleküldetektion im Kanal der Chips durchzuführen. Hierzu wurden die Moleküle zunächst durch ein externes Objektiv detektiert, aber durch die integrierten Wellenleiter angeregt. Im Gegensatz dazu konnten die integrierten Wellenleiter bisher nicht erfolgreich zur Detektion von Einzelmolekülen genutzt werden. Als Ursache werden u.a. Herstellungsfehler der integrierten Wellenleiter und Probleme mit dem Design der Chips diskutiert. Unter Einbeziehung der Erkentnisse aus dem vorherigen Teil, konnten mehrere Verbesserungsvorschläge gemacht werden, die dazu beitragen sollten, die Eigenschaften derartiger Chips bezüglich ihrer Eignung zur Einzelmoleküldetektion zu verbessern. Vollintegrierte Versuchsaufbauten für fluoreszenzbasierte Einzelmolekülsensoren rücken damit ein Stück näher.

Die Einzelmoleküldetektion, im Besonderen bei extrem niedriger Konzentration, ist nach wie vor ein wichtiges Thema in der aktuellen Forschung. Mit dem Aufkommen von „lab-on-a-chip“-Lösungen ist die Nachfrage nach kompakten und effizienten Verfahren zur Einzelmoleküldetektion weiter gestiegen. Diese Arbeit möchte zu diesem Ziel beitragen, indem Lösungsansätze für zwei der großen Hindernisse untersucht werden, die der Entwicklung von günstigen, effektiven und einfach zu handhabenden Sensoren entgegenstehen. Die Kombination von aktivem, strömungsbasierten Transport mit effizienter Detektion auf Basis von Wellenleitern bietet einen aufregenden Ausblick auf die Zukunft der Einzelmoleküldetektion.

Appendix A.

Experimental Setup and Protocols

A.1. Experimental Setups

A.1.1. Single Molecule Detection

Fiber-based Setup The experimental setup for fiber-based experiments is depicted in figure A.1. A semiconductor-diode-laser (**L**) emitting at 635 nm(IDT0-635-30, GMP, 30 mW) in case of experiments with FRET dye, or 690 nm (HL6738MG, Thorlabs, 30mW) for standard Cy7 dye is providing the excitation light. After passing through a filter wheel to control the power, the laser beam is deflected by a dichroic mirror (**1**, T740/140 650 dcip, Chroma) and coupled into a short (20 to 30 cm) piece of single-mode optical fiber (**F**, FS-SN-3224, λ_{cutoff}=630 nm, Thorlabs). Fibers have been chosen for low Raman background. The light is transmitted through the fiber and emitted via a 90^o-cleaved fiber end into the liquid sample volume **P**, where it excites single molecules whose fluorescence is coupled back into the fiber with sufficiently high efficiency. The fiber is connected to a computer controlled xyz positioner (I3005, Luminos Industries or T-LS 28M, Zaber Technologies Inc.) which allows for a precise positioning of the fiber relative to the rotor. Single-molecule fluorescence passes the dichroic mirror after exiting the fiber, while residual excitation light traveling backwards through the fiber or being reflected at the fiber end facet gets deflected. The remaining light passes a bandpass filter (**3**, BrightLine HC 785/62, Semrock) and is focused by a convex lens (**4**, f=30 cm, AC254-300-B, Thorlabs) onto the active area (ø=180 µm) of a single photon counting avalanche diode (**D**, SPCM-AQR-13, Perkin Elmer, quantum efficiency at 780 nm$\approx$ 60 %) whose output is fed into a PC and evaluated by counting fluorescence bursts in the fluorescence time traces using a custom-made software (Labview, National Instruments). The focal length of the focusing lens has been chosen such that the image of the fiber core fits the active area of the detector thus preventing excess background originating from cladding modes from reaching the detector's active area.

Objective-based setup For objective-based single-molecule detection experiments, the setup described in the previous paragraph has been slightly modified. The fiber has been removed and replaced by a microscope objective (NA=0,85, Leica), mounted on a 3-axis fiber launch system (MBT610/M, Thorlabs) to allow for alignment of the objective with the beam path. The sample container is placed on a xyz-micrometer stage (New Focus) for position control. Compared to the fiber-based experiments, the

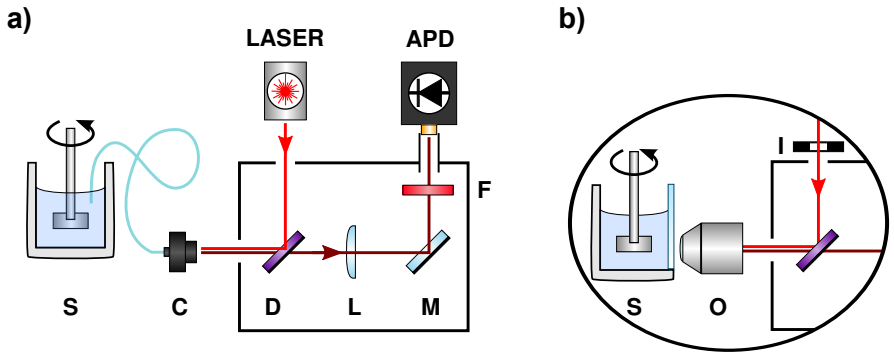

Figure A.1.: Schematic diagram of the experimental setup. **a)** Fiber-based setup. Laser: red diode laser, D: dichroic mirror, C: fiber coupler including aspheric lens, with a short piece of single-mode optical fiber (20-30 cm), S: sample container (ø=10 mm,V=1 ml), F: bandpass filter, L: focusing lens, APD: single-photon counting avalanche photodiode module, M: mirror. **b)** Objective-based setup. O: microscope objective, I: iris to adjust beam-size. To shield the setup against ambient light, most of the beam-path is placed in a box.

sample container has been modified by removing part of the outer wall and inserting a standard microscope cover slip (25x25 mm, 0,17 mm thickness) to allow focusing into the sample volume from the outside (see figure A.2B). Additionally excitation light is provided by incoupling the laser into a single-mode optical fiber to ensure a gaussian beam profile. An iris can be used to change the diameter of the beam for adjustment of the filling parameter β_G.

Microfluidic chip setup The setup used in the experiments with the microfluidic chips (cf. chapter 6) is based on a modified single molecule detection setup as described previously. The chip is placed in a custom-made fixture (see fig. A.2B) in front of the microscope objective, which is used for collection of emitted fluorescence photons. A flip mirror **FM** is placed in front of the laser, making it possible to choose between the chip-waveguides and the microscope objective for excitation of the sample. See figure A.3 for a drawing of the setup. Additionally, the objective can be replaced with an optical fiber to allow for fiber-based detection of signals from the chip. By placing the fiber end in a three-axis positioning system (T-LS 28M, Zaber Technologies Inc.), precise control of the fiber position is possible. A custom-made software for the LabView environment allows for raster-scanning the chip with the fiber.

A.1.2. Emitter-Fiber Distance Measurements

A tunable white-light source (**WLS**, SuperKPower with SpectraK AOTF, NKT photonics)) is exciting a sample of spin-coated QDot800 quantum dots placed on a piezo stage (**S**). To focus the emission from the light-source, an oil-immersion objective (**M**,

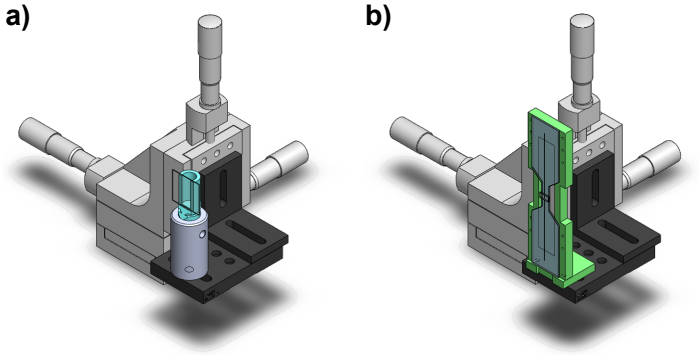

Figure A.2.: Drawing of modified parts of objective-based setup **a)** and chip setup **b)**, respectively.

NA=1.3, Leica) is used. The light emitted by the quantum dots can be collected by the objective and an optical fiber (**O**, FS-SN-3224, 3M). The fiber is fixed by a custom-made fixture on a single-axis piezo-stage (**P**, PIFOC, PI), to allow for precise controll of emiter-fiber distance. The beam path at the objective side is passing through a beam splitter and an bandpass filter (**F**, XF3307, Omega Optical) for removal of scattered excitation light and then focused onto a CCD camera (**CCD**, iXon, Andor Technology) for direct real-time imaging. For imaging of the sample with the fiber, the sample stage is raster-scanned while objective and fiber are kept at fixed position. The light incoupled into the fiber is transmitted through the fiber to the fiber coupler (**C**, New Focus), through an dichroic mirror (**D**, z720 RDC, Chroma) and focused onto the APD (**APD**, SPCM-AQR-13, Perkin Elmer) by an achromatic lens (**L**, f=300 mm, AC254-300-B, Thorlabs). Another band-pass filter (**F**, XF3307, Omega Optical) filters remaining scattered and excitation light. A diode laser (635 nm, IDT0-635-30, GMP) can be used to optionally excite the quantum dots through the fiber and for rough allignment of the fiber with the objective. For the experiments, the setup was first calibrated by alligning the fiber with the objective. A rough alignment can be done by coupling the laser into the fiber and superimpose the light emited from the fiber end with the focal spot of the objective while looking at the signal at the ccd camera. For fine-tuning the alignment, the WLS is tuned to 800 nm emission and the signal on the APD from the fiber emissionis maximised by calibrating both the alignment of objective and fiber and of fiber end at the fiber coupler and the APD. By raster-scanning the sample stage and detecting the signal at the APD, a scanned image of the sample surface can now be obtained, showing the incoupling into the fiber. With the PIFOC, the distance between fiber and emitter can be set with high accuracy.

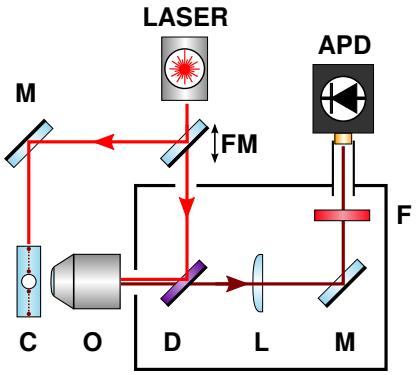

Figure A.3.: Schematic diagram of the setup in the chip experiments. Laser: red diode laser (λ=690 nm), D: Dichroic mirror, O: microscope objective (NA=0.85, Leica), C: microfluidic chip, F: bandpass filter, L: focusing lens, APD: single-photon counting avalanche photodiode module, M: mirror, FM: flip-mirror for switching excitation path between on-chip waveguides and objective. To shield the setup against ambient light, most of the beam-path is placed in a box.

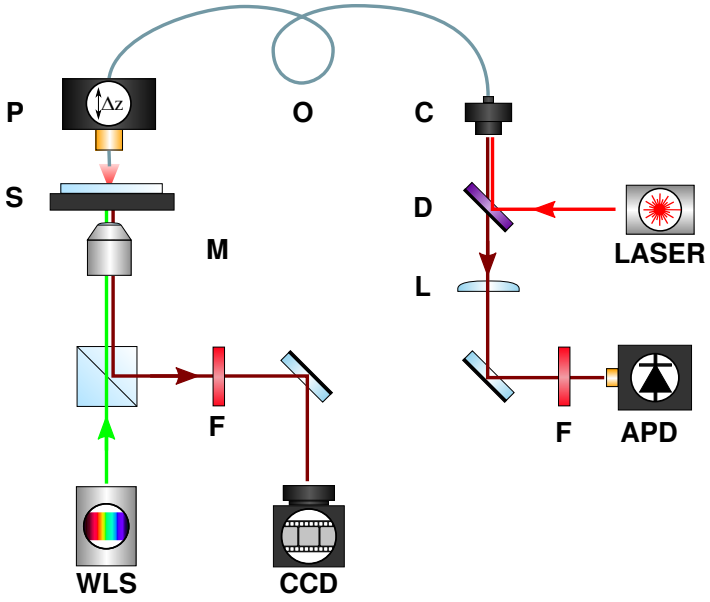

Figure A.4.: Schematic diagram of the experimental setup for distance measurements. WLS: tunable white-light source for excitation, S: Piezo stage for sample positioning, M: oil-immersion objective, CCD: CCD camera for real-time imaging, O: optical fiber, P: PIFOC stage for control of z-distance between fiber and sample, D: dichroic mirror, L: focusing lens, APD: SPAD for detection. An optional illumination path is provided by coupling a LASER into the fiber.

A.2. Fabrication of Steps

The steps used to manipulate the flow in chapter 4 have been fabricated by exposing UV glue (UVO114, EpoTek, USA) spin-coated onto microscope cover-glass (Menzel cover glass no. 1.5, thickness 0.17 mm) through a custom-made mask. The mask consists of two razor-blades fixed on a metal slab to produce a well defined thin slit of 1 mm width. Prior to the process, the cover-glass has been thoroughly cleaned by first wiping it with an acetone-soaked cloth and then submerging it for 10 minutes first in ethanol and then millipore-water in an ultrasonic bath. The modified cover-glass can be used in the standard sample containers used for the objective-based measurements in this work.

The following protocol has been found to reliably produce clearly defined steps of ≈12 µm thickness:

1. A large drop of UV-glue (≈50 µL) is placed on the cleaned cover-glass with a pipette. To evenly spread the glue on the glass, it is spin-coated at 5000 rpm for 10-20 s.

2. After spin-coating, the coated cover-glass is placed on top of the mask (coated side up) and illuminated from below by a UV lamp for 30 minutes.

3. The exposed glue is allowed to cool down for 15 minutes, after which the unexposed glue is removed by use of an ultrasonic bath with ethanol for 5 minutes. To prevent damage of the steps, the cover glass is placed upright in a special holder.

4. After a final rinsing of the cover glass with water, it can be used in experiments.

Figure A.5 again outlines the protocol. Pictures made from the steps with an optical microscope and an SEM can be found in figure A.6. The steps are generally well-defined and of good, even quality. During experiments it has been found that prolonged exposure to isopropanol during cleaning between experiments can lead to degradation and damaged steps. It is therefore advised to use clear water for cleaning of the steps and refrain from using isopropanol in high concentrations and for extended periods of time.

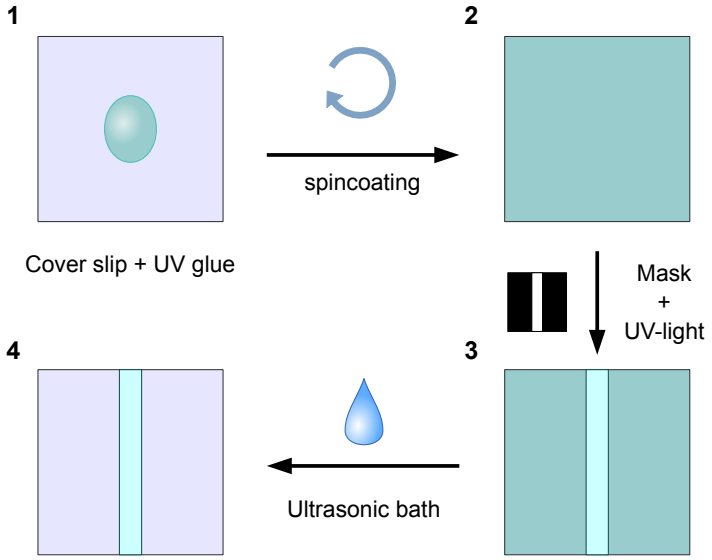

Figure A.5.: Fabrication of steps used for flow measurements. **(1)** A drop of UV glue is placed on a thoroughly cleaned cover slip and spincoated at 5000 rpm. **(2)** The evenly spread out glue is then exposed through a mask by UV light for 30 minutes. **(3)** After cooling, the remaining unexposed glue is removed in an ultrasonic bath. **(4)** The finished step can be used in experiments.

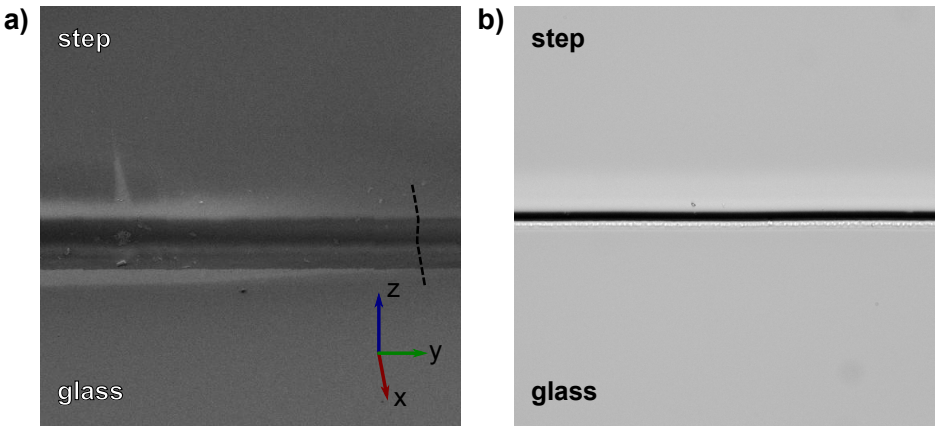

Figure A.6.: **a)** SEM picture of one of the steps, tilted view. As a guide to the eye, a coordinate system and the step profile (dashed line) have been added. The step has an even quality, although some dirt particles may be present (left). **b)** Optical microscope picture of the step, top-down view.

Appendix B.

Dyes and buffer

Fluorescent Dyes In this work, mainly three dyes have been used. Most SMD experiments have been conducted with Cy7 and Dy751, which share very similar spectral characteristics (figure B.1). In these experiments the dye was excited by a diode laser operating at 690nm. In experiments with the fiber sensor from chapter 5, a FRET-pair of Cy5.5 and Cy7, linked by 5 thymidine bases (Cy5.5-TTTTT-Cy7) was used. The thymidine bases have been chosen due to low quenching of the fluorescence emission [84, 85].

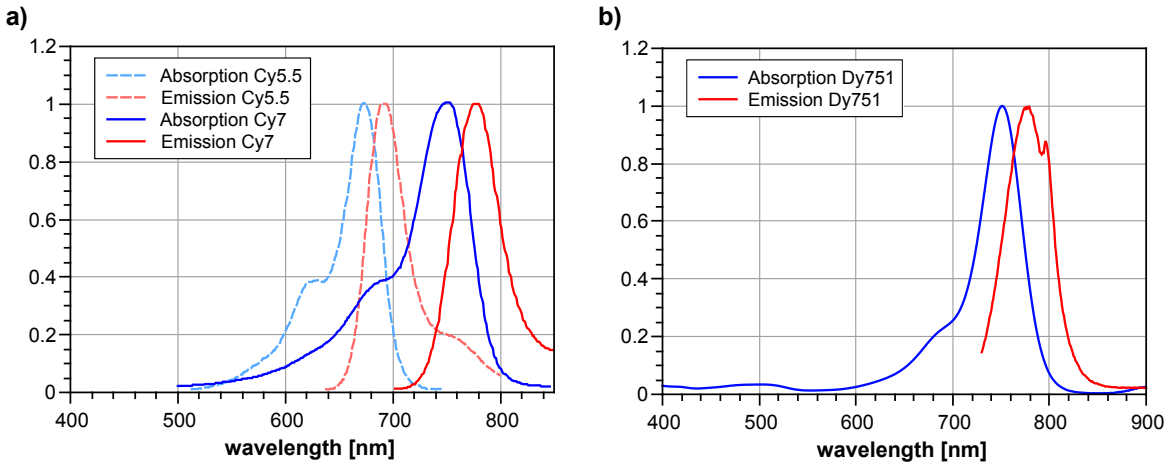

Figure B.1.: Normalized absorption and emission spectra of dyes used in this work. Blue curves depict excitation, red curves emission. **a)** Light, dashed curves: Cy5.5. Dark, solid curves: Cy7. In case of the FRET-dye, Cy5.5 is excited, energy is transmitted internally to Cy7, which is emitting (source: fluorophores.org). **b)** Dy751 (source: Dyomics GmbH).

Figure B.2 shows normalized spectra of the light leaving the fiber together with the transmission curve of the used bandpass filter (XF3307, Omega Optical), which is matched to the emission band of Cy7. The spectrum of the background was recorded with the fiber end in air, while the spectra of Cy5.5 and Cy7 were recorded when dipping the fiber in solutions containing sufficiently large concentrations of the pure dyes. Using a bandpass filter largely suppresses the background generated in the fiber while transmitting most of the acceptor fluorescence.

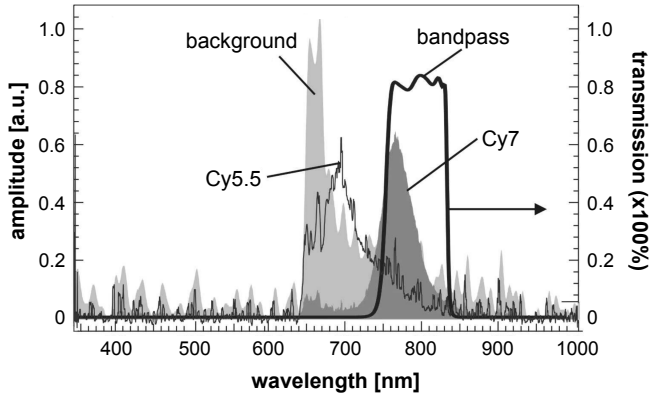

Figure B.2.: Spectra of light leaving the fiber towards the detector. As indicated: Spectrum of the background due to inelastic scattering of the excitation light in the optical fiber, the fluorescence emission of solutions of Cy5.5 and Cy7 and the transmission spectrum of the bandpass filter (XF3307, Omega Optical). The cutoff towards shorter wavelength in the spectra at $\approx$ 640 nm is due to a notch filter centered at 632 nm. Figure reproduced from [66].

Buffer solution All SMD experiments have been conducted in a stock PBS buffer solution (PBS tablets, P4417, Sigma-Aldrich) or a custom-made buffer solution (pH 8.3), prepared according to the table below. A special switching buffer was used for one set of experiments in chapter 6.

substance	amount (1M) for 500 mL buffer	concentration	part number
Tris-HCl	50 ml	100 mM	Sigma T2694
KCl	250 ml	500 mM	Fluka 60142
$MgCl_2$	7,5 ml	15mM	Fluka 63069
H_2O	192,5 ml		

Table B.1.: Recipe for a 10x, pH 8.3 buffer solution. To be diluted by 1:10 before use.

substance	amount for 1 mL buffer	concentration	part number
PBS	540 µL	10 mM	Sigma P4417
Glucose	400 µL	10% (wt/vol)	
Glucose oxydase	50 µL	100 µg/mL	
Ascorbic acid	5 µL	200 mM	Sigma A5960
Methyl viologen	5 µL	200 mM	Sigma 856177

Table B.2.: Recipe for the ROXS switching buffer as kindly provided by AG Sauer. See [83] for reference.

Appendix C.

Microfluidic Chips - Design Documents

This chapter contains the design documents of the microfluidic chips that have been used in this work. For each chip, the transmission through the on-chip waveguides and the size and shape of the waveguide mode has been measured by imaging the outcoupled mode with an objective (25x, NA 0.50, wd=1.3 mm), while the fluid channel was empty and filled with acetone, respectively. All transmission measurements and pictures have been done by the group of Dr. R. Osselame in Milan. It should be noted that the incoupling efficiency reached during the experiments conducted in Würzburg was generally lower.

	empty channel				acetone			
Nr.	**Mode**	**T[%]**	**Øx**	**Øy**	**Mode**	**T[%]**	**Øx**	**Øy**
1	too weak	-	-	-	diffuse	3.2	12	15
2	mono	1.3	8	9.8	mono	25.3	8.6	9.8
3	double	0.4	-	-	mono, long	17.5	9.2	12.8
4	mono, weak	0.19	9	10.1	mono	25.1	9.4	11.9
5	too weak	-	-	-	mono, weak	2.2	10	12

Table C.1.: Incoupling efficiency, shape and size in µm of outcoupled modes of the waveguides for the chip **"ZigZag"**

	empty channel				acetone			
Nr.	**Mode**	**T[%]**	**Øx**	**Øy**	**Mode**	**T[%]**	**Øx**	**Øy**
1	multi, weak	0.36	-	-	low multi	39.8	9.3	20.2
2	mono	1.8	8.2	11.8	mono, long	41.4	8.6	12.7
3	mono	1.6	8.7	10.1	mono	40.5	9.1	10.8

Table C.2.: Incoupling efficiency, shape and size in µm of outcoupled modes of the waveguides for the chip **"Circles"**

Nr.	empty channel				acetone			
	Mode	**T[%]**	**Øx**	**Øy**	**Mode**	**T[%]**	**Øx**	**Øy**
1	long, bad	1.2	-	-	multi, long	38.2	10.1	21.9
2	mono	1.2	9	11.5	mono	37	8.8	11
3	mono, small	3	10.6	12.4	mono	32.7	10.4	12
4	low multi	4.8	10	12.9	low multi	35.9	9.2	11.6
5	mono	4.2	11	13	mono	46.9	11.4	12.8

Table C.3.: Incoupling efficiency, shape and size in µm of outcoupled modes of the waveguides for the chip **"Carpet"**

Nr.	empty channel				acetone			
	Mode	**T[%]**	**Øx**	**Øy**	**Mode**	**T[%]**	**Øx**	**Øy**
1	weak	-	-	-	mono, bad	2.1	10	10
2	mono	0.05	6	8	mono, long	4.3	7.9	10.1
3	mono, long	1.3	8.8	11.5	low multi	23.6	8.8	11.1
4	mono, long	0.13	8.4	12.5	low multi	41.8	8.7	12
5	diffuse, long	0.04	-	-	mono, bad	21.9	14	14
6	mono, long	1	9.1	10.9	mono	48.7	9.1	12
7	mono, long	1.3	8.1	10.5	mono	61.8	8.3	11
8	diffuse, weak	0.15	-	-	mono, big	18.8	14	15
9	multi, bad	0.1	-	-	mono, big	21.9	13	14
10	mono, long	1.2	9.2	11.5	mono	41.8	9	12.2
11	no	-	-	-	no	-	-	-
12	weak, small	-	9.0	9.5	weak, small	1	8.9	9.5
13	no	-	-	-	no	-	-	-

Table C.4.: Incoupling efficiency, shape and size in µm of outcoupled modes of the waveguides for the chip **"Single"**

Nr.	empty channel				acetone			
	Mode	**T[%]**	**Øx**	**Øy**	**Mode**	**T[%]**	**Øx**	**Øy**
4	-	1.9	-	-	-	7.7	-	-
5	-	2.5	-	-	-	11.5	-	-
6	-	1.2	-	-	-	10.6	-	-
7	-	1.5	-	-	-	11.9	-	-
8	-	1.7	-	-	-	11.5	-	-
9	-	1.7	-	-	-	16.3	-	-

Table C.5.: Incoupling efficiency of the waveguides 4-9 for the chip **"SMOD.04 ch.B"**. Shape and size of the modes have not been measured.

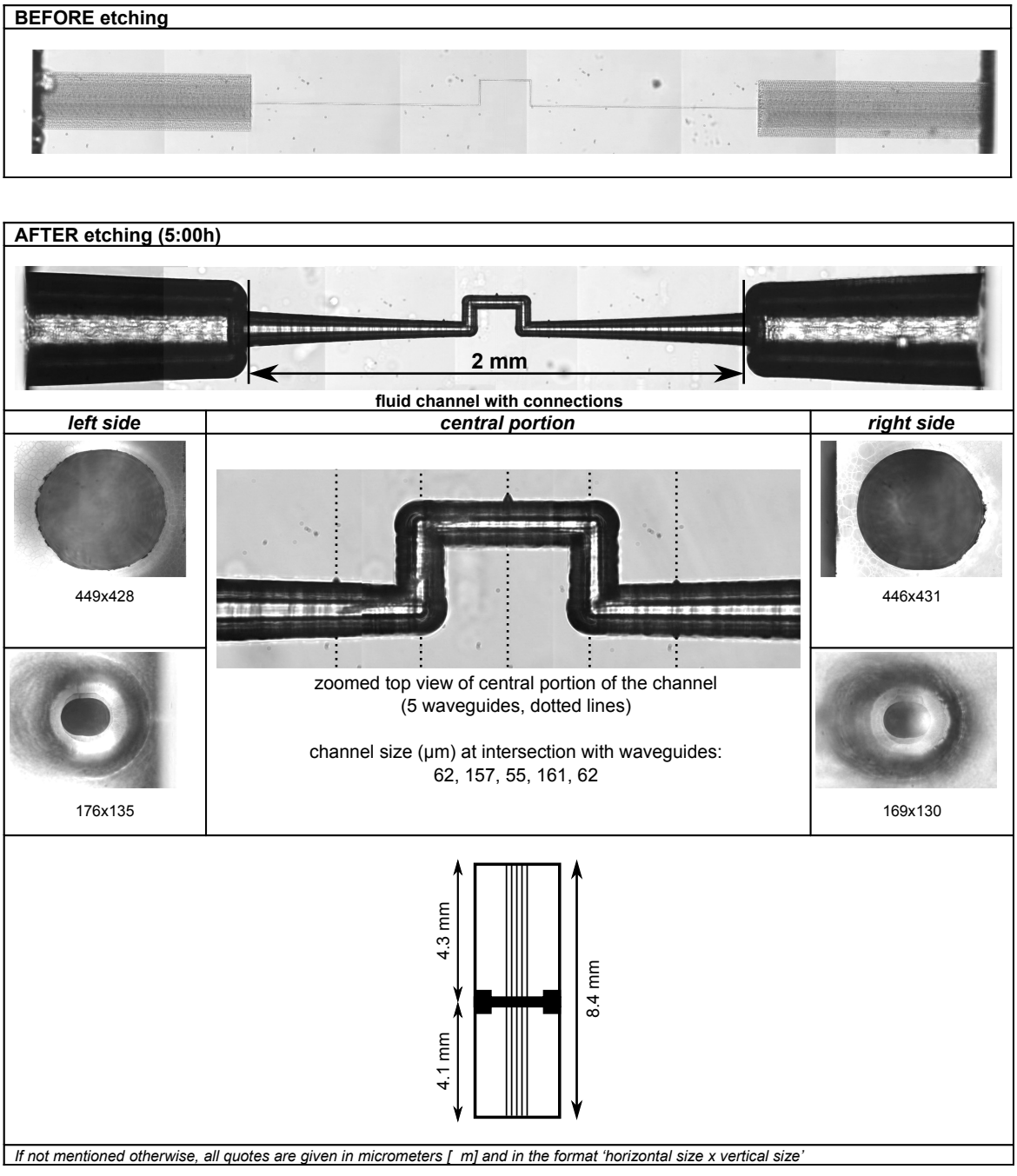

Figure C.1.: Layout of microfluidic chip "ZigZag", showing the shape of the fluid channel (2 mm length). The large cavities framing the channel are used to connect the channel with tubing. Left and right side pictures show the cross-section of the channel. Waveguides (dotted lines) are overlayed in the zoomed-in view of the central part of the channel.

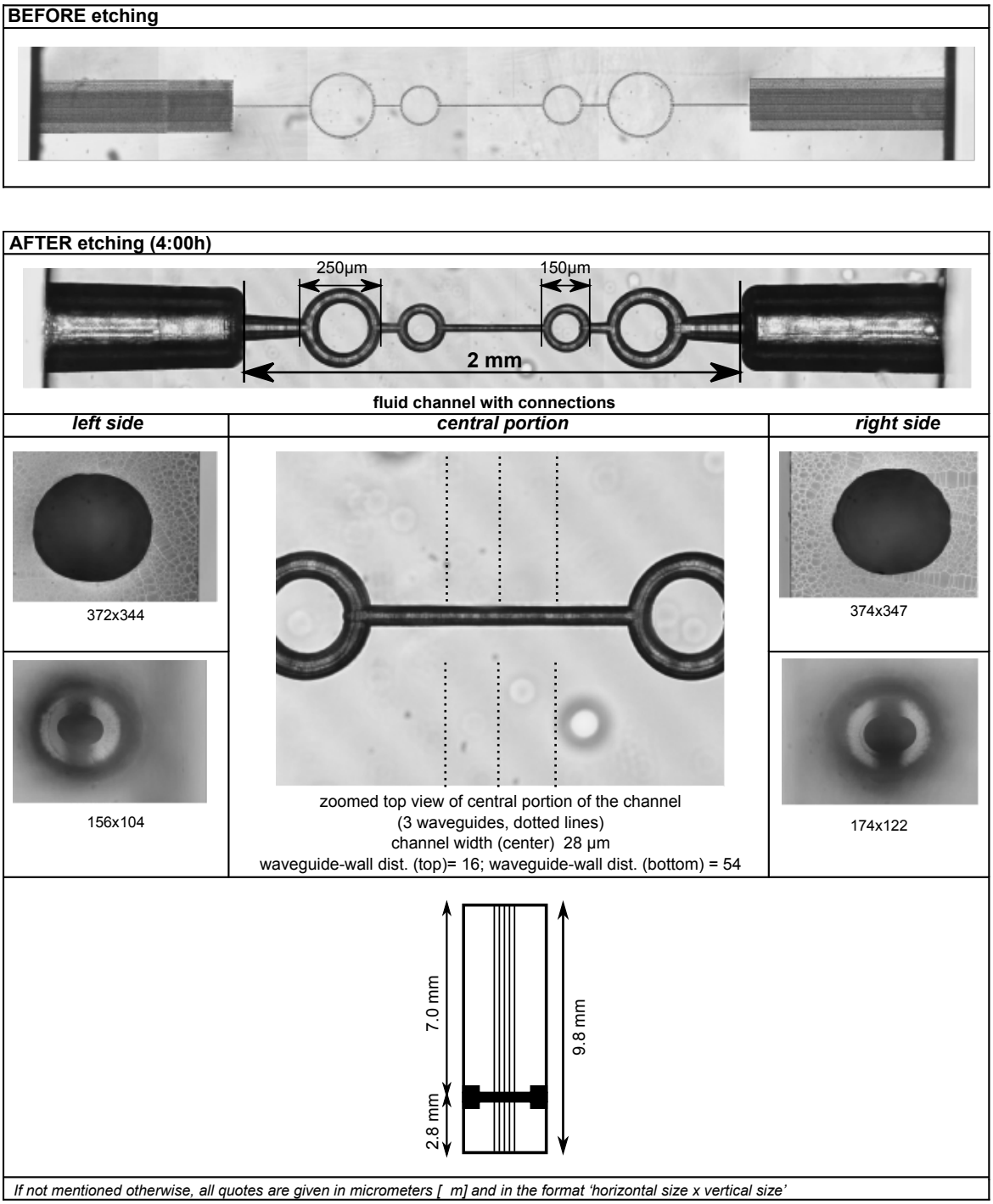

Figure C.2.: Layout of microfluidic chip "Circles", showing the shape of the fluid channel (2 mm length). The large cavities framing the channel are used to connect the channel with tubing. Left and right side pictures show the cross-section of the channel. Waveguides (dotted lines) are overlayed in the zoomed-in view of the central part of the channel.

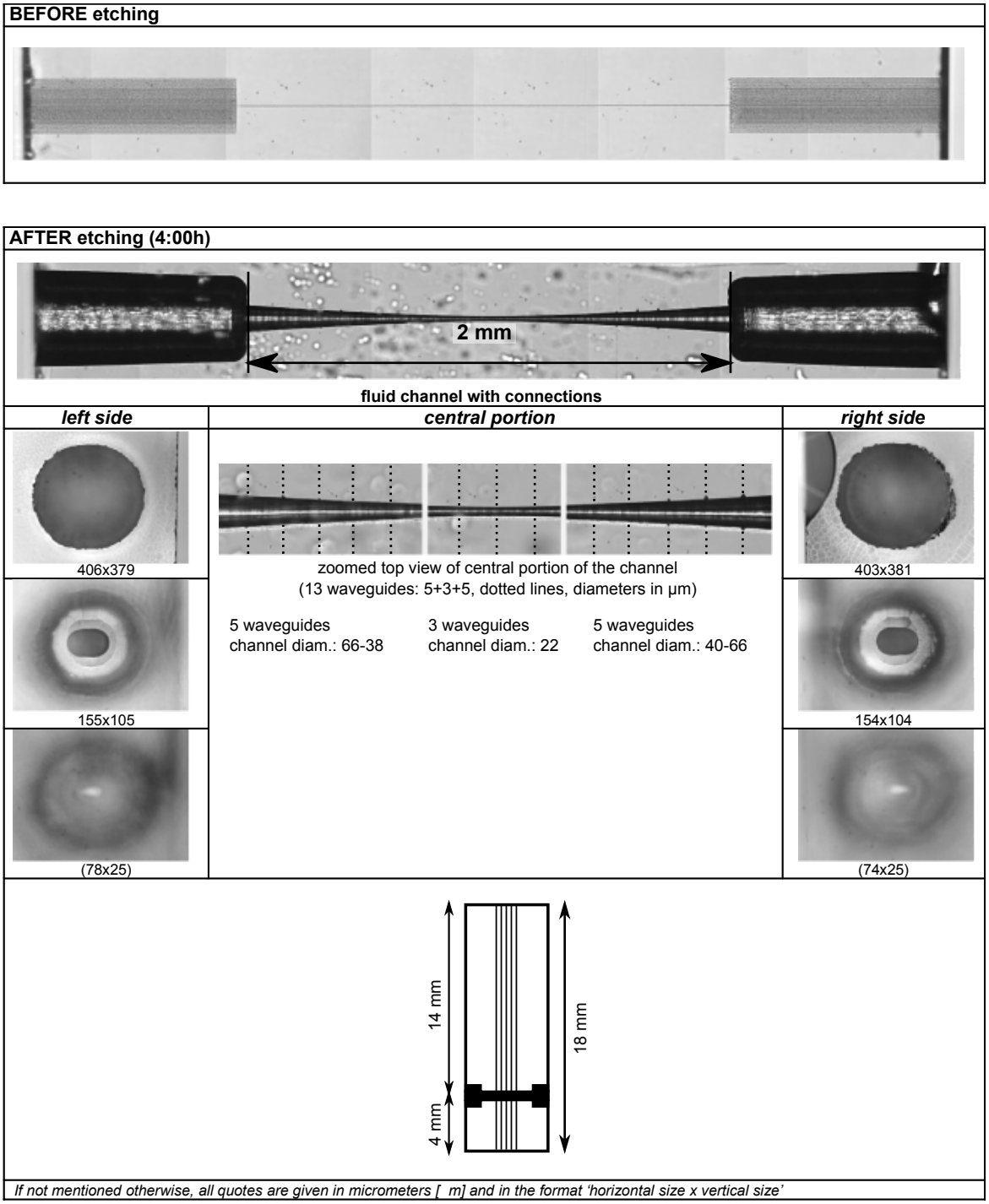

Figure C.3.: Layout of microfluidic chips "Single", showing the shape of the fluid channel (2 mm length). The large cavities framing the channel are used to connect the channel with tubing. Left and right side pictures show the cross-section of the channel. Waveguides (dotted lines) are overlayed in the zoomed-in view of the central part of the channel. The chip "Carpet" is largely identical to "Single", with the main difference being a larger fluid channel diameter (59 µm) and a lower number of waveguides (5 vs. 13).

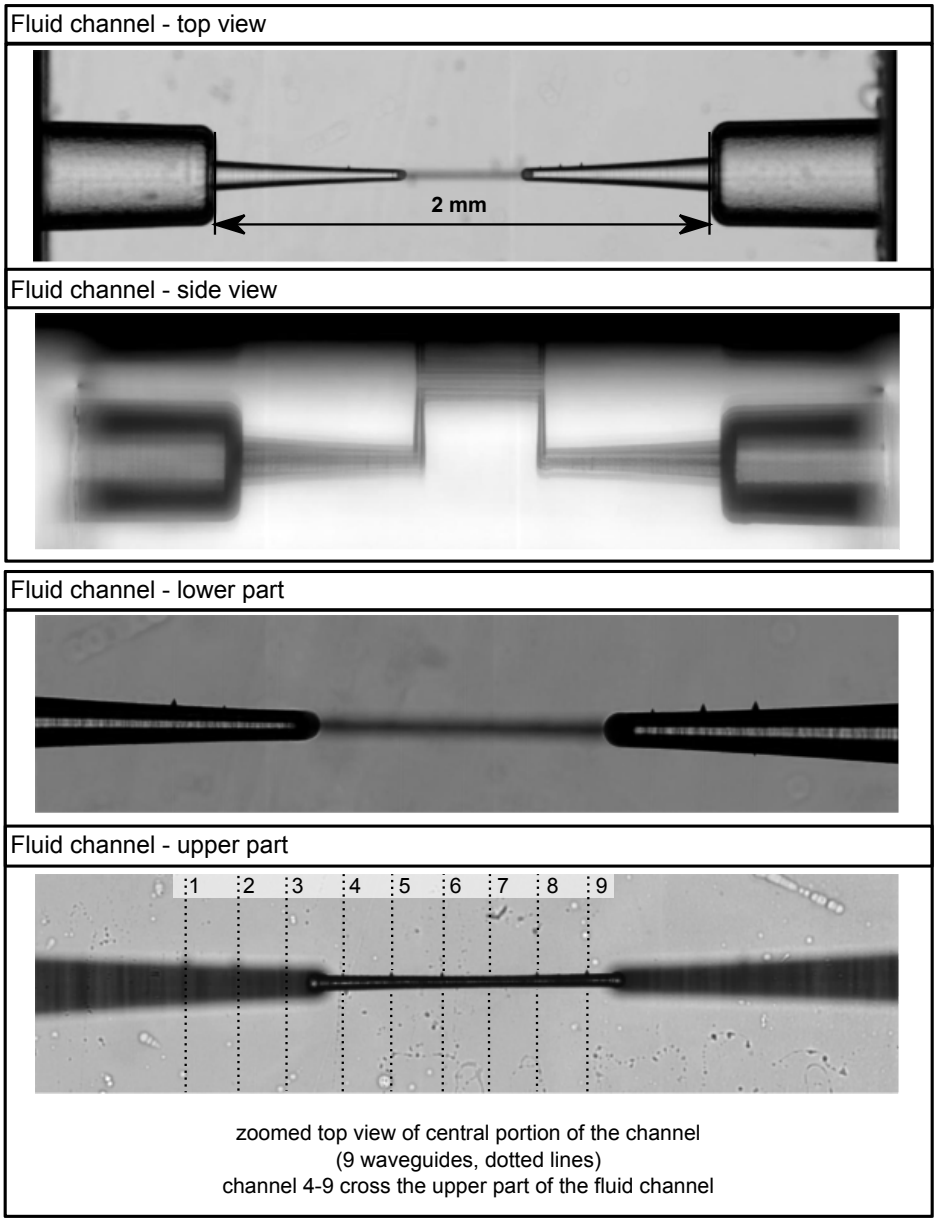

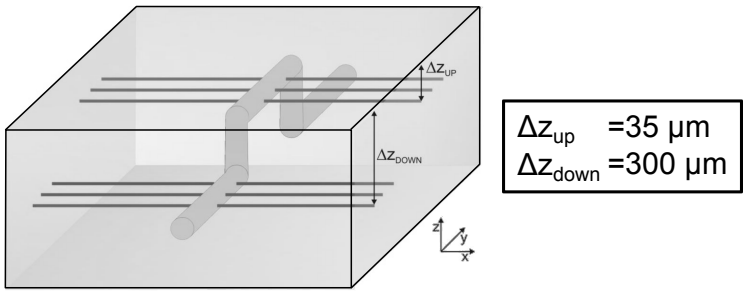

Figure C.4.: Layout of microfluidic chip "Smod.04 ch.B", showing the shape of the fluid channel (2 mm length). The large cavities framing the channel are used to connect the channel with tubing. Waveguides (dotted lines) are overlayed in the zoomed-in view of the central part of the channel. The central part of the fluid channel is reaching upwards, with a distance of 35 µm to the surface.

Appendix D.

Listings

D.1. Monte Carlo Simulations of SMD Experiments - Simulation.pas

All software that has been developed over the course of this work can be obtained from the author[1]. The following listing is taken directly from the main unit of the program used in the Monte Carlo simulations. It is written in (Object) FreePascal using Lazarus IDE in version 1.0.10. Take note that the presented code is only showing the main routines used in the simulation and is missing declaration of variables, as well as procedures related to the GUI. Several variables are assigned values by reading values from interface elements.

Listing D.1: Simulation.pas

```
function fact(x:integer):real;                                          1
{subfunction to calculate factorial}
begin
        if (x=0) then
                fact:=1                                                 5
        else
                fact:=x*fact(x-1);
end;

function poisson(y:integer; m:real):real;                               10
{subfunction providing possion distribution}
begin
        poisson:=power(m,y)*exp(-m)/fact(y);
end;
                                                                        15
function cumPois(z:integer; n:real):real;
{subfunction providing cumulative poisson}
begin
        if (z=0) then
                cumPois:=poisson(0,n)                                   20
        else
                cumPois:=poisson(z,n)+cumPois(z-1,n);
```

[1] please send an e-mail to patrickthen@web.de

```
end;

function norm(x:real;m:integer;s:integer):real;
{subfunction providing normal distribution}
begin
        norm:=1/sqrt(2*Pi*s*s)*exp(-((x-m)*(x-m))/(2*s*s));
end;

procedure TTraceSim.FormCreate(Sender: TObject);
{assign detection efficiency at position in simulated volume on
    opening of program}
begin
    timeres:=1.0E-7;

    for i:=1 to 9 do
    begin
        for j:=1 to 5 do
        begin
                weight[i,j]:=round(norm((i-5),0,2)*norm((j-3),0,1)
                    /(norm(0,0,2)*norm(0,0,1))*100);
        end;
    end;
    curPos:=0;
    curPosInt:=0;
end;


procedure TTraceSim.buStartClick(Sender: TObject);
begin
  {main part: check if buffer has to be read out, then move and
      detect}
 randomize;
 molcount:=0;
 RandMolArray;
 bgrate:=StrtoInt(edBG.text);
  BleachRate:=StrToInt(edBleach.Text);
  BinTime:=strtoint(edBinTime.text);
  conc:=strtoint(edConc.text);
  emrate:=strtoint(edEmRate.text);
  blinkrate:=strtoint(edBlinkRate.text);
  curTime:=0;
  mean:=1E-7*0.9E-6*1E-5*1000*conc*1E-12*6.022E23; //mean
      molecules in each row of array
  laMean.Caption:='Mean number of Molecules: '+floattostr(mean*9);
  step:=speed/1000*timeres/1.0E-7;  // speed is in mm/s, spatial
      res is 100nm, at max speed 1m/s step=1
```

```
tracelength:=round(totaltime/BinTime*1000000);
SetLength(Trace,tracelength);
laTrace.Caption:='Length of timetrace: '+inttostr(tracelength);
Application.ProcessMessages;
while curTime < (totaltime/timeres) do
{do movement and detection through entire array}
begin
  if buffertime = BinTime*10 then
  {internal time ref is "timeres", bintime is in microsec...((1E
     -6)/timeres)}
    begin
    bincount:=bincount+1;
    laBuffer.Caption:='Current value in buffer: '+inttostr(
       buffer);
    //Trace[bincount]:=0;
    Trace[bincount]:=buffer;
    buffertime:=0;
    buffer:=0;
    laCurPos.Caption:='Current time: '+inttostr(round(int(
       curTime*timeres)));
    Application.ProcessMessages;
    end
  else
    begin
    buffertime:=buffertime+1;
    curPos:=curPos+step;
    curPosInt:=round(int(curPos));
    if curPosInt=1 then shiftarray;
    curTime:=curTime+1;

    detection;
    if random(bgrate)=1 then buffer:=buffer+1; //random noise

    end;
end;
assignfile(tracefile, '/home/patrick/trace-bin'+inttostr(BinTime
   )+'-speed'+floattostr(Speed)+'-'+inttostr(totaltime)+'s-bg'+
   edBG.Text+'-blr'+edBleach.text+FileAppend.Text+'.txt');
rewrite(tracefile);
for k:=1 to tracelength-1 do
writeln(tracefile,(floattostr(k*BinTime*1.0E-6)+#9+inttostr(
   Trace[k])));
closefile(tracefile);
buffertime:=0;
buffer:=0;
curPosInt:=0;
```

```
  curPos:=0;
  bincount:=0;
  curTime:=0;
end;

procedure TTraceSim.RandMolArray;
{create new molecules in focus}
begin
  W:=random(100000)+1;
  arraypos:=random(5)+1;
  count:=0;
  while count<11 do
  begin
  if W<(cumpois(count,mean)*100000) then
    begin
    molcount:=molcount+count;
    molarray[1,arraypos]:=count;
    molarray2[1,arraypos]:=count;
    count:=11;
    end
  else count:=count+1;
  end;
  laMolNumber.Caption:='Number of Molecules: '+inttostr(molcount);
end;


procedure TTraceSim.Detection;
{"detection" of molecules, modified by weighting of focus,etc.}
begin
  for i:=1 to 9 do
  begin
  for j:=1 to 5 do
    begin
     if ((molarray2[i,j]>molarray[i,j]) AND (random(blinkrate)
        +1=1)) then molarray[i,j]:=molarray[i,j]+1; //re-activate
        dark molecules
      molatpos:=molarray[i,j];
      while molatpos>0 do
        begin
         if (random(emrate)+1=1) AND (weight[i,j]>=random(100)+1)
            then buffer:=buffer+1;
         if (random(BleachRate)+1=1) AND (weight[i,j]>=random(100)
            +1) then molarray[i,j]:=molarray[i,j]-1 ; //dark
            states!
         molatpos:=molatpos-1;
        end;
```

```
        end;
      end;

 end;

procedure TTraceSim.shiftarray;
{move molecules through focus}
begin
 for i:=1 to 8 do
       molarray[10-i]:=molarray[9-i];
       molarray2[10-i]:=molarray2[9-i];
 RandMolArray;
 curPos:=0;

end;
```

D.2. Matlab Routine for Fitting Noisy 2D-Gaussian Emission Spots

The following Matlab routine was adapted from a script originally developed by Jord Prangsma to fit spots from raster-scanned images of optical antenna. The adapted routine has been adjusted in order to more efficiently fit noisy, elongated and arbitrarily oriented emission spots from raster-scanned images with a 2D-gaussian. On execution it is possible to choose between automatic and manual detection of peaks. For noisy data manual detection is advised. To this end a user interface is opened that lets the user manually select the spots to be fitted with the mouse.

Listing D.2: PeakFit2k

```
clc;
close all;
clear all;
% Read data
[filename,path]=uigetfile('*.txt','Pick file for peakfind and
    analysis');
filenameandpath=[path,filename];
dat=ReadConf(filenameandpath);
Acent=dat.data1;
xAxis=dat.x;
yAxis=dat.y;
Acent=flipud(Acent);
bg=mean(mean(Acent)); %average of matrix to get a first, rough
    estimate of background
A=ones(xAxis+100)*(bg*0.9); %creates some larger matrix
```

```
A(50:xAxis+49,50:xAxis+49)=Acent; %places original data at center
    of large matrix to prevent issues at border
[iszx,iszy]=size(A);
% parameters
span=35;          %radius' of the sub-area where the gaussian is
    fitted to
sz=2*span+1;%so this is the total span of the sub-area
span2=25;
sz2=2*span2+1;
% make the X,Y and with that the Radius in the subarea
X=repmat([1:sz2]-span2-1,sz,1);
Y=repmat(([1:sz]-span-1)',1,sz2);
R=sqrt(X.^2+Y.^2);
% decrease number of minima via convolution The a should be tuned
    according
% to scale: still to be implemented
a=0.05;
fitinit=dlmread('fitinit.txt'); %fitinit contains starting values
    for width and rotation of gaussian
wx=fitinit(:,1);
wy=fitinit(:,2);
theta=fitinit(:,3);
% select peak detection method
button=questdlg('Auto peak detection, manual entry, or repeated
    fit?','Peak Detection','Auto','Manual','Repeat','Auto');
switch button
    case 'Auto'
        % convolution gauss
        Fcon=exp(-(wx*(cos(theta)*X+sin(theta)*Y)).^2-(wy*(sin(
            theta)*X+cos(theta)*Y)).^2);
        Ac=conv2(A,Fcon,'same');
        %Ac=A;
                % find local maxima
        B=imregionalmax(Ac);
        [x,y]=find(B==1); % get x and y coordinates
        nrlin=find(B(:)==1);
        szl1=max(size(x));

        val=Ac(nrlin); % the local maximum value in Ac - for noisy
            QD, value in A could be too low despite maximum,
           wouldn't work

        Dis1=max(max(Ac))/3; % try to determine first criterium by
            convoluted matrix Ac
        ind2=find(val>=Dis1); % teh index
        x2=x(ind2); % the subset x coordinates
```

```
        y2=y(ind2); % the subset y coordinates
        val2=val(ind2); % the subset values
        sz12=max(size(x2));
    case 'Manual'
        FitGui;                                                    55
        XYpos=dlmread([dat.pathstr,'peakpos.txt']);
        x2=XYpos(:,2)+50; %+50 is due to additional border region.
            Remove otherwise...
        y2=XYpos(:,1)+50;
        sz12=max(size(x2));
    case 'Repeat'                                                  60
        XYpos=dlmread([dat.pathstr,'peakpos.txt']);
        x2=XYpos(:,2)+50;
        y2=XYpos(:,1)+50;
        sz12=max(size(x2));
end;                                                               65
% gaussian fitted in sub region
for n=1:sz12 % for each local minimum
    if x2(n)>span+1 && y2(n)>span+1 && x2(n)<iszx-span-1 &&y2(n)<
       iszy-span-1 % to close to the edge the procedure does not
       work
        subA=A(x2(n)-span:x2(n)+span,y2(n)-span2:y2(n)+span2); %
            sub region data
        %subA(subA<5)=NaN;                                         70
        coef=Fit2DGaussian2(wx,wy,theta,bg,subA,X,Y); % the fit
        result(n,:)=coef; % put results in list
        % result(n,3:4)=[wx wy]; %put fixed width values in list
        % calculate the volume under the curve
        Vraw(n)=sum(sum(subA));                                    75
        % determine the amplitude of the noise: stil to be
            implemented
        Anoise=2;
        % determine the volume of the noise
        Vnoise=Anoise*sz*sz2;
        V=Vraw-Vnoise;                                             80

    else
        result(n,:)=[0 0 0 0]; % needed to skip maxima located
            near the edge
    end;
end;                                                               85
% this is purely for presentation
F=zeros(iszx,iszy);
F2=F;
for n=1:sz12
```

```
    if x2(n)>span+1 && y2(n)>span+1 && x2(n)<iszx-span-1 &&y2(n)<
        iszy-span-1
    Fsub=bg*0.9+result(n,1)*exp(-(wx*(cos(theta)*(X+result(n,2))+
        sin(theta)*(Y+result(n,3)))).^2-(wy*(sin(theta)*(X+result(n
        ,2))+cos(theta)*(Y+result(n,3)))).^2);
    Fsub2=result(n,1)*exp(-(wx*(cos(theta)*(X+result(n,2))+sin(
        theta)*(Y+result(n,3)))).^2-(wy*(sin(theta)*(X+result(n,2))
        +cos(theta)*(Y+result(n,3)))).^2);
    xm=x2(n)-span;
    xp=x2(n)+span;
    ym=y2(n)-span2;
    yp=y2(n)+span2;
    F(xm:xp,ym:yp)=Fsub;
    F2(xm:xp,ym:yp)=Fsub2;
    end;
end;
% second criterium : fitted gaussian  amplitude larger than Dis2
Dis2=1;
m=1;
for n=1:szl2
    if result(n,1)>Dis2 %&& result(n,3)>Dis3
        endresult(m,1)=x2(n);
        endresult(m,2)=y2(n);
        endresult(m,5:7)=result(n,:);
        endresult(m,3)=V(n);
        endresult(m,4)=bg*0.9;
        endresult(m,8)=A(x2(n),y2(n));
        m=m+1;
    end;
end;
% layout of endresult: 1) x-coordinate, 2) y-coordinate,
% 3) Gauss-fit-param1, 4) Gauss-fit-param1, 5) Gauss-fit-param1,
% 6) experimental volume in the subarea, dark counts subtracted
    but
% no backround subtracted
f=figure('Position',[100 100 800 500]);
subplot(2,2,2)
imagesc(A)
text(endresult(:,2),endresult(:,1),num2str((1:max(size(endresult
    (:,1))))'),'fontsize',12,'color','white')
xlabel('Raw data')
colorbar
subplot(2,2,4)
imagesc(F)
xlabel('fitted data')
colorbar
```

```
cnames = {'X-coor','Y-coor','Value','Offset','Amp','Offset x','
    Offset y','Raw Value'};
t = uitable('Data',endresult(:,1:8),'ColumnName',cnames,...
            'Parent',f,'Position',[30 40 240 420],'ColumnWidth'
                ,{70});
myformat = '%u\t %u\t %u\t %4.2f\t %4.2f\t %4.2f\t %4.3f\t %4d\n';
[pathname, name, ext] = fileparts(filenameandpath);
fid = fopen([name 'fitdata.txt'],'a');

[rows,cols]=size(cnames)

for i=1:rows %To write a header consisting of the column names in
    cnames
 fprintf(fid,'%s\t',cnames{i,1:end-1})
 fprintf(fid,'%s\n',cnames{i,end})
end;

fprintf(fid, '\n');
fprintf(fid, '\n');
fprintf(fid, myformat, endresult');
fclose(fid);
saveas(f,[filename '.jpg']);
```

Listing D.3: Fit2DGaussian2.m

```
% fitting subroutine
function coef=Fit2DGaussian2(wx,wy,theta,bg,Asub,X,Y)
  stcoef=[max(max(Asub))/2,0,0];
  coef=fminsearch(@T2DGError2,stcoef,[],wx,wy,theta,bg,Asub,X,Y);
```

Listing D.4: T2DGError2.m

```
% error function for 2D Gaussian fit
function error=T2DGError2(coef,ax,ay,theta,bg,A,x,y)
  offset=bg*0.9;
  mag=coef(1);
  x0=coef(2);
  y0=coef(3);
  F=offset+mag*exp(-(ax*(cos(theta)*(x+x0)+sin(theta)*(y+y0)))
      .^2-(ay*(sin(theta)*(x+x0)+cos(theta)*(y+y0))).^2);
  Amx=max(max(A));
  if mean(mean(A)) < (bg+0.5)
        error=sum(sum((A-F).^2));
  else
       F(A<(Amx/3)&F>((mag+offset)/4))=A(A<(Amx/3)&F>((mag+offset)
           /4));
     % This is an attempt at weighting:
```

```
    % Disregard values where measured data shows bleaching by
        setting F=A at
    % this positions.                                          15
        error=sum(sum((A-F).^2));
end;
```

Bibliography

[1] P. Haas, P. Then, A. Wild, W. Grange, S. Zorman, M. Hegner, M. Calame, U. Aebi, J. Flammer, and B. Hecht. Fast quantitative single-molecule detection at ultralow concentrations. *Analytical Chemistry*, 82(14):6299–6302, July 2010.

[2] P. Then, G. Razinskas, T. Feichtner, P. Haas, A. Wild, N. Bellini, R. Osellame, G. Cerullo, and B. Hecht. Remote detection of single emitters via optical waveguides. *Physical Review A*, 89(5), May 2014.

[3] Ch. Zander, J. Enderlein, and R. Keller. *Single molecule detection in solution: Methods and applications.* John Wiley & Sons, Berlin, 2002.

[4] N. G. Walter, C. Huang, A. J. Manzo, and M. A. Sobhy. Do-it-yourself guide: how to use the modern single-molecule toolkit. *Nature Methods*, 5(6):475–489, June 2008.

[5] D. R. Walt. Optical Methods for Single Molecule Detection and Analysis. *Analytical Chemistry*, 85(3):1258–1263, February 2013.

[6] W. E. Moerner and L. Kador. Optical detection and spectroscopy of single molecules in a solid. *Physical Review Letters*, 62(21):2535–2538, May 1989.

[7] M. Orrit and J. Bernard. Single pentacene molecules detected by fluorescence excitation in a p-terphenyl crystal. *Physical Review Letters*, 65(21):2716–2719, November 1990.

[8] E. Brooks Shera, Newton K. Seitzinger, Lloyd M. Davis, Richard A. Keller, and Steven A. Soper. Detection of single fluorescent molecules. *Chemical Physics Letters*, 174(6):553–557, November 1990.

[9] Th. Förster. Zwischenmolekulare Energiewanderung und Fluoreszenz. *Annalen der Physik*, 437:55–75, 1948.

[10] R. Roy, S. Hohng, and T. Ha. A practical guide to single-molecule FRET. *Nature Methods*, 5(6):507–516, June 2008.

[11] J. Hohlbein, K. Gryte, M. Heilemann, and A. Kapanidis. Surfing on a new wave of single-molecule fluorescence methods. *Physical Biology*, 7(3):031001, August 2010.

[12] D. W. Pohl, W. Denk, and M. Lanz. Optical stethoscopy: Image recording with resolution $\lambda/20$. *Applied Physics Letters*, 44(7):651–653, April 1984.

[13] E. Betzig, A. Lewis, A. Harootunian, M. Isaacson, and E. Kratschmer. Near Field Scanning Optical Microscopy (NSOM). *Biophysical Journal*, 49(1):269–279, January 1986.

[14] T. Klar and S. Hell. Subdiffraction resolution in far-field fluorescence microscopy. *Optics Letters*, 24(14):954, July 1999.

[15] E. Betzig, G. H. Patterson, R. Sougrat, O. W. Lindwasser, S. Olenych, J. S. Bonifacino, M. W. Davidson, J. Lippincott-Schwartz, and H. F. Hess. Imaging Intracellular Fluorescent Proteins at Nanometer Resolution. *Science*, 313(5793):1642–1645, September 2006.

[16] M. J. Rust, M. Bates, and X. Zhuang. Sub-diffraction-limit imaging by stochastic optical reconstruction microscopy (STORM). *Nature Methods*, 3(10):793–796, October 2006.

[17] F.R. Kramer and S. Tyagi. Molecular beacons: Probes that fluoresce upon hybridization. *Nature Biotechnology*, 14:303–308, 1996.

[18] J. Knight. Microfluidics: Honey, I shrunk the lab. *Nature*, 418(6897):474–475, 2002.

[19] D. Mark, S. Haeberle, G. Roth, F. von Stetten, and R. Zengerle. Microfluidic lab-on-a-chip platforms: requirements, characteristics and applications. *Chemical Society Reviews*, 39(3):1153, 2010.

[20] A. M. Foudeh, T. Fatanat Didar, T. Veres, and M. Tabrizian. Microfluidic designs and techniques using lab-on-a-chip devices for pathogen detection for point-of-care diagnostics. *Lab on a Chip*, 12(18):3249, 2012.

[21] P. Holzmeister, G. P. Acuna, D. Grohmann, and P. Tinnefeld. Breaking the concentration limit of optical single-molecule detection. *Chemical Society Reviews*, 43(4):1014, 2014.

[22] N. Hosaka and T. Saiki. Near-field fluorescence imaging of single molecules with a resolution in the range of 10 nm. *Journal of Microscopy*, 202(2):362–364, 2001.

[23] J. N. Farahani, D. W. Pohl, H.-J. Eisler, and B. Hecht. Single quantum dot coupled to a scanning optical antenna: A tunable superemitter. *Physical Review Letters*, 95(1), June 2005.

[24] C. M. Puleo and T. Wang. Microfluidic means of achieving attomolar detection limits with molecular beacon probes. *Lab on a Chip*, 9(8):1065–1072, April 2009.

[25] T. Klamp, M. Camps, B. Nieto, F. Guasch, R. T. Ranasinghe, J. Wiedemann, Z. Petrasek, P. Schwille, D. Klenerman, and M. Sauer. Highly Rapid Amplification-Free and Quantitative DNA Imaging Assay. *Scientific Reports*, 3, May 2013.

[26] L. Novotny and B. Hecht. *Principles of Nano-Optics*. Cambridge University Press, Cambridge, 2012.

[27] B. Valeur and M. N. Berberan-Santos. *Molecular fluorescence principles and applications*. WileyVCH ; John Wiley [distributor], Weinheim; Chichester, 2012.

[28] A. Iqbal, S. Arslan, B. Okumus, T. J. Wilson, G. Giraud, D. G. Norman, T. Ha, and D. M. J. Lilley. Orientation dependence in fluorescent energy transfer between Cy3 and Cy5 terminally attached to double-stranded nucleic acids. *Proceedings of the National Academy of Sciences*, 105(32):11176–11181, 2008.

[29] L Stryer. Fluorescence energy transfer as a spectroscopic ruler. *Annual Review of Biochemistry*, 47(1):819–846, 1978.

[30] F.R. Kramer, S. Tyagi, and S. Marras. Wavelength-shifting molecular beacons. *Nature Biotechnology*, 18:1191–1196, 2000.

[31] A. K. Ghatak. *An introduction to fiber optics*. Cambridge University Press, Cambridge ; New York, 1998.

[32] J. Bures. *Guided optics: optical fibers and all-fiber components*. Physics textbook. Wiley-VCH, Weinheim, 2009.

[33] H. Unger. *Planar optical waveguides and fibres*. Oxford engineering science series. Clarendon Press, Oxford [Eng.] ; New York, 1977.

[34] J. Durnin. Exact solutions for nondiffracting beams. i. the scalar theory. *J. Opt. Soc. Am. A*, 4(4):651–654, 1987.

[35] J. Durnin, J. J. Miceli Jr, and J. H. Eberly. Diffraction-free beams. *Physical Review Letters*, 58(15):1499–1501, 1987.

[36] M. Born. *Principles of optics: electromagnetic theory of propagation, interference and diffraction of light*. Cambridge University Press, Cambridge ; New York, 7th expanded ed edition, 1999.

[37] Z. Jiang, Q. Lu, and Z. Liu. Propagation of apertured bessel beams. *Applied optics*, 34(31):7183–7185, 1995.

[38] F. Bloisi and L. Vicari. Bessel beams propagation through axisymmetric optical systems. *Journal of Optics*, 22(1):3, 1991.

[39] V. Klimov, M. Ducloy, and V. S. Letokhov. Spontaneous emission of an atom in the presence of nanobodies. *Quantum Electronics*, 31(7):569, July 2001.

[40] A. W. Snyder. *Optical waveguide theory*. Number 190 in Science paperbacks. Chapman and Hall, London ; New York, 1983.

[41] K. Lee. *Principles of antenna theory*. Wiley, Chichester [West Sussex] ; New York, 1984.

[42] A. Einstein. Über die von der molekularkinetischen Theorie der Wärme geforderte Bewegung von in ruhenden Flüssigkeiten suspendierten Teilchen. *Annalen der Physik*, 322(8):549–560, 1905.

[43] L. Böswirth and S. Bschorer. *Technische Strömungslehre: Lehr- und Übungsbuch*. Springer Vieweg, Wiesbaden, 2014.

[44] H. J. Spurk and N. Aksel. *Fluid Mechanics*. Springer-Verlag, Berlin, Heidelberg, 2008.

[45] H. Oertel jr. *Prandtl - Führer durch die Strömungslehre, Grundlagen und Phänomene*. Springer Vieweg, Wiesbaden, 2012.

[46] E. L. Elson and D. Magde. Fluorescence correlation spectroscopy. i. conceptual basis and theory. *Biopolymers*, 13(1):1–27, 1974.

[47] R. Rigler, Ülo Mets, J. Widengren, and P. Kask. Fluorescence correlation spectroscopy with high count rate and low background: analysis of translational diffusion. *European Biophysics Journal*, 22(3):169–175, 1993.

[48] J. Ries and P. Schwille. Fluorescence correlation spectroscopy. *BioEssays*, 34(5):361–368, 2012.

[49] O. Krichevsky and G. Bonnet. Fluorescence correlation spectroscopy: the technique and its applications. *Reports on Progress in Physics*, 65(2):251, 2002.

[50] J. Enderlein, I. Gregor, D. Patra, T. Dertinger, and U. B. Kaupp. Performance of fluorescence correlation spectroscopy for measuring diffusion and concentration. *ChemPhysChem*, 6(11):2324–2336, November 2005.

[51] D. Magde, W. W. Webb, and E. L. Elson. Fluorescence correlation spectroscopy. III. uniform translation and laminar flow. *Biopolymers*, 17(2):361–376, 1978.

[52] M. Goesch, H. Blom, J. Holm, T. Heino, and R. Rigler. Hydrodynamic flow profiling in microchannel structures by single molecule fluorescence correlation spectroscopy. *Analytical Chemistry*, 72(14):3260–3265, July 2000.

[53] P. C. Brister, K. K. Kuricheti, V. Buschmann, and K. D. Weston. Fluorescence correlation spectroscopy for flow rate imaging and monitoring - optimization, limitations and artifacts. *Lab on a Chip*, 5(7):785, 2005.

[54] T. Plakhotnik, W.E. Moerner, V. Palm, and Urs P. Wild. Single molecule spectroscopy: maximum emission rate and saturation intensity. *Optics Communications*, 114(1-2):83–88, January 1995.

[55] W. Grange, P. Haas, A. Wild, M. Calame, M. Hegner, and B. Hecht. Detection of transient events in the presence of background noise. *J. Phys. Chem. B*, 112:7140–7144, 2008.

[56] M. H. Horrocks, H. Li, J. Shim, R. T. Ranasinghe, R. W. Clarke, W. Huck, C. Abell, and D. Klenerman. Single Molecule Fluorescence under Conditions of Fast Flow. *Analytical Chemistry*, 84(1):179–185, January 2012.

[57] S. T. Hess and W. W. Webb. Focal volume optics and experimental artifacts in confocal fluorescence correlation spectroscopy. *Biophysical Journal*, 83(4):2300–2317, 2002.

[58] M. J. Nasse and J. C. Woehl. Realistic modeling of the illumination point spread function in confocal scanning optical microscopy. *Journal of the Optical Society of America A*, 27(2):295–302, February 2010.

[59] D. Yin, E. Lunt, M. Rudenko, D. Deamer, A. Hawkins, and H. Schmidt. Planar optofluidic chip for single particle detection, manipulation, and analysis. *Lab on a Chip*, 7(9):1171, 2007.

[60] R. M. Vazquez, R. Osellame, D. Nolli, C. Dongre, H. van den Vlekkert, R. Ramponi, M. Pollnau, and G. Cerullo. Integration of femtosecond laser written optical waveguides in a lab-on-chip. *Lab Chip*, 9(1):91–96, 2008.

[61] P. Ghenuche, H. Rigneault, and J. Wenger. Hollow-core photonic crystal fiber probe for remote fluorescence sensing with single molecule sensitivity. *Optics express*, 20(27):28379–28387, 2012.

[62] Z. Zhu and T. Brown. Full-vectorial finite-difference analysis of microstructured optical fibers. *Optics Express*, 10(17):853–864, 2002.

[63] S. Kasarova, N. Sultanova, C. Ivanov, and I. Nikolov. Analysis of the dispersion of optical plastic materials. *Optical Materials*, 29(11):1481–1490, July 2007.

[64] E. Palik. *Handbook of Optical Constants of Solids, Volumes I, II, and III: Subject Index and Contributor Index*. Elsevier Science & Tech, 1985.

[65] B. Hecht, P. Haas, A. Wild, M. Hegner, and M. Calame. Single analyte molecule detection by fibre fluorescence probe. United States Patent, 2010. US 7,657,133 B2.

[66] P. Haas. *Remote optical sensing and quantification of single analyte molecules in liquids through a waveguide*. PhD thesis, Philosophisch-Naturwissenschaftliche Fakultät Universitaet Basel, 2006.

[67] P. Then. Aufbau und Charakterisierung eines faseroptischen Einzelmolekülsensors. Diplomarbeit, Fakultät für Physik und Astronomie, Julius-Maximilians-Universität Würzburg, March 2008.

[68] B. R. Munson, D. F. Young, and T. H. Okiishi. *Fundamentals of Fluid Mechanics*. John Wiley & Sons, Inc, 2006.

[69] S. A. Soper, Q. L. Mattingly, and P. Vegunta. Photon burst detection of single near infrared fluorescent molecules. *Analytical Chemistry*, 65:740–747, 1993.

[70] J. Schaffer, A. Volkmer, C. Eggeling, V. Subramaniam, G. Striker, and C.A.M. Seidel. Identification of Single Molecules in Aqueous Solution by Time-Resolved Fluorescence Anisotropy. *The Journal of Physical Chemistry A*, 103:331–336, 1999.

[71] C. Zander, M. Sauer, K. Drexhage, D. Ko, A. Schulz, J. Wolfrum, L. Brand, C. Eggeling, and C. Seidel. Detection and characterization of single molecules in aqueous solution. *Applied Physics B*, 63:517–523, 1996.

[72] M. Sauer, K.H. Drexhage, C. Zander, and J. Wolfrum. Diode laser based detection of single molecules in solutions. *Chemical Physics Letters*, 254:223–228, 1996.

[73] S. Nie, D. T. Chiu, and R. N. Zare. Real-Time Detection of Single Molecules in Solution by Confocal Fluorescence Microscopy. *Analytical Chemistry*, 67(17):2849–2857, 1995.

[74] R. Osellame, H. Hoekstra, G. Cerullo, and M. Pollnau. Femtosecond laser microstructuring: an enabling tool for optofluidic lab-on-chips. *Laser and Photonics Reviews*, 5(3):442–463, 2011.

[75] D. R. Reyes, D. Iossifidis, P. Auroux, and A. Manz. Micro Total Analysis Systems. 1. Introduction, Theory, and Technology. *Analytical Chemistry*, 74:2623–2636, 2002.

[76] D. R. Reyes, D. Iossifidis, P. Auroux, and A. Manz. Micro Total Analysis Systems. 2. Analytical Standard Operations and Applications. *Analytical Chemistry*, 74:2637–2652, 2002.

[77] G. M. Whitesides. The origins and the future of microfluidics. *Nature*, 442:368–373, 27 July 2006.

[78] K. F Lei. Microfluidic systems for diagnostic applications a review. *Journal of laboratory automation*, 17(5):330–347, 2012.

[79] J. Wu, G. Zheng, and L. M. Lee. Optical imaging techniques in microfluidics and their applications. *Lab on a Chip*, 12(19):3566, 2012.

[80] K. C. Vishnubhatla, N. Bellini, R. Ramponi, G. Cerullo, and R. Osellame. Shape control of microchannels fabricated in fused silica by femtosecond laser irradiation and chemical etching. *Optics Express*, 17(10):8686–8695, 2009.

[81] A. Streltsov and N. Borelli. Study of femtosecond-laser-written waveguides in glasses. *Journal of the Optical Society of America*, 19(10):2496–2504, October 2002.

[82] Y. Lill and B. Hecht. Single dye molecules in an oxygen-depleted environment as photostable organic triggered single-photon sources. *Applied Physics Letters*, 84(10):1665, 2004.

[83] J. Vogelsang, R. Kasper, C. Steinhauer, B. Person, M. Heilemann, M. Sauer, and P. Tinnefeld. A reducing and oxidizing system minimizes photobleaching and blinking of fluorescent dyes. *Angewandte Chemie International Edition*, 47(29):5465–5469, July 2008.

[84] C. Seidel, A. Schulz, and M. Sauer. Nucleobase-specific quenching of fluorescent dyes. 1. nucleobase one-electron redox potentials and their correlation with static and dynamic quenching efficiencies. *The Journal of Physical Chemistry*, 100:5541–5553, 1996.

[85] S. Tyagi, S. Marras, and F.R. Kramer. Efficiencies of fluorescence resonance energy transfer and contact-mediated quenching in oligonucleotide probes. *Nucleic Acids Research*, 30(21):e122, 2002.